博士論文

Study on Interface and Crystallization of Materials in Organic Solar Cells

（有機薄膜太陽電池における材料の界面と結晶性に関する研究）

鐘　宇飛

Study on Interface and Crystallization of Materials in Organic Solar Cells

（有機薄膜太陽電池における材料の界面と結晶性に関する研究）

鐘　宇飛 (Zhong Yufei)
Hashimoto laboratory

Department of Applied Chemistry
School of Engineering, The University of Tokyo

Contents

Chapter 1. General Introduction

1.1 Background of this study

In 21^{th} century, the use of highly developed technology and scientific innovation make our life the highest level ever in human being's history. Nevertheless, a critical problem I are facing now is the energy crisis. Petroleum, the most common energy source and also the most imperative source, is especially limited in storage on earth and nonrenewable. Scientists therefore started to seek for other renewable and clean energy sources like solar energy, wind energy, geothermal energy and so forth. Among these options, solar energy looks quite promising due to its easy access and cleanness. From the last century, commercial available solar cells are fabricated based on silicon materials, which is the most important semiconductor material in electronic industry. Remarkable power conversion efficiency (PCE) has been achieved by silicon solar cells and wide spread of its application offered substantial electricity supply for our everyday life. However, silicon solar cell relied on high cost to achieve high PCE and its heavy weight make it hard to combine these cells with other system like buildings or even mobile cars. On the other hand, a new type of solar cells based on organic materials has been attracting much attention due to its potential to achieve lightweight, flexible and low-cost products. The very first example was reported in 1980s by Tang, combing p-type and n-type materials, free charges can be generated and collected to form photo-current.[1] Including organic solar cells (OSCs), organic light emitting diodes (OLEDs) or other organic electronics like organic thin film transistors (OFETs) are also studied and proved their potential for real applications.

In organic devices, especially OSCs, interface of materials is of vital importance. A critical process for electricity generation in OSCs is the free charges formation. However, unlike silicon solar cell in which the free charges could be thermally activated after the irradiation due to its high dielectric constant (ε ~ 12), organic semiconductors often have low dielectric constants (ε ~ 3), giving rise to large binding energy of electron hole pairs generated by light. Instead of being separated, these strongly bound pairs (excitons) diffuse to the p-type (donor (D)) and n-type (acceptor (A)) interface and separated by the energy offset of the highest occupied molecular orbital (HOMO) and offset of the lowest unoccupied molecular orbital (LUMO)) of these two materials (Figure 1.1.1). This process is critical to achieve current generation in OSCs and therefore makes D/A interface indispensable in the device. On the other hand, the major energy loss of OSCs also takes place at D/A interface through charge recombination. From these points above, investigating how D/A interfacial property affect OSCs performance could give important guideline to improve the PCE of devices.

One more important factor which could also significantly affect the OSC performance is the crystallization of materials. The crystallization of the materials usually affect the charge separation at interface and charge transport in the bulk. These processes have large influence on the device performance like photo-current and fill factor. Investigating how to utilize crystallization of material to control the key process like charge separation in device could be another strategy to improve efficiency of device.

In this thesis, the interface and the crystallization of the materials in organic solar cells were studied. Aiming at improving the efficiency, the photo-physical process at D/A interface was studied and controlled.

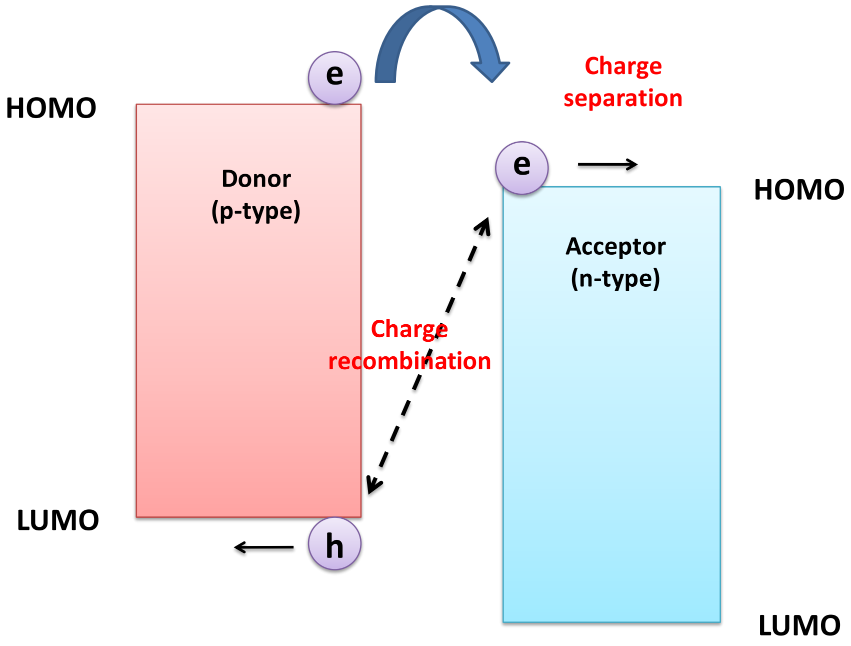

Figure 1.1.1 Schematic image of charge separation and recombination happening at D/A interface.

The thesis begins with Chapter 1 giving a detailed introduction of OSCs for its working principle, the importance of D/A interface is highlighted. In Chapter 2, the manipulation of D/A interfacial energy level and its effect on device performance was investigated. Chapter 3 focus on how D/A distance and interfacial charge separation center affect charge separation and recombination by using a spacer layer between D and A, and doping effect of spacer layer with dye molecules. An equivalent circuit model was also utilized to investigate the device performance. In Chapter 4, the effect of thermal annealing on PCBM was analyzed in terms of its electronic property and OSCs performance. In Chapter 5, a summary and perspectives of this study will be made.

1.2 Introduction of organic solar cells

1.2.1 The working principles of organic solar cells

Organic solar cells relies on several steps to generate photocurrent, namely exciton formation, exciton diffusion, charge transfer, charge separation (recombination), charge transportation and charge collection. These processes are critical for achieving high PCE of the devices. The detailed photo-physical mechanism are discussed in below:

Exciton formation

In conjugated polymers a bonding orbital (π) and an antibonding orbital (π^*) are constituted by the delocalized p_z orbital. π-orbital is occupied by the electrons and forms HOMO, and π^*-orbital is unoccupied and forms LUMO. The energy difference between HOMO and LUMO usually lies within the range of visible light. When these materials absorbed light, an electron at HOMO is excited into LUMO band, whereas a hole is generated in the HOMO band. This electron-hole pair is called exciton which could be regarded as a strongly bounded radical pair by Coulomb interaction.

Generally, the organic semiconductor materials have very low dielectric constant (ε

~ 3), giving rise to very large binding energy of the exciton (0.1 to 1.0 eV) according to the expression of binding energy *V*:

$$V = \frac{e^2}{4\pi \varepsilon_0 \varepsilon_r r}$$

where e is the charge of an electron, ε_{r} is the dielectric constant of the surrounding medium, ε_0 is the permittivity of vacuum, and r is the electron-hole separation distance. Table 1.2.1 listed the binding energy of several commonly used OSC materials.[2] On the other hand, inorganic materials have a very high dielectric constant (~12 for silicon), leading to a binding energy below 0.1 eV, in which exciton could be separated even by thermal energy. The difference of binding energy compare to those inorganic semiconductor makes organic semiconductor unable to generate free charges directly and other charge separation mechanism would be needed (will be discussed below).

Table 1.2.1 Exciton binding energy for several organic semiconductors (reproduced from ref. 2).

Organic semiconductors	Binding energy (eV)
CuPc	0.6
Alq3	1.4
PTCDA	0.8
PPPV	0.4
C_{60}	1.4
C_{70}	1.0

Exciton diffusion

After excitation, a generated exciton would take a random walk, namely exciton diffusion. Since the exciton relies on D/A interface for separation, an important parameter here is the exciton diffusion length, the distance an exciton can migrate before relaxing back to the ground state. Exciton diffusion length is given by:

$$L_{\mathrm{D}} = \sqrt{D\tau_0}$$

where D is the diffusion coefficient and τ_0 is the average life time of excition. Obviously, L_{D} would give a limitation for collecting excitons at D/A interface, a certain size of donor and acceptor domains would be desirable to get high carrier generation (will be discussed later). Usually, photoluminescence quenching experiment of D/A bilayer device as a function of layer thickness is used to estimate the L_{D} of materials. For typical polymers like PPV or P3HT, the L_{D} was proved to be less than 10 nm.[3, 4]

The exciton diffusion is usually explained by energy transfer. Possible mechanism like Förster resonance energy transfer (FRET) and Dexter energy transfer are purposed. In the former case, long range dipole-dipole coupling is utilized to transfer the excitation of donor to acceptor.[5] This type of energy transfer require the overlap of emission of the donor and absorption of the acceptor. In the latter case, a wavefunction overlap between the donor and the acceptor is necessary.

Charge transfer, separation and recombination

Within its life time, the exciton would diffusion to the D/A interface where it can be dissociated by an interfacial electron transfer reaction. Right after the electron transfer from the donor to the acceptor, the electron and hole are still bound by their Coulomb attraction, resulting in a charge transfer state (CT state). This CT state need to conquer its Coulomb interaction to give free and fully separated electron and holes. However, if these bound pair cannot be fully dissociated within the life time of CT state, geminate recombination would happen, making these charges fall to the ground state. This process is known as one of the major losses in OSCs.

Geminate recombination (often referred to recombination of electron and hole from same exciton, or called mono-molecular recombination) was first described by Onsager in 1938.[6] He calculated the probability of a electron-hole pair which is bound by their Coulomb interaction in a electrolyte will be through Brownian random walk and eventually escape from this Coulomb interaction and form free carriers. Furthermore, if the system undergoes photon excitation, a hot electron and localized hole would be generated. Due to the excess thermal energy of the electron, the electron would eventually stabilize with a certain distance (a) from the localized hole. These process are summarized and depicted by Durrant et al. (see Figure 1.2.1).[7] The distance at which the energy of Coulomb interaction equals to the thermal energy is defined as Onsager radius (r_C) :

$$r_\mathrm{C} = \frac{e^2}{4\pi\varepsilon_0\varepsilon_\mathrm{r}kT}$$

where ε_r is the dielectric constant of the surrounding medium, ε_0 is the permittivity of vacuum, e is the charge of an electron, k is Boltzmann's constant, and T is temperature in Kelvin. From the above equation, if the initial electron hole separation distance a is larger than r_C, the radical pair would escape from the Coulomb interaction and free charges would be generated. Otherwise, fully separation of electron and hole would take place with a probability of $P(E)$ (E is the electric field), while probability for geminate recombination refers as $1-P(E)$. As suggested by the expression of r_C, dielectric constant has a large impact on whether free charges could be generated or not. Generally, organic semiconductors have a very low dielectric constant (~3) compared to their inorganic counterpart (~10), the dissociation rate of excitons undergo CT state would be relatively low in organic semiconductors.

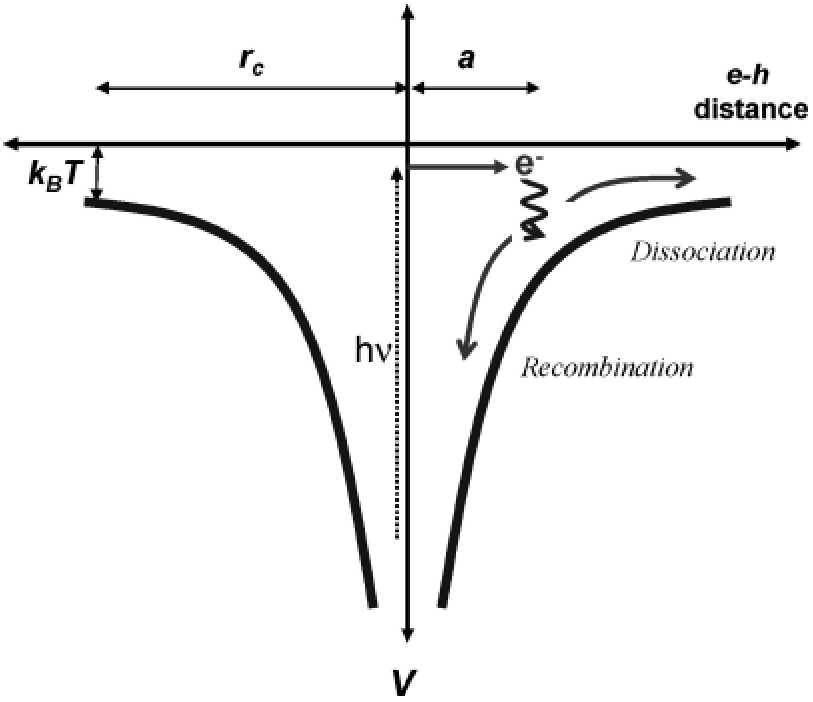

Figure 1.2.1 Potential energy diagram summarizing Onsager theory for autoionization. The red curve illustrates the potential energy resulting from Coulomb attraction as a function of electron-hole (*e*-*h*) separation. Photoexcitation results in generation of a hot, mobile electron. This electron subsequently thermalizes at a particular distance from the hole (the thermalization length, *a*). If *a* is less than the Coulomb capture radius, *r*c (as is typical for single component organic systems), then the electron-hole pair (which I refer to herein as a charge-transfer state) can either undergo geminate recombination or dissociate into free charges. Figure is reproduced from ref. 7 with permission. Copyright 2010 American Chemical Society.

As for $P(E)$, it mainly depends on initial separation distance, applied electric field and temperature which is given by below:

$$P(E) = exp\left(\frac{-r_C}{a}\right)(1 + \frac{er_C}{2kT}E)$$

where E is the electric field, e the electron charge, r_{C} is the Onsager radius, k is

Boltzmann's constant and *T* is temperature in Kelvin. As suggested by the above equation, the presence of electric field could help to dissociate charges. So far, Onsager theory has been successfully applied for several systems.[8-12]

In 1984, Onsager theory was improved by Braun.[13] In Onsager theory, if the charges does not dissociate, they will fall to the ground state directly. However, Braun pointed out that free carriers could be generated through CT state, and furthermore, those separated charges could be again back to the bounded CT state. Other modification of Onsager theory has also been made. Tachiya et al. reported that in systems with very high electron mobility, Onsager theory was not applicable.[8] The further incorporating the effect of electron mobility could explain other experiment results beyond Onsager theory.

Besides the process in Onsager theory for charge dissociation, other factors like lattice relaxation, energy disorder in organic semiconductors and polarization energy also need to be considered since the r_C in Onsager theory would be calculated to be 16 nm assuming T = 297 K. However, by including the above factors, Onsager radius was estimated to be around 4 nm. Finally, the electric field in the real OSC device would also be presented and effect charge dissociation such as electric field generated by the charges or surface dipoles. By combining these factors with Onsager theory, the photo-physical process could be screened and lead to the further understanding of how OSCs work.

Charge transportation and collection

After separation of exciton at D/A interface, free electrons and holes are generated. These free carriers would diffuse to the corresponding electrode. Driving force for such diffusion are usually explained as the carrier concentration difference at D/A interface and places away from D/A interface, and another driving force would the build-in potential from the electrodes sweeping out these free charges. During transportation, trap states originated from impurities or structure defects might capture free charges. In terms of energy level, these trap states lies within material band gap, therefore unfavorable for charge transportation. However, as depicted in Figure 1.2.2, there are two types of traps, namely shallow and deep traps. The free charges captured by the shallow trap could still be activated even by the thermal energy and join transportation again to form photo-current (black arrow). However, if the free carriers are captured by the deep trap (red arrow), which lies near the middle of band gap, they cannot be de-trap and eventually recombine and fall to ground state. This is one of the loss mechanisms in OSCs.

Several factors could limit charge transportation such as morphology of active layer and mobility of carriers. Usually the morphology of the active layer affect the charge transportation in terms of charge collection pathways. As indicated by Figure 1.2.3, the polymer donor forms hole transport pathways and fullerene acceptor forms electron transport pathways, such bicontinuous pathway lead free electron and hole to the corresponding electrodes as shown by the black arrow. On the other hand, if the morphology is not optimized, there would be dead end for these carriers to travel, as indicated by the blue arrow. If these free carriers cannot go to the electrode, they will recombine with an opposite charge which is one of the loss mechanism in OSCs. These cases suggest certain phase separation of donor and acceptor is necessary to give a clear path way for charge transport.

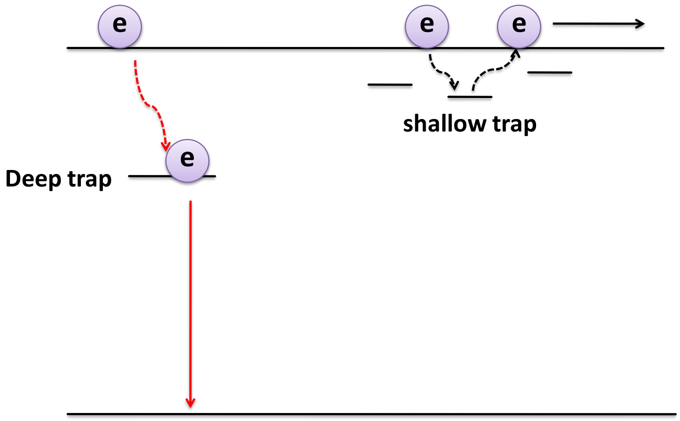

Figure 1.2.2 Schematic image of deep trap and shallow trap. Red arrow indicated carriers captured by deep trap and eventually recombined. Black arrow indicated carriers de-trap from shallow trap.

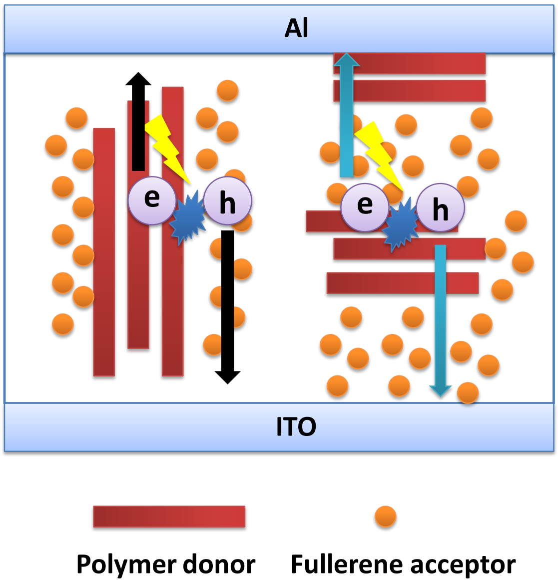

Figure 1.2.3 Schematic image of bi-continuous path ways for transporting electrons and holes to the electrode (black arrow), and un-optimized morphology hamper charge transportation (blue arrow).

When the free carriers are collected by the electrode, photo-current could be observed. However, it is proposed that efficient carrier collection at electrodes requires ohmic contact between the active layer and metal electrode. In the ideal case for ohmic contact, the acceptor LUMO level matches the Fermi level of electrode with small work function, and the donor HOMO matches the Fermi level of the electrode with large work function.[14] Nevertheless, the material used so far cannot meet such requirement. The energy level mismatch at the organic/inorganic interface might give energy barrier for charge collection and lead to loss of current in OSCs (red arrow in Figure 1.2.4). In order to minimize the current loss at organic/inorganic interface, various buffer layer between the active layer and electrode are used to achieve ohmic contact.[15] These buffer layers such as metal oxides can reduce the injection barrier and contact resistance which would minimize the current loss at the electrode interfaces. Furthermore, the buffer layer can also reduce charge recombination at this interface due to their higher lying energy level for the opposite charge to transport to the electrode (Figure 1.2.5).

Furthermore, due to the low mobility in organic semiconductors, the thickness of active layer is usually kept at 100 nm. Note that this is a compromise between charge collection and light absorption. If the thickness of active layer is to large, time for charge transport would increase, number of trap caused by defects or morphology would dominant, and space charge effect might also play a role.[16]

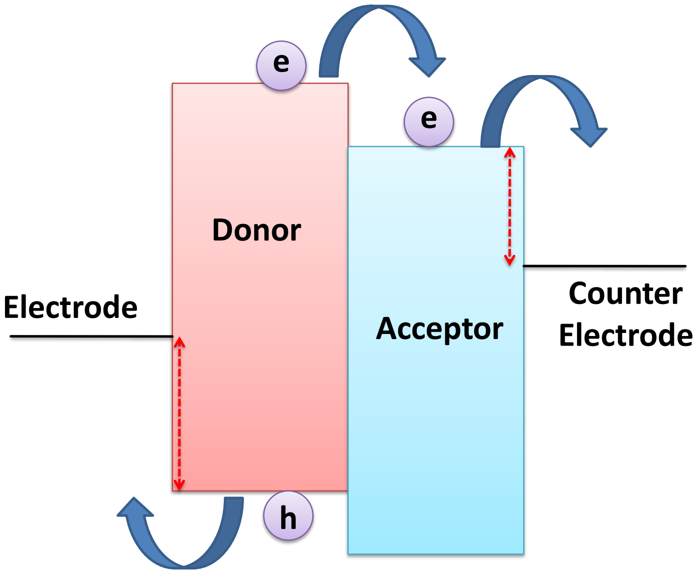

Figure 1.2.4 Schematic image of charge collection at the electrode, the current loss from the mismatch of the energy levels are indicated by the red arrow.

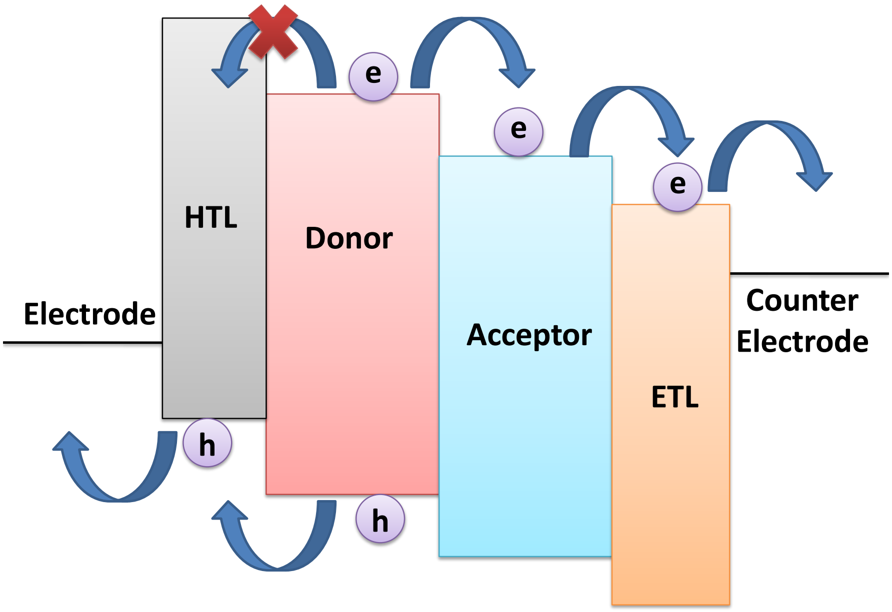

Figure 1.2.5 Schematic image of charge collection at the electrode, the current loss could be minimized by introducing buffer layer (electron transporting layer (ETL) and hole transporting layer (HTL)), charge recombination could also be suppressed.

1.2.2 Characterization of OSCs

OSCs performances are usually measured by current density-voltage (J-V) characteristics in dark or under irradiation. As shown in Figure 1.2.6, J-V curves give several parameters to characterize the performance of OSCs. Open circuit voltage (V_{OC}) is the maximum photovoltage that can be obtained in the device. On the other hand, under short circuit condition, the maximum current density can be obtained without any bias voltage is called short circuit current density (J_{SC}). The maximum of output power P_{max} is in the fourth quadrant where the product of current density and voltage reached their maximum ($J_{max} \times V_{max}$). The ratio between P_{max} and the product of J_{SC} and V_{OC} is called fill factor (FF):

$$\mathrm{FF} = \frac{J_{max} \times V_{max}}{J_{SC} \times V_{OC}}$$

The PCE (η) of OSCs is the ratio between the maximum output power and the power of the incident light:

$$\mathrm{PCE} = \frac{P_{max}}{P_{light}} = \frac{J_{SC} \times V_{OC} \times \mathrm{FF}}{P_{light}}$$

PCE of OSCs should be measured under standard conditions. The standard spectrum for solar cell calibration is air mass 1.5 (AM 1.5), the spectrum of AM 1.5 is shown in Figure 1.2.7.

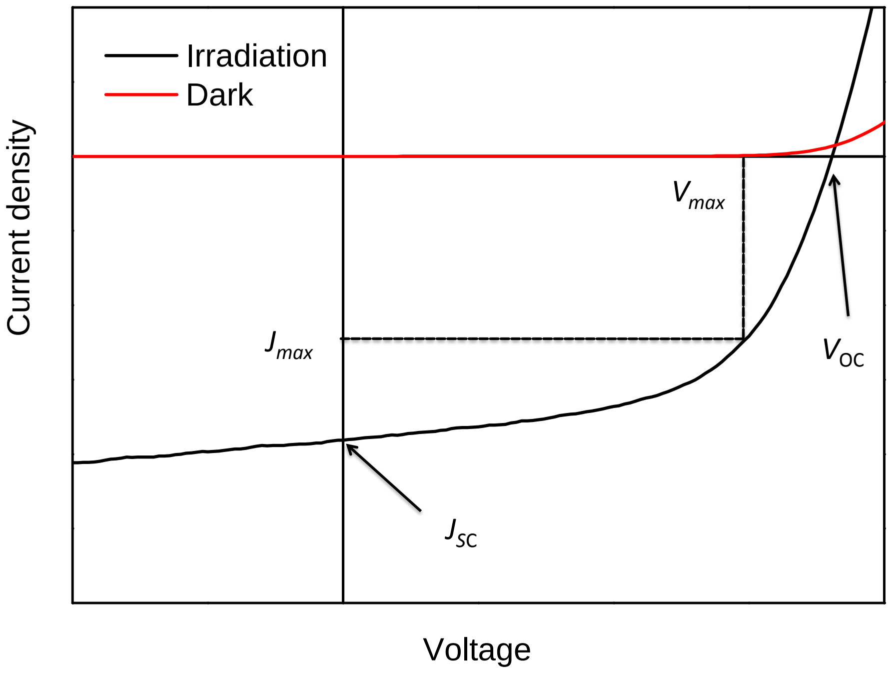

Figure 1.2.6 Typical *J*-*V* curve of OSCs in dark and under irradiation.

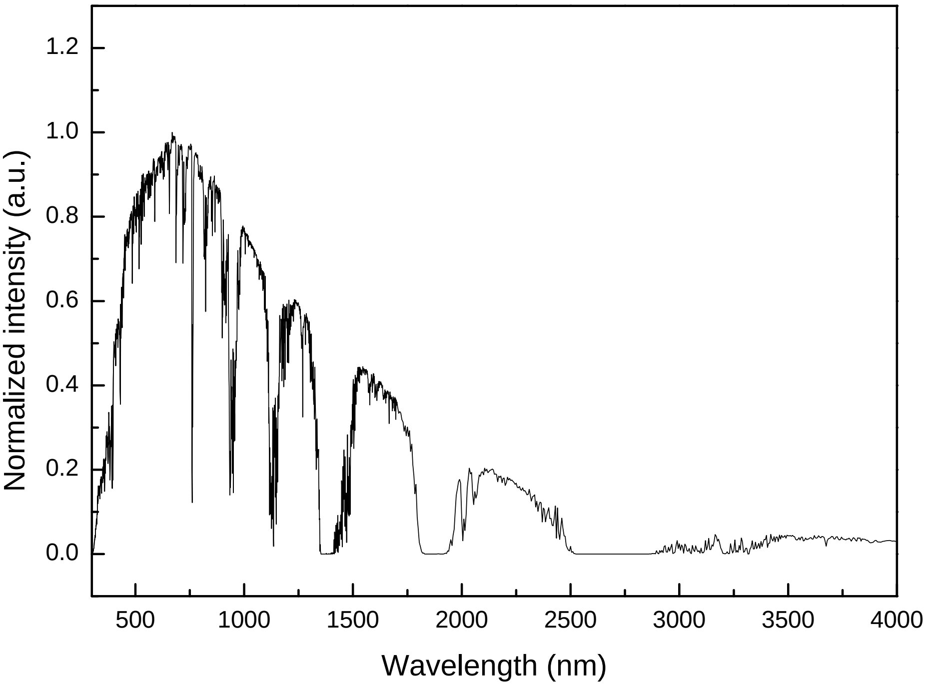

Figure 1.2.7 The spectrum of AM 1.5.

As can be easily see from above discussion, the PCE is decided by J_{SC} and V_{OC} and FF. The origin of each parameter and their physical meaning will be discussed below.

Short circuit current density (J_{SC})

J_{SC} is the maximum current attainable in OSC under zero bias. It involves multiple process such as light absorption, charge separation, recombination and charge collection. For organic semiconductors, their band gaps usually go within the visible range and therefore absorb visible light. However, most organic semiconductors have a sub-optimize band gap which has a mismatch with solar spectrum, giving rise to insufficient light absorption, especially in the near infrared region. Furthermore, in order to have enough photon absorption, a thicker organic layer would be desirable, but the charge transport problems would be caused as discussed in the former section.

Under negative bias, as I can see from Figure 1.2.6, the current obtained is usually larger than J_{SC}. This is because the negative bias offer extra electric field helping charge separation and charge collection. Under such condition, geminate recombination caused from strongly bound exciton or bimolecular recombination originated by traps could be prevented and a bias large enough could give a constant current. However, at short circuit condition, there is zero bias, the free charges are separated at D/A interface due to energy offset of D and A and sweep out by build-in potential. During these process, current loss may occur through the aforementioned recombination mechanism.

Fill factor (FF)

FF is determined by the charge carriers reaching the electrodes, when the internal field is reduced when voltage approaching open circuit condition. FF is also affected by a number of factors. Recombination often reduce FF, and also the mobility of material and balance of mobility of D and A can also affect FF. In addition, there is report using equivalent circuit mode to analyze *J*-*V* curves of OSCs and found that series resistance (R_S) and shunt resistance (R_{SH}) play a role to determine FF.[17] R_S comes from resistance of materials like ITO or organic materials, and also from the contact resistance at the interface. When R_S increases, both FF and J_{SC} would lowered. On the other hand, R_{SH} is related to the intrinsic resistance of the active layer. For example, a pin hole exist in the active layer could decrease $R_{SH.}$ When R_{SH} increases, both FF and V_{OC} would be increased. The equivalent circuit mode is given by Figure

1.2.8, and detailed analysis of OSC performance by using this mode will be discussed in the following chapter.

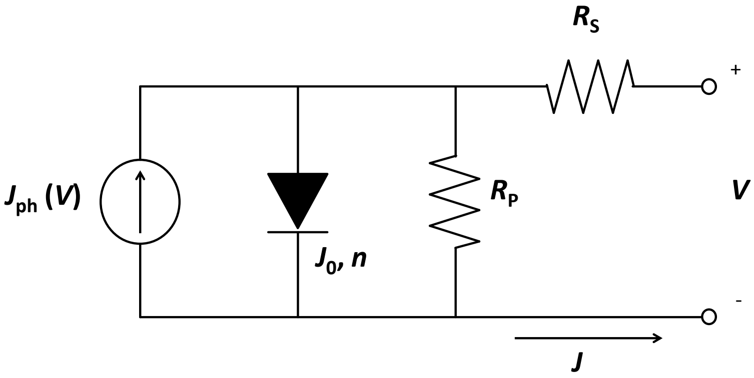

Figure 1.2.8 Equivalent circuit model used for analyzing OSCs.

Open circuit voltage (V_{OC})

Open circuit voltage of a metal-insulator-metal device is determined by the difference of the work functions of the two electrodes (Figure 1.2.9a). The search for the origin of V_{OC} in OSCs therefore begins with the relationship between V_{OC} and work function difference of electrodes. Although change of electrodes sometimes did affect V_{OC}, this is mainly due to the energy level mismatch at organic/inorganic interface, causing substantial charge recombination and therefore loss of V_{OC}. This situation can be solved by introducing ETL and HTL as I introduced in the former section. On the other hand, the voltage for a p-n junction would be confined by the n-type and p-type energy levels, namely the quasi Fermi levels of the electron and hole. As for organic solar cells, the V_{OC} was found to be linearly scaled with the different between HOMO of donor and LUMO of acceptor (E_{DA}) (Figure 1.2.9b). There are several report showing relationship between maximum V_{OC} can be obtained and D/A interface energy difference. They find for a number of systems, V_{OC} had a linear relationship with interfacial energy difference (Figure 1.2.10).[18, 19] These results suggested the E_{DA} plays an essential role in determining V_{OC} of OSCs.

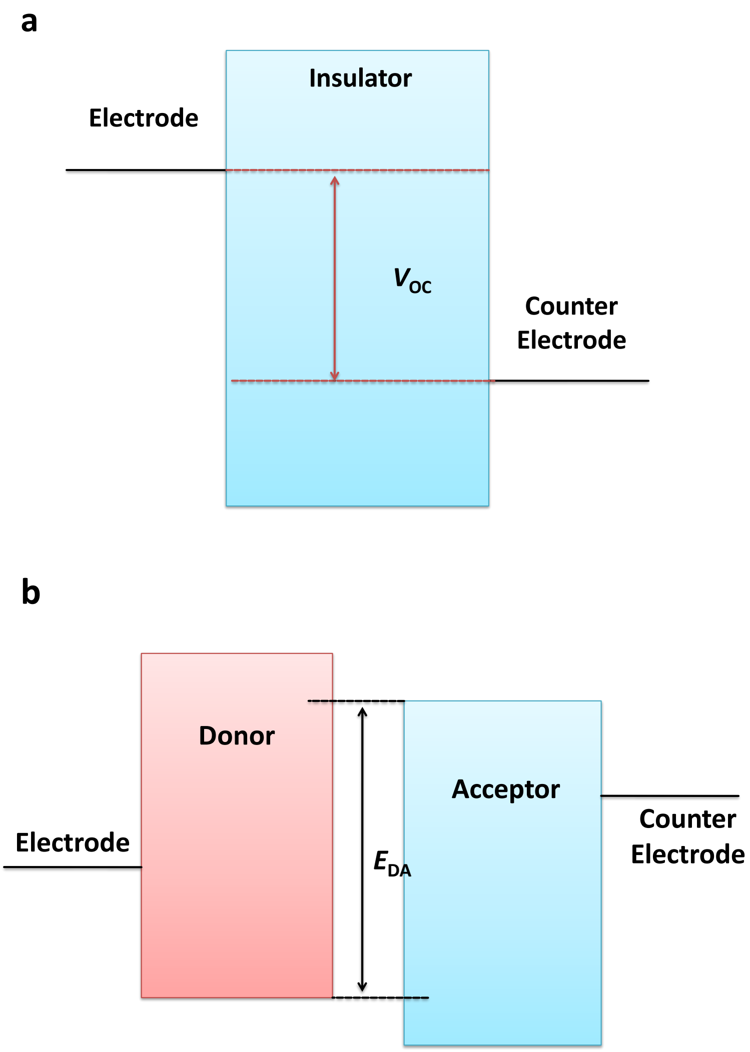

Figure 1.2.9 Schematic images of V_{OC} of metal/insulator/metal device.

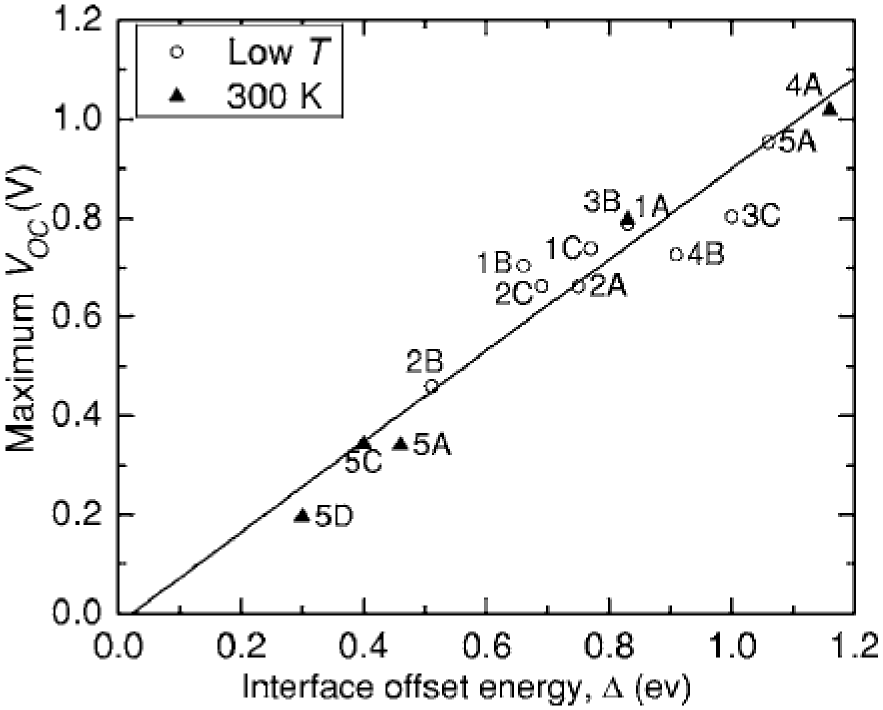

Figure 1.2.10 Dependence of V_{OC} on D/A interfacial energy difference. The closed triangles correspond to heterojunction devices for which the maximum open circuit voltage, V_{OCmax}, was measured at 300 K, whereas open circles are V_{OCmax} collected at T 300 K. The solid line shows a linear best fit to the data slope = 0.92 and intercept = 0.02. Figure is reproduced from ref. 18 with permission. Copyright 2007, American Physics Society.

External Quantum efficiency (EQE)

Quantum efficiency is one of the key indicator for performance of OSCs. It shows the current generated by the device at a given incident light wavelength. In EQE measurement, the quantum efficiency is calculated from current obtained divided by incoming photons. Therefore, the EQE is dependent on absorption of the photons and collection of the free charges. Expression of EQE is given as below:

$$\mathrm{EQE} = \frac{n_{electron}}{n_{photon}} = \frac{I_{SC} \times hc}{P_{light} \times \lambda e}$$

where $n_{electron}$ is the electrons generated by the OSCs after irradiation, n_{photon} is the number of photons from the incident light, h is the Plank constant, c is the velocity of light and e the electron charge. Furthermore, EQE spectrum of OSCs could also be used to calculate the short circuit current under the irradiation of AM1.5 (zero bias EQE).

1.2.3 Typical materials in OSCs

Active layer of OSCs comprises of a p-type materials as donor and an n-type materials as acceptor. Usually donor materials used in OSCs are semiconducting polymers which could absorb a portion of visible light. On the other hand, acceptor materials are often fullerene-based materials. Buffer layer materials in OSCs are usually metal oxides, and ITO and Al or Ag are used for electrodes. In the following paragraphs, a number of typical materials used in OSCs will be introduced.

Donor materials

PPV and its derivatives are well studied in the early stage of OSCs, and their efficiency exceed 2%.[20, 21] The chemical structure of PPV and one of its derivative MEH-PPV are shown in Figure 1.2.11. PPV is insoluble in commonly used organic solvent, therefore derivative like MEH-PPV is developed which is soluble in solvent like chlorobenzene and chloroform. These materials were well studied in the past decade, limited light absorption however, prevented its further application in OSCs.

Polythiophene, on the other hand, has a better application in OSCs. P3HT, one of the derivative of polythiophene, has absorption up to 650 nm, which almost cover the visible band, shown an improved PCE up to 4%. The key factor not only lies in the broaden absorption, but also high mobility of hole due to higher degree of crystallization of the polymer. Yang et al. reported PCE of P3HT based OSCs over 4% via self-assembly of P3HT, demonstrating the importance of crystallization of material in OSCs.[22]

PTB7 is another high efficient donor material recently reported, showing PCE higher than 7%.[23] Absorption of PTB7 extends to 750 nm, give rise to higher photo-current compared to P3HT. Furthermore, PTB7 showed face-on orientation which is beneficial for charge transport, these factors make PTB7 the most promising donor material so far and the highest PCE achieved by PTB7 based solar cell is over 9%.[24]

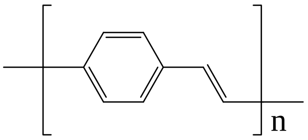

PPV

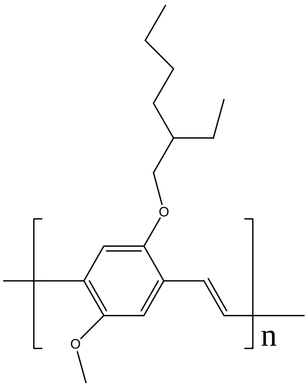

MEH-PPV

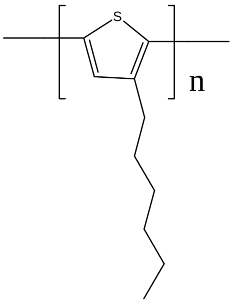

P3HT

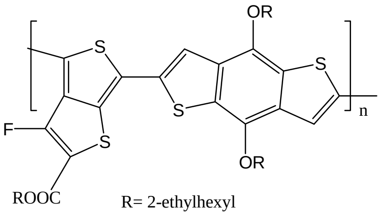

PTB7

Figure 1.2.11 Chemical structures of PPV, MEH-PPV, P3HT and PTB7.

Acceptor materials

Acceptor materials in OSCs should have an electron affinity larger than that of the photoexcited donor. The fullerene molecule and its derivatives so far have been proven the most efficient acceptor materials. The commonly used fullerene materials are given in Figure 1.2.12. These materials are soluble in common organic solvent and have high electron mobility (~0.1 cm^2/Vs). The key factor makes fullerene the most successful acceptor material might lies in the aggregation of this molecule. Durrant et al. reported pure PCBM showed a higher LUMO energy which may act as driver for charge separation in OSCs.[25] However, fullerene molecule often has weak absorption of the light, alternative acceptor materials are needed to further increase the PCE of OSCs.

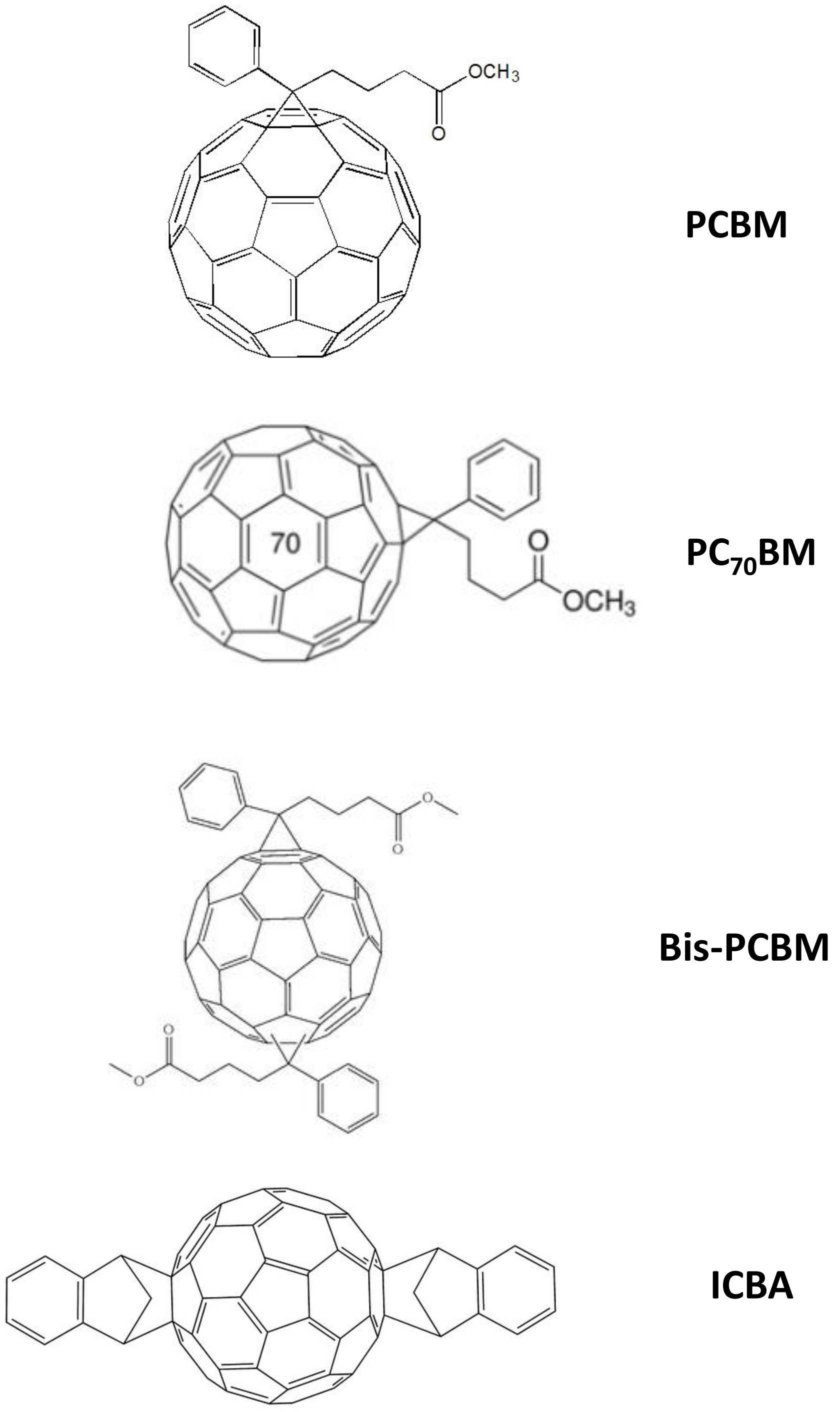

Figure 1.2.12 Chemical structures of PCBM, PC$_{70}$BM, bis-PCBM and ICBA.

Buffer layer materials

As introduced in the former section, two kinds of buffer layer materials, namely ETL and HTL are often used in OSCs. Typical HTL is PEDOT:PSS, which is highly conductive and has a good match of the energy levels with most donor polymers. However, due to its acid nature, the stability of OSCs using PEDOT:PSS is not high, therefore alternative materials like graphene oxide is used to replace it. Figure 1.2.13 showed a typical example of using graphene oxide and PEDOT:PSS for comparison.[26] OSCs with graphene oxide interlayer showed similar PCE compared with PEDOT:PSS modified OSCs. However, when these devices were exposed to air, PEDOT:PSS modified OSCs showed a substantial loss of PCE after just several hours. On the contrary, OSCs with graphene oxide interlayer showed a relatively high stability, even after 20000 minutes, PCE is still above 2%. There are other type of HTLs, metal oxides such as V_2O_5 and MoO_3 are usually used. The HTL used in OSCs not only give a better match of energy level at organic/inorganic interface for efficient charge collection, but also reduce charge recombination near electrode (mainly bimolecular recombination).

On the other hand, ETL is used for better electron collection. Typical materials like ZnO and TiO_2 are used in OSCs in the ITO side for inverted structure design. Furthermore, these ETL could also be made as nano-array to enhance charge transport, the increase of FF could be often observed in such cases. One typical example was reported by Takanezawa et al., who inserted ZnO nano-array to enhance electron transport, resulting the increase of device performance (see Figure 1.2.14).[27]

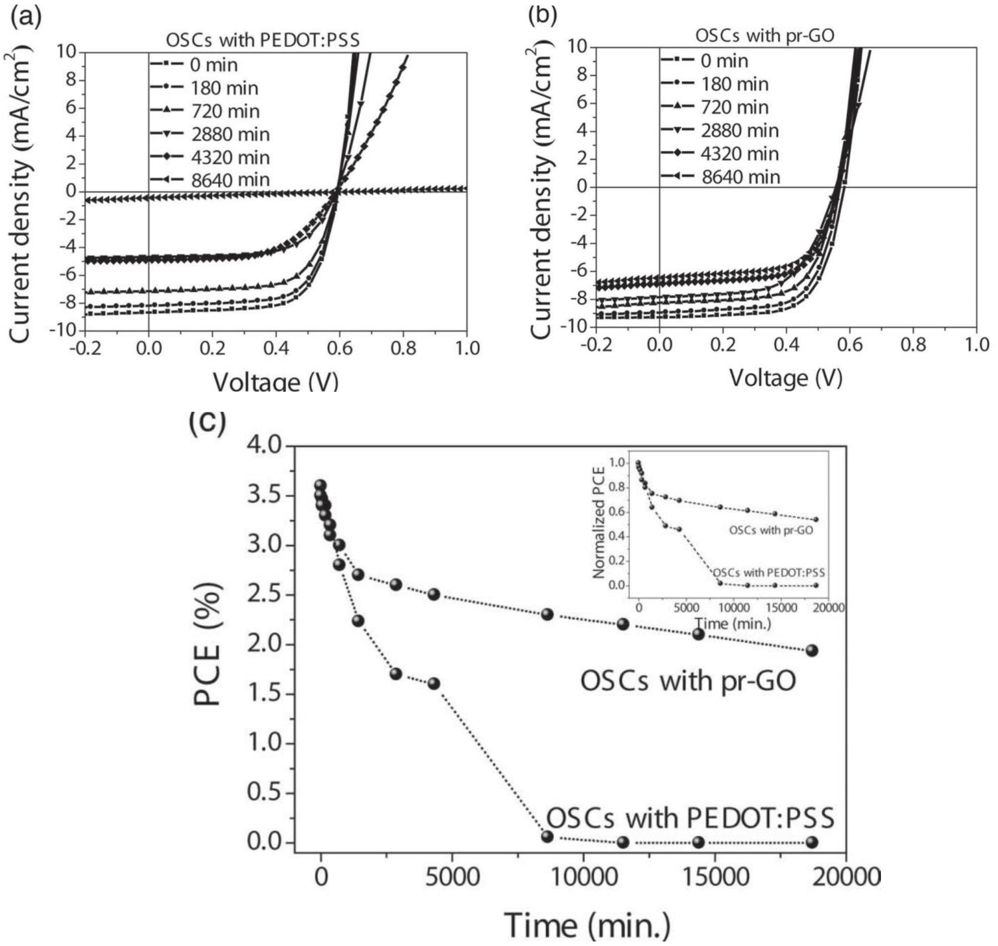

Figure 1.2.13 (a) a conventional PEDOT:PSS-based OSC and (b) an OSC with the graphene oxide anode interfacial layer. (c) Changes in PCE of a conventional PEDOT:PSS-based OSC and an OSC with the graphene oxide anode interfacial layer during exposure to air. The inset shows the normalized PCE. Figure is reproduced from ref. 26 with permission. Copyright 2011, WILEY-VCH Verlag GmbH & Co. KGaA, Weinheim.

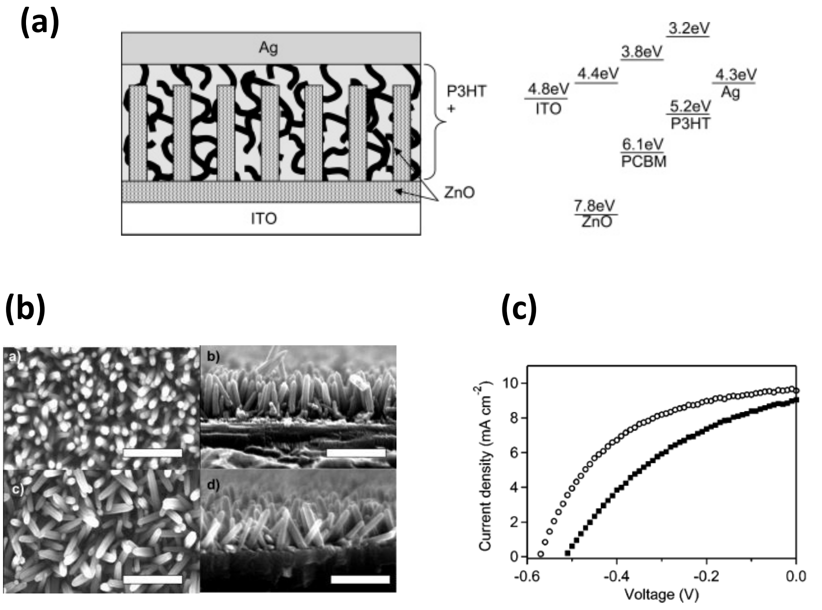

Figure 1.2.13 (a) energy diagram of the device using ZnO nano-array, (b) SEM image of ZnO nano-array, (c) enhanced device performance of OSCs with ZnO nano-array (open circle). Figure is reproduced from ref. 27 with permission. Copyright 2007. American Chemical Society.

Electrode materials

Electrode materials used in OSCs are often ITO for the anode and metals like Ag, Al and Au for cathode. The work function of these materials are given in Table 1.2.2. The work function difference between these two electrodes serves as the build in potential, sweeping out charges after their separation at D/A interface. Furthermore, the use of electrode material with deeper work function like gold can also increase stability of device in terms of oxidation of electrode material.

Table 1.2.2 Work function for different metal materials

Material	**Work function (eV)**
ITO	4.7
Al	4.3
Ag	4.3
Au	5.1

1.2.4 Device structures of OSCs

The device structure of OSCs has a large influence on its performance. In this section, the structures used in OSCs will be introduced and their effect on device performance will be discussed,

Single layer OSCs

The early stage study of OSCs used a simple structure of a light absorber polymer sandwiched by two metal electrodes. After the light absorption, the electron goes to one electrode and hole goes to the other to form photo-current, as indicated by Figure 1.2.14. This type of device rely on the difference of work function from the two electrodes to separate charges, therefore the choice of metal electrode could affect the device performance very much. Furthermore, since the electron and hole transport in the same layer, substantial recombination of these carriers could happen, and different mobility of electron and hole could also further reduce the performance. In addition, the exciton diffusion length of the polymer is usually limited, therefore the thickness of polymer must be kept thin, resulting insufficient light absorption. The performance of this type of OSCs is limited to less than 1%.[28]

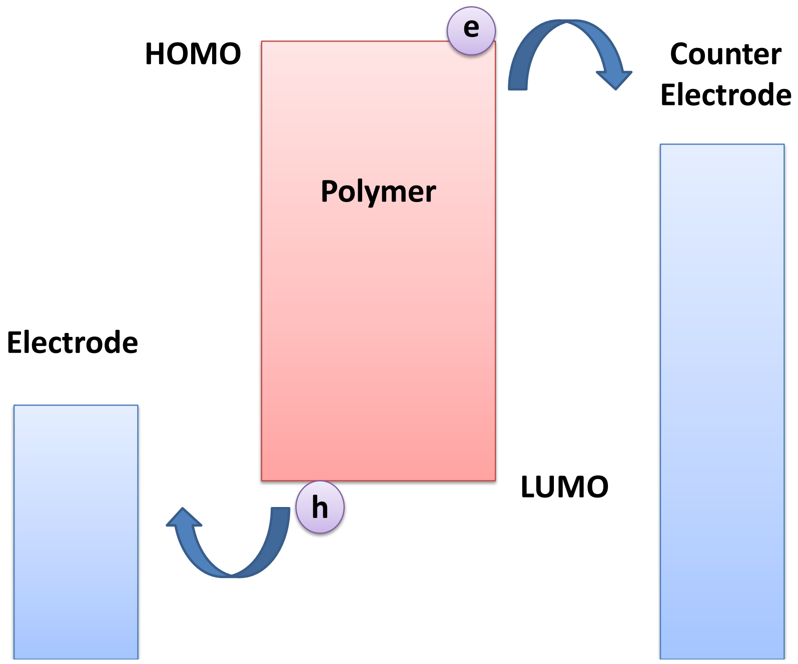

Figure 1.2.14 Schematic image of metal/polymer/metal devices.

Bilayer OSCs

In 1986, Tang reported by using of an electron donor of copper phthalocyanine and an acceptor o perylene tetracarboxylic derivative in a bilayer structure OSCs, the PCE could be higher than 1%.[1] The high charge separation efficiency in this type of cell was explained by the field at the interface between two organic materials .This result gave a new concept for increasing PCE of OSC by introducing electron acceptor materials (Figure 1.2.15). This concept has been utilized up to now to push the PCE of OSCs.

After Tang' work, the importance of concept of D/A was realized by people who work in OSC field. Sariciftci et al. reported use of polymer (MEH-PPV) as donor and C_{60} as acceptor.[29] MEH-PPV could donate electrons to fullerene and transport holes to the ITO. On the other hand, fullerene receive electrons and transport them to the electrode. PCE over 1% was achieved.

Compare to single layer device, bilayer device utilized D/A interface to increase charge separation efficiency, and electron and hole are transported by corresponding n-type and p-type materials. However, bilayer device also has its limitation. The OSCs relies on sufficient light absorption from the materials to generate current. The typical thickness required by the polymer for light absorption is around 100 nm. On the other hand, the exciton diffusion length in these materials is often limited (~10 nm). Only a portion of excitons could diffuse to D/A interface for charge separation, therefore causing loss of energy in the device.

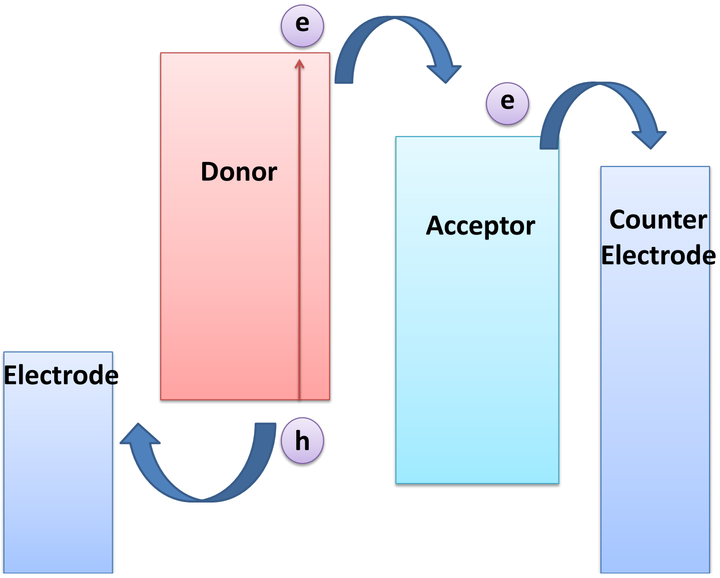

Figure 1.2.14 Schematic image of metal/donor/acceptor/metal bilayer devices.

Bulk heterojunction (BHJ) OSCs

Although charge separation was significantly enhanced in bilayer OSCs, the PCE was still limited by collection of excitons. As to solvent this problem, another device structure called bulk heterojuction OSCs was designed. In such type of OSCs, donor material and acceptor material are blended together and nano-scale phase separation could be formed (Figure 1.2.15). In such condition, a large D/A interfacial area could be obtained and the typical domain size of D and A are around several tens of nanometers, which is beneficial for exciton diffusion. In 1990s, Hiramoto and Yu et al. independently showed that by using BHJ structure the PCE could be improved compared to bilayer case.[14, 30]

In BHJ OSCs, nano-morphology control is the key factor for achieving high PCE. Certain aggregation of each material might provide charge collection path ways. On the other hand, the ideal size of domain of each material should be equivalent to its exciton diffusion length in order to maximize exciton harvesting. Usually such demand is achieved by using high boiling solvent or solvent additive to optimize morphology. Furthermore, crystallization of the polymer also plays a very important role because hole mobility of the polymer is usually lower than electron mobility of fullerene in the blend films.

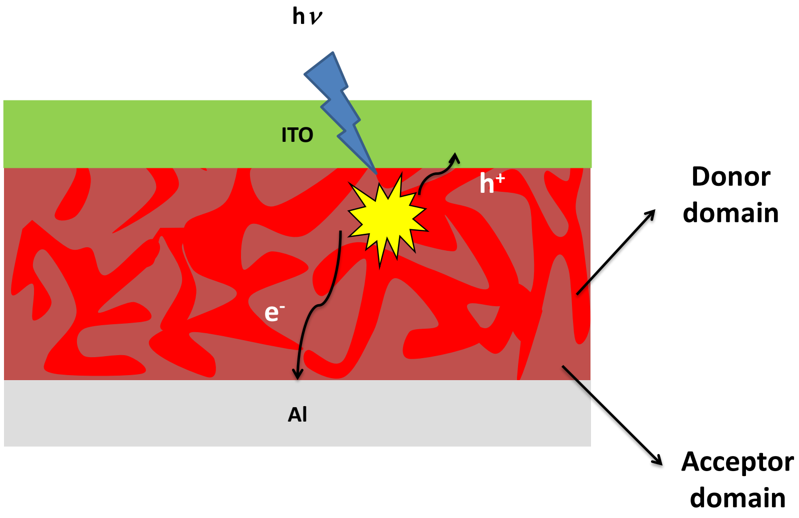

Figure 1.2.15 Schematic image of BHJ device.

Other structure OSCs

Besides commonly used BHJ OSCs, there are a number of other structure OSCs such as PIN and tandem OSCs. The former one consist of BHJ layer sandwiched by a p-type layer and n-type layer, which could help charge transport near the electrode (Figure 1.2.16).[31] Latter one consist of two sub BHJ cells, each cell utilized different materials to maximize light absorption and voltage of the cell could be the sum of these two cell under optimized condition (Figure 1.2.17).[32] Although these structures OSCs do show an enhanced PCE but their complicated processing condition limited their further application.

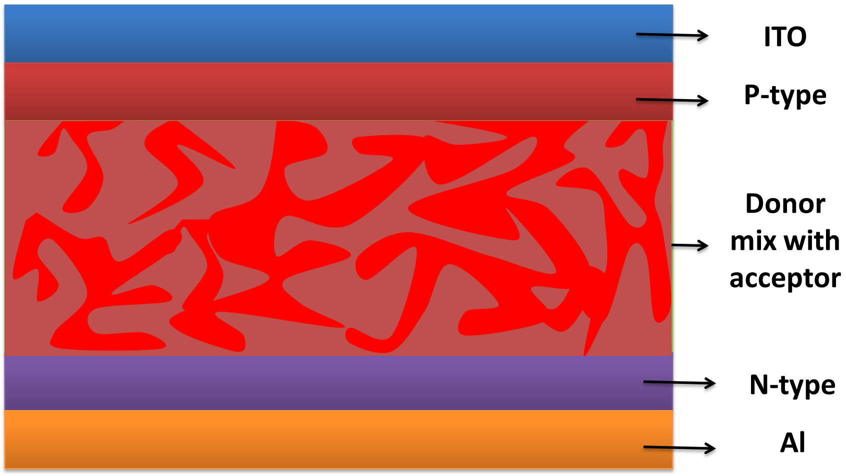

Figure 1.2.16 Schematic image of PIN device.

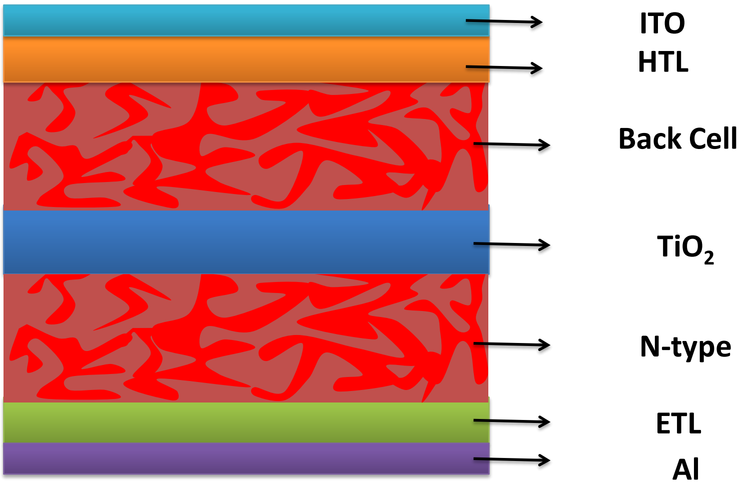

Figure 1.2.16 Schematic image of tandem device.

1.2.5 Importance of interfaces in OSCs and charge transfer state

Interfaces in OSCs

As introduced in the former sections, D/A interface has a primary importance in OSCs. The relative large binding energy of excitons in organic semiconductor relies on the energy offset at D/A interface for dissociation. Furthermore, the major loss mechanism of charge recombination also happens at this interface. The above two processes compete with each other, and significantly affect performance of OSCs. In addition, open circuit voltage of OSCs is largely related to the difference of HOMO-LUMO difference (E_{DA}) at this interface (Figure 1.2.17).

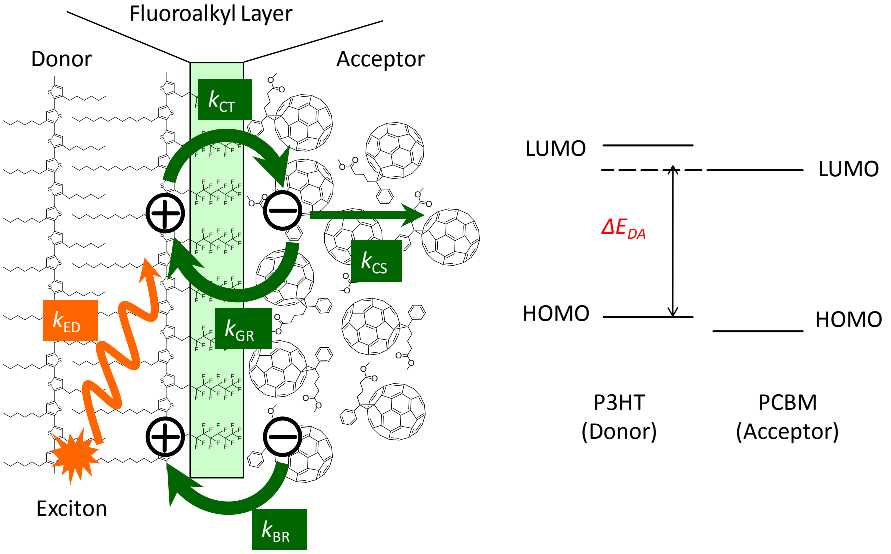

Figure 1.2.17 Schematic image of photo-physical process at D/A interface.

However, although the use of BHJ structure offer a substantial enhancement of PCE, it barely gives information on photo-physical process at D/A interface. This is largely due to the mixing manner of D and A materials, giving rise to hard access to purposely control the D/A interface. So far, the study of interface modification in OSCs mainly concentrated on organic/inorganic interface. As I induced in the former section, the energy level mismatch at organic/inorganic interface is one of the main loss mechanisms in OSCs, a substantial work has been done to solve this issue.

There are lots of examples which improve PCE of OSCs by modifying organic/inorganic interface. Some of the examples will be selectively shown here to demonstrate the effectiveness of this methodology.

Metal oxide is usually used in modifying the electrode. For the inverted structure OSCs, metal oxide like V_2O_5 and MoO_3 are often used buffer layer for modifying cathode. However, there also report by using metal oxide in the anode side in normal BHJ OSCs. As reported by Li et al., a solution-processed rhenium oxide was synthesized and applied in OSCs, resulting an increase in PCE.[33] The energy diagram is shown in Figure 1.2.17, a number of materials combination was tested by using s-ReOx as the anode buffer layer. An increase of photo-current and FF was observed for all these four materials combination (Figure 1.2.18). The improved PCE of the PSCs with s-ReOx anode buffer layer could be attributed to the suitable work function of s-ReOx layer and the enhanced absorption of the active layer in the devices with s-ReOx anode buffer.

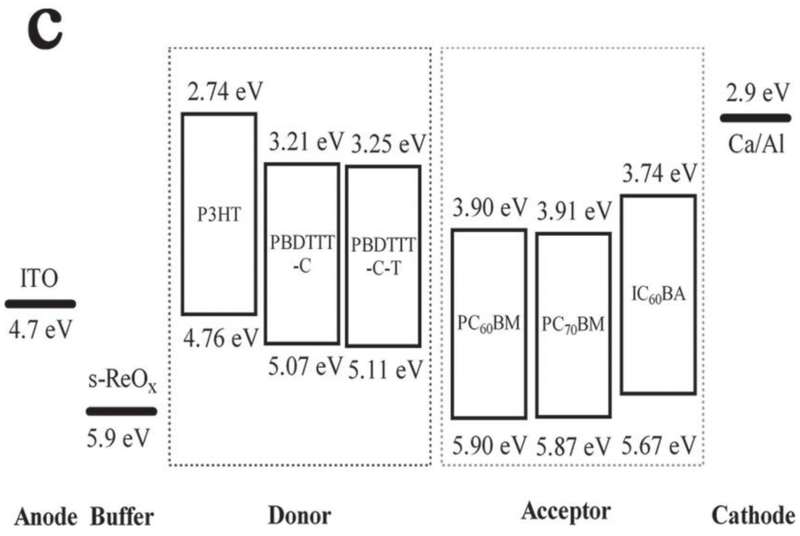

Figure 1.2.17 Energy diagram for devices with anode modification. Figure is reproduced from ref. 33 with permission. Copyright 2014, WILEY-VCH Verlag GmbH & Co. KGaA, Weinheim.

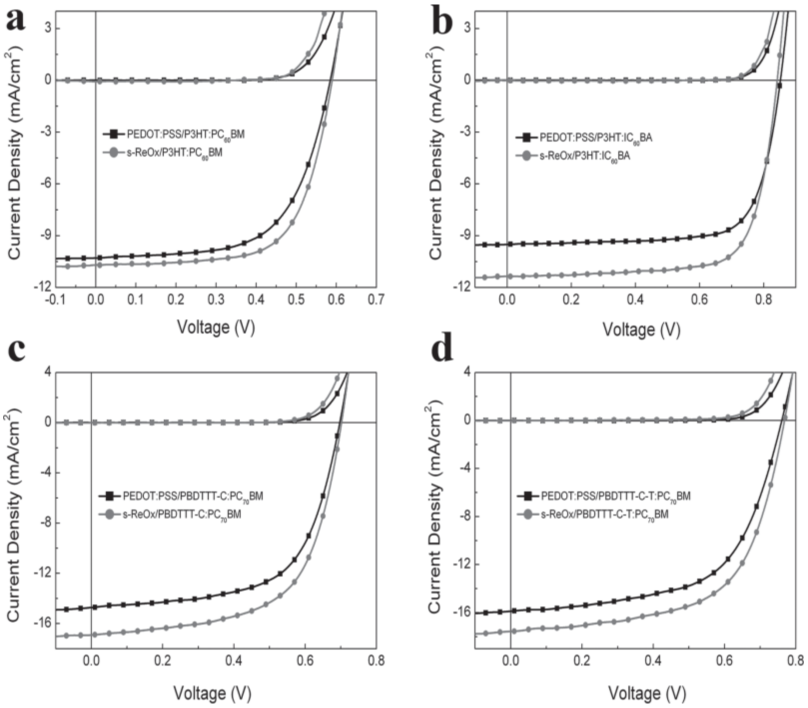

Figure 1.2.18 *J-V* curves for devices with anode modification. Figure is reproduced from ref. 33 with permission. Copyright 2014, WILEY-VCH Verlag GmbH & Co. KGaA, Weinheim.

Besides metal oxides, organic materials could also be used to modify organic/inorganic interface for better collection of charges. Li et al. reported by using one of the fullerene derivative to modifying cathode could enhance the current and FF of OSCs. The synthesis of this novel fullerene molecule and *J*-*V* curves of the device using it for cathode modification are shown in Figure 1.2.19 and Figure 1.2.20, respectively. The enhanced performance of the cell resulted from the dipole formation of fullerene interlayer shifting the energy level at organic/inorganic interface. Furthermore, comparing with the conventional cathode modifier Ca, the stability of device utilizing fullerene interlayer was significantly enhanced in the air atmosphere.

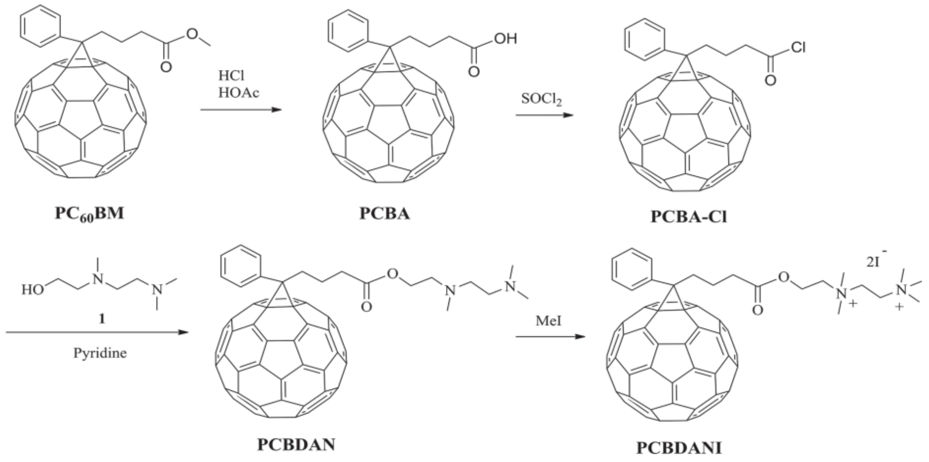

Figure 1.2.19 Synthesis of fullerene derivative used for cathode modification. Figure is reproduced from ref. 34 with permission. Copyright 2013, WILEY-VCH Verlag GmbH & Co. KGaA, Weinheim.

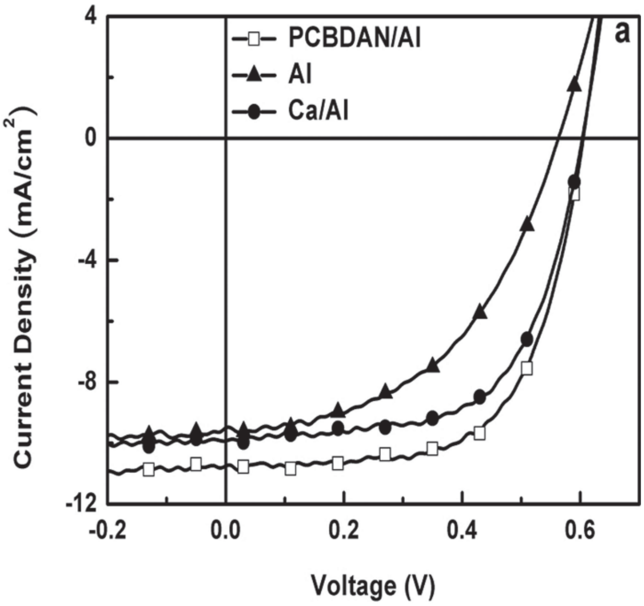

Figure 1.2.20 *J-V* curves for devices with cathode modification. Figure is reproduced from ref. 34 with permission. Copyright 2013, WILEY-VCH Verlag GmbH & Co. KGaA, Weinheim.

The above two examples showed PCE enhancement using interlayer at organic/inorganic interface. However, there is also example of modifying this interface just by polar solvent treatment. Heeger et al. reported by spin-coating polar solvent like methanol on the surface of active layer, the photo-current and FF could be increased (Figure 1.2.21).[34] The enhancement of performance was explained by the passivation of surface traps and decreased series resistance, accelerated charge extraction and reduced charge recombination (Figure 1.2.22).

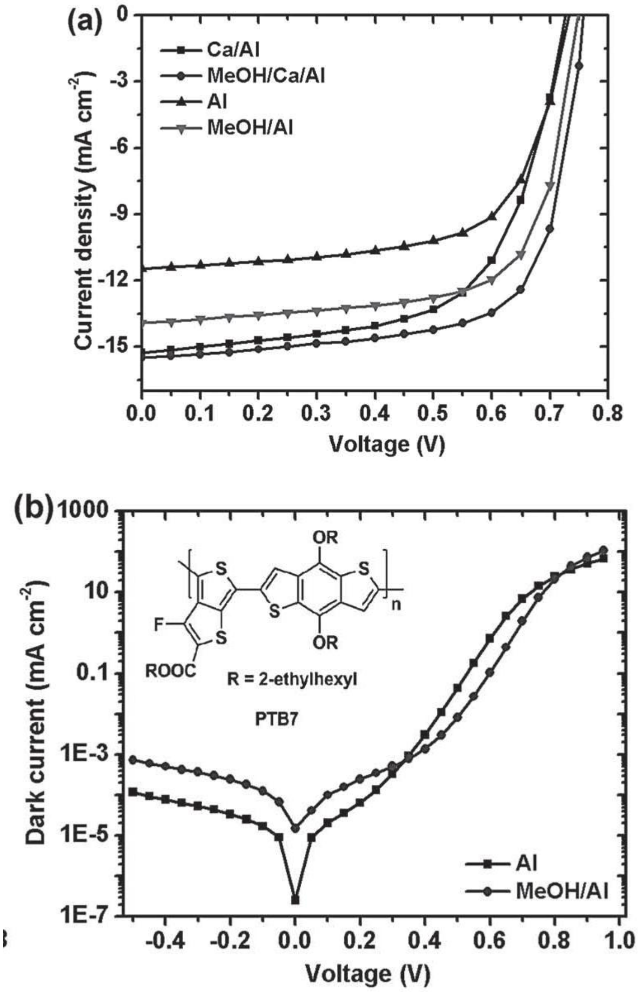

Figure 1.2.20 *J-V* curves for devices with solvent treatment. a) Under irradiation, b) in dark. Figure is reproduced from ref. 34 with permission. Copyright 2013, WILEY-VCH.

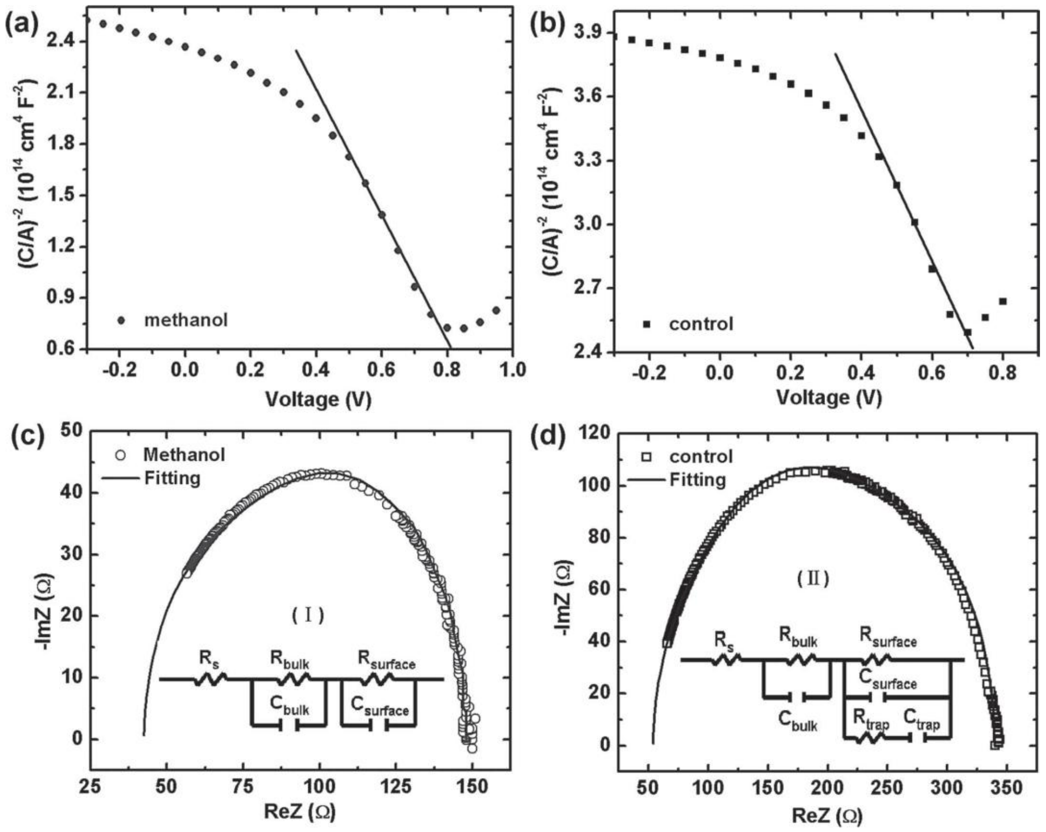

Figure 1.2.20 Impedance spectra analysis for the effect of methanol treatment on PTB7:PC$_{70}$ BM solar cell. a,b) (C/A)−2 versus applied bias voltage with (a) and without (b) methanol treatment. The solid lines correspond to Mott–Schottky plot. c,d) Niquist plots for PTB7:PC 70 BM solar cells with (c) and without (d) methanol treatment. The data are fitted by equivalent circuit models I and II separately. Figure is reproduced from ref. 34 with permission. Copyright 2013, WILEY-VCH Verlag GmbH & Co. KGaA, Weinheim

The modification of organic/inorganic interface showed substantial improvement of PCE of OSCs. Nevertheless, the increased performance mainly resulted from photo-current and FF factor, since the organic/inorganic interface mostly affect charge collection. In all these examples, open circuit voltage was barely changed since it is decided by another interface-D/A interface. So far, PCE of OSCs has already been pushed to around 10% by developing new materials and buffer layers. However, methodology like adding buffer layer cannot solve the intrinsic limitation. As indicated in Figure 1.2.21, V_{OC} of OSCs is closely related to E_{DA} at D/A interface, in order to have higher voltage, a deeper lying HOMO of donor and a shallower lying LUMO of acceptor is desirable. Simultaneously, the band gap of material decide the absorption, the smaller band gap and larger E_{DA} require a deeper lying LUMO and HOMO level of the donor. However, this demand might shrink the LUMO offset between D and A, which might weaken the driving force for charge separation in the device. Therefore, compromise between V_{OC} and J_{SC} in OSCs has to be made and eventually limited the highest PCE attainable. As I discussed above, by modifying organic/inorganic interface was no more than improving charge collection, which obviously cannot break this trade-off relationship in OSCs.

The key factor to solve this problem in OSCs lies in understanding the photo-physical processes at D/A interface. How do the charge separation and the recombination affect device performance? How to increase one parameter in OSCs without losing the others? The clue should be obtained by purposely modifying D/A interface. However, there is limited reports about D/A interfacial modification. The effect of D/A interfacial property on device performance remained obscure. This is mainly due to the BHJ structure used in OSCs. The mixture of D and A material and automatic phase separation already provide an efficient device. In addition, optimized active layer usually has nano-scale phase separation, making D/A interfacial modification difficult even in terms of material design since it require highly self-assemble for the materials.

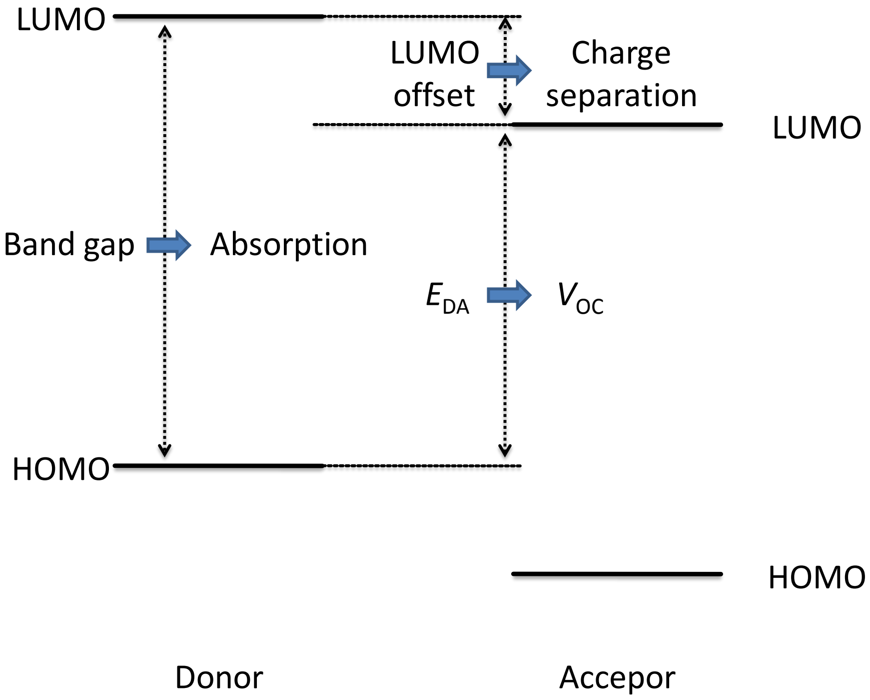

Figure 1.2.22 Schematic image of trade-off relationship between J_{SC} and V_{OC} in OSCs

A notable example of modifying D/A interface in BHJ OSCs is reported by Honda et al. who put dye molecules in P3HT:PCBM system to promote energy transfer, resulting in the enhancement of photo-current.[35-38] In the beginning of his research, two type of dye molecule, namely SiPc and ZnPc were blended with P3HT:PCBM, expecting energy transfer from P3HT to the dye molecules. The location of the dye molecules was also discussed according to the device performance (Figure 1.2.23). As shown in Figure 1.2.24, in case of ZnPc, there is degradation of device performance.

This is explained by the aggregation of ZnPc due to its planar structure preventing segregation into D/A interface. On the other hand, by blending SiPc into P3HT:PCBM, there is increase of photo-current. From EQE spectrum, the enhancement mainly comes from P3HT and dye absorption region. This suggests the increase of photo-current comprise of two parts. One is from the direct absorption of dye molecule, the other is from energy transfer from P3HT to dye. As one can see from the energy diagram in Figure 1.2.23, the hole and electron would be trapped unless the dye molecule is located at D/A interface. The location of dye therefore is expected at D/A interface. The increase of EQE response of P3HT is resulted from long range Förster resonance energy transfer. Such energy transfer requires overlap of emission of energy donor spectrum and absorption of energy acceptor spectrum. After excitation of energy donor, the exciton could be transfer to energy acceptor over a long range. In case of OSCs, this could efficiently collect those excitons which cannot reach the D/A interface for dissociation.

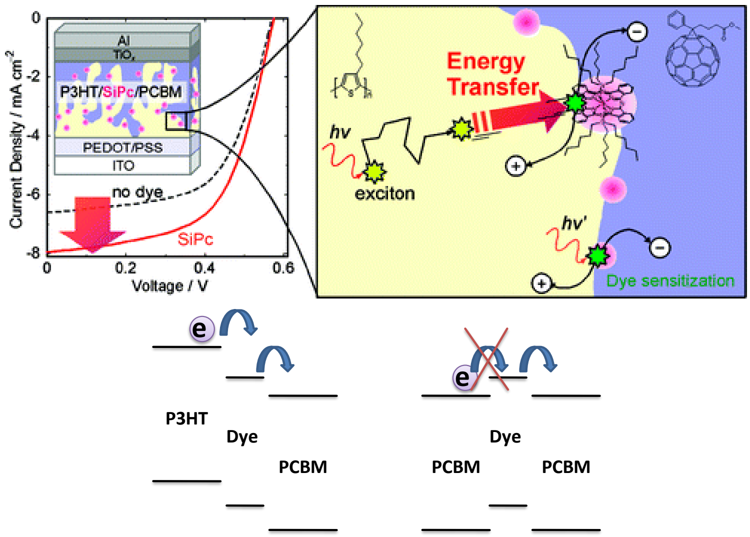

Figure 1.2.23 Energy transfer process in P3HT/SiPc/PCBM OSCs. Figure is reproduced from ref. 38 with permission. Copyright 2009, American Chemical Society.

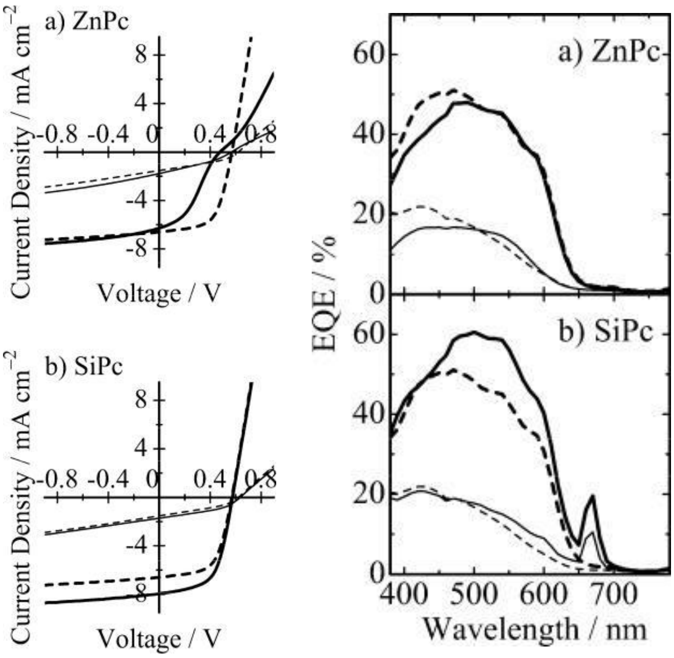

Figure 1.2.24 *J-V* curves and EQE spectrum of P3HT/SiPc/PCBM OSCs. P3HT/PCBM blend films with (solid lines) and without dye (broken lines) before (thin lines) and after annealing (thick lines): (a) P3HT/PCBM/ZnPc; (b) P3HT/PCBM/SiPc. Figure is reproduced from ref. 35 with permission. Copyright 2009, American Chemical Society.

Honda et al. later on reported study of P3HT/Dye/PCBM ternary blend solar cells with transient absorption spectroscopy (TAS).[38] Their results suggested upon polymer excitation, P3HT excitons decayed much faster in ternary blends than in binary blends with an identically rapid formation of SiPc photobleaching, indicating efficient energy transfer from P3HT to SiPc (Figure 1.2.24). They also quantified the time scale for the processes happened at D/A interface for thermal annealing and solvent annealing case (Figure 1.2.25). The driving force of location of dye molecules at D/A interface is also discussed as surface energy difference and crystallization of D and A which repel dye molecules from their domain and therefore into D/A interface.

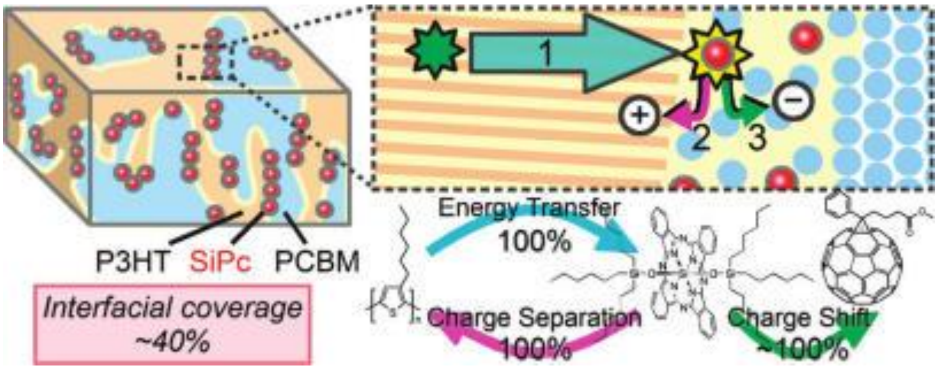

Figure 1.2.25 Schematic image of energy transfer from P3HT to dye and charge separation in P3HT/SiPc/PCBM device. Figure is reproduced from ref. 38 with permission. Copyright 2011, American Chemical Society.

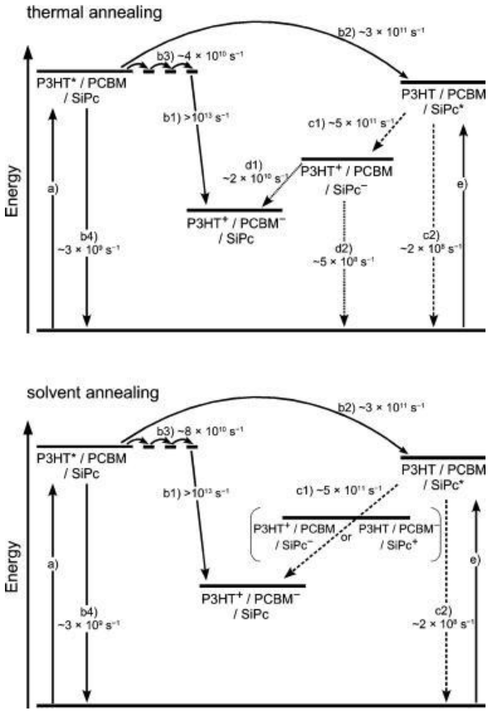

Figure 1.2.25 The scheme of light-harvesting and charge generation mechanisms in thermal-annealed (upper) and solvent-annealed P3HT:PCBM:SiPc blend films. Figure is reproduced from ref. 38 with permission. Copyright 2011, American Chemical Society.

The examples shown above indicate by purposely modifying D/A interface, PCE could be increase, more importantly, photo-physical process revealed here might potentially provide a new route to push PCE further. However, the above cases were achieved with limitations. To make third component located at D/A interface in BHJ device is really challenging, the strict requirement for the materials in term of the surface energies and system might limit the further application and research for D/A interface modification in BHJ OSCs.

On the other hand, the bilayer structure OSCs I introduced before may be a perfect model system to utilize for analyzing D/A interface. Since bilayer structure comprise of layer by layer configuration, PCE of the device might be limited the small D/A interfacial area, but a clear and well-defined D/A interface could be expected and much easier modification of D/A interface could be accessed. The bilayer device was therefore used more frequently to analyze how D/A interfacial property affect performance of OSCs.

There are several reports to date showing the D/A interface property could significantly alter device performance. McGehee et al. reported modification of TiO_2/P3HT interface with organic molecules.[39] Their results suggested that the energy offset at this interface could be tuned by interfacial dipoles, correspondingly open circuit voltage of the device is changed. The photo-current generation is also increased by modification this interface with dye molecules. A two fold increase of saturated photocurrent was achieved by modifying the TiO_2/P3HT interface. Their results suggesting that the charge separation interface has a primary importance on device performance.

Lee et al. reported by adding a ultra-thin MoO_3 layer (0.5 nm) in between CuPc/C_{60} layer, the open circuit voltage of the cell was increased from0.45 to 0.85 V.[40] The results were rationalized by the energy level change at D/A interface, their UPS and XPS results showed that E_{DA} at D/A interface was increased from 0.66 to 1.16 eV. This indicated E_{DA} has a direct impact on open circuit voltage in OSCs.

Yu et al. reported by insertion of CuPc at pentacene/C_{60} interface could enhance the open circuit voltage without obviously decrease the EQE.[41] The HOMO of CuPc is higher than pentacene, therefore open circuit voltage is increased. Furthermore, with the CuPc absorbing extra sun light, photocurrent is slightly increased. Their results suggested that constructing multiple charge separation interfaces could increase PCE of OSCs. The interlayer should have suitable energy level, and high carrier mobility. Another similar interface modification is reported by Shih et al. that potassium was used to dope CuPc/C_{60} interface, the results showed that PCE was enhanced mainly by increase of short current density.[42] Changes in binding energies, depletion capacitance, and electron and hole mobility confirmed the existence of interfacial dipoles. The electron structures like energy levels and charge transfer process was changed by K doping, combining balanced electron and hole mobility, the short circuit current was increased.

Huang et al. reported by inserting a ferroelectric dipole layer at P3H:PCBM interface showed drastic change of OSC performance.[43] Figure 1.2.26 showed the ferroelectric material and device structure they used. A very thin dipole layer was inserted between donor and acceptor materials, since the dipole layer material exhibited ferroelectric properties, the electric poling could induce the alignment of dipole moment according to the direction of electric field. The dipole layer at this interface could also give rise to a local electric field which could help charge dissociation. Various measurements were used to characterize this interlayer, and device performance was also analyzed. In Figure 1.2.27, J-V curve under irradiation and dark were shown. Before electric poling, device exhibited lower V_{OC}, J_{SC} and FF. This is due to the random orientation of dipoles and the insulating property of ferroelectric layer. However, after reverse bias poling, the device performance was drastically increased. This could be explained by the alignment of dipole under electric field. The local electric field created by the dipole layer help to dissociate charges, resulting enhancement of device performance. Dark *J-V* curves after poling also showed a reduced reverse current which can also explained the change of device performance.

However, if current hypothesis is true, the reverse bias aligning dipole could help charge separation, the forward bias should aligning dipole the opposite way and increase charge recombination. But the device performance after forward bias still showed increase of device performance compared to the case without poling. Further investigation might be needed to explain the phenomenon here.

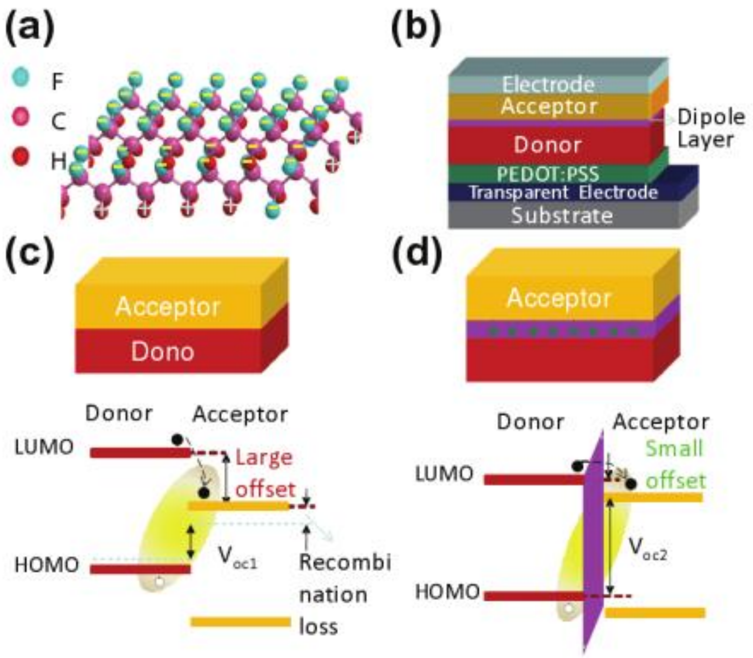

Figure 1.2.26 a) The molecular structure of a ferroelectric P(VDF-TrFE) dipole layer, b) the device structure with a dipole layer inserted between the acceptor and the donor layers, c) and d): the energy level diagram of the semiconductor heterostructure without and with a dipole layer inserted between the acceptor and the donor layers. Figure is reproduced from ref. 43 with permission. Copyright 2012, WILEY-VCH Verlag GmbH & Co. KGaA, Weinheim.

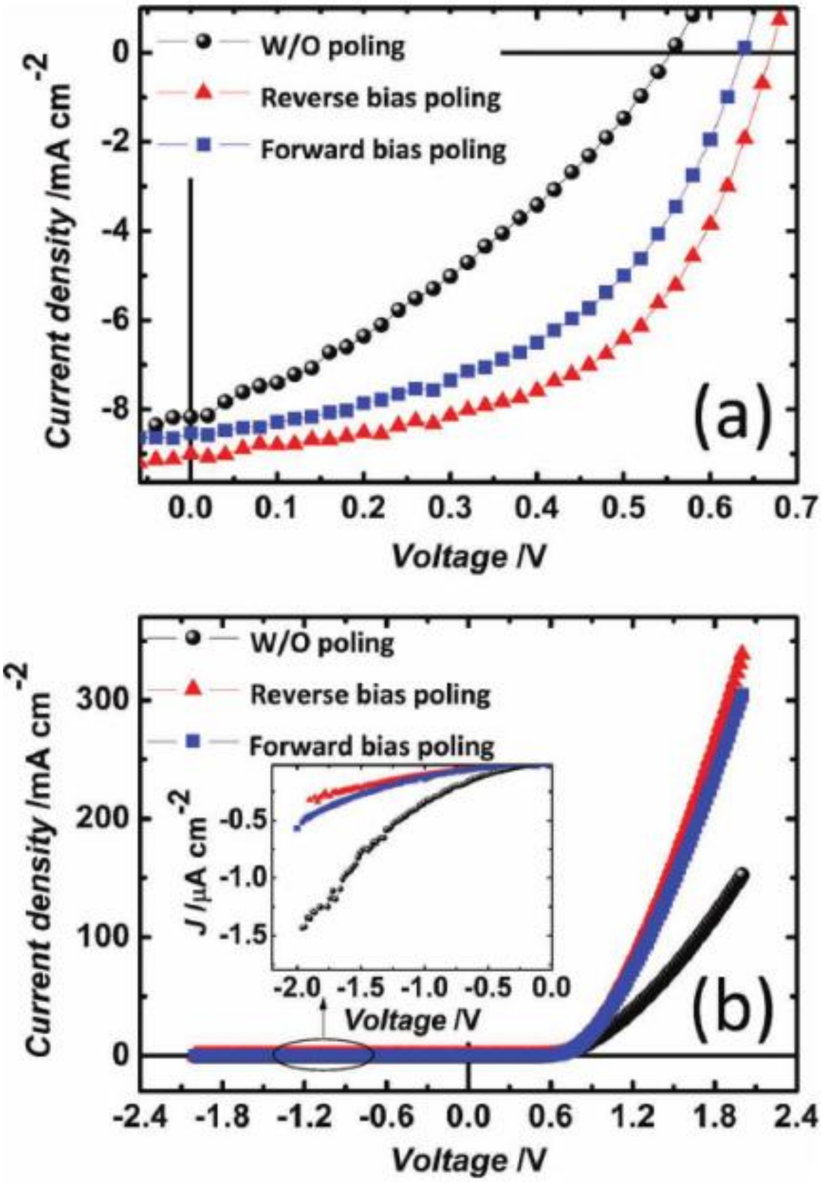

Figure 1.2.27 Device performance variation with the insertion of 1 ML P(VDF-TrFE) dipole layer between P3HT and PCBM layers: a) J–V curves under the simulated Air Mass 1.5 Global Irradiation (100 mW cm−2) for the as made trilayer device (black balls), after poling the P(VDF-TrFE) layer with reverse bias (red triangles) and forward bias pulses (blue squares), respectively; b) *J*–*V* curves in dark of the device under the three poling conditions. Figure is reproduced from ref. 43 with permission. Copyright 2012, WILEY-VCH Verlag GmbH & Co. KGaA, Weinheim.

The examples showed above clearly indicated that the D/A interfacial property could affect device performance of OSCs drastically. More importantly, the process involved are key process like charge separation and recombination. By tuning this process could potentially minimize the energy loss in OSCs and find a new route to optimize the device performance.

Charge transfer state

As mentioned in the previous section, charge transfer state (CT state) is an intermediate state refers to the state right after electron transfer from donor to acceptor. After the formation of CT state, the bonded electron-hole pair might either get separated or recombine to the ground state, therefore this process has a primary importance for generating free charges in OSCs.

However, the above statement is just a simple scenario. Friend et al. reported by pump push measurement, a multiple state was detected at D/A interface after excitation.[44] As indicated by Figure 1.2.28, after excitation, the S_1 state will go to CT state, however, initially CT_n state is a hot state which is a higher lying energy state. Within a short time, CT_n state relaxed to CT_0 state, which is a lower lying energy state. By push probe, the lower lying CT state could be push to CS state. For higher lying CT state, charge separation could proceed due to the downhill process in energy. For the lower lying state, on the other hand, charges could recombine because the energy of CT state (E_{CT}) is lower than CS state. As shown in Figure 1.2.29, for lower lying CT state, the charge separation distance is shorter, indicating more localized CT state.

In this case, charges are more likely to recombine due to the large coulomb interaction. However, for higher lying CT state, charges are more spatially separated, indicating more localized CT state, resulting efficient charge separation.

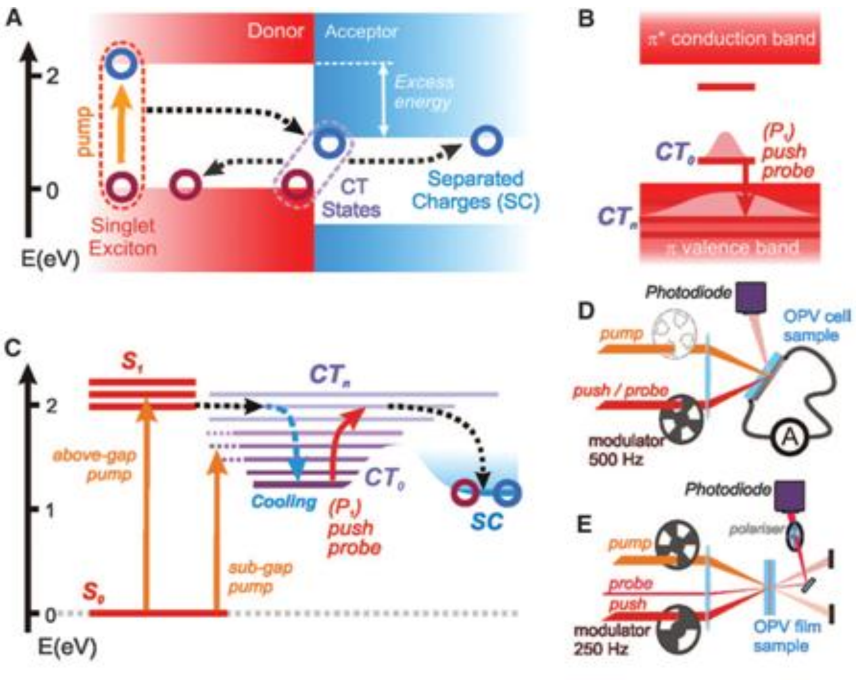

Figure 1.2.28 (A and B) Band diagrams for (A) a typical OPV and (B) a cationic state on the polymer donor. (C) Free energy state diagram of the same OPV system. Singlet, charge-transfer (CT; lowest-lying, CT0; band states, CTn) and separated-charges (SC) states are shown; positive charge density distribution in (B) is indicated by pink contour. Solid arrows show optical transitions, and dashed arrows indicate energy- and charge-transfer pathways involved in photoconversion. Layouts of (D) pump-push photocurrent and (E) three-pulse transient-anisotropy experiment. Figure is reproduced from ref. 44 with permission. Copyright 2012. American Association for the Advancement of Science.

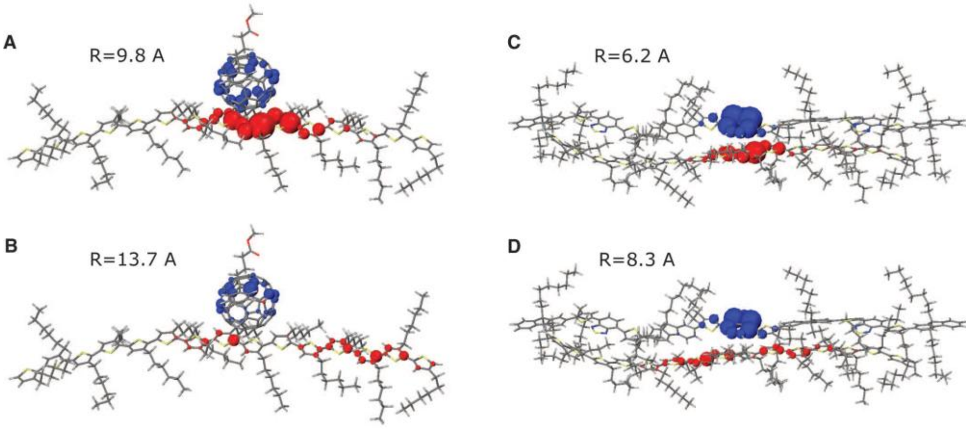

Figure 1.2.28 (A and B) Microelectrostatic simulations of the charge distribution at the P3HT/ PCBM (A and B) and P3HT/F8TBT (C and D) heterojunction, with electron and hole densities shown in blue and red, respectively. (A and C) Charge distribution in the lowest CT-state configuration, and (B and D) in the excited CTstate configuration created upon absorption of an IR-push photon. R, average electron-hole separation. Figure is reproduced from ref. 44 with permission. Copyright 2012. American Association for the Advancement of Science.

In the above report, the energy offset at D/A interface seemed less important since the CT state could be initially hot. This phenomenon has also been discussed by other groups. Durrant et al. reported that for the systems that exhibit the smallest LUMO offset, the photocurrent quantum yield decreases as the photon excitation energy is reduced toward the band gap, but the yield of bound, interfacial charge transfer states rises.[45] The initial energy of excitons could lead to a hot state in which the energy could be used for charge separation.(Figure 1.2.29) This scenario is quite similar as reported by Friend et al.

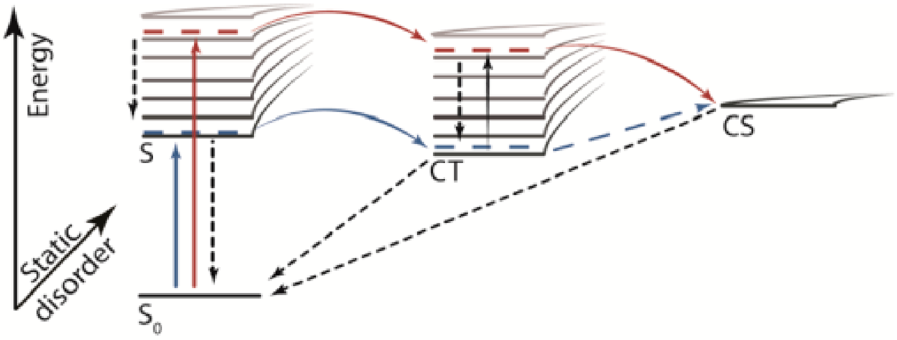

Figure 1.2.29 Energy level diagram depicting two charge separation processes initiated by light excitations using photons with high energy (red arrows) and low energy (blue arrows). Figure is reproduced from ref. 45 with permission. Copyright 2012. American Chemical Society.

Besides these reports, there are other groups using spectroscopy analysis to reveal CT state in terms of time scale. Zhu et al. reported that for initial excitation on phthalocyanine, hot CT excitons are formed in 10^{-13} s, followed by relaxation to lower energies and shorter electron–hole distances on a 10^{-12} s timescale.[46] The relaxation of hot CT state might limit the time for competitive charge separation channels that can give rise to higher current generation. (Figure 1.2.30)

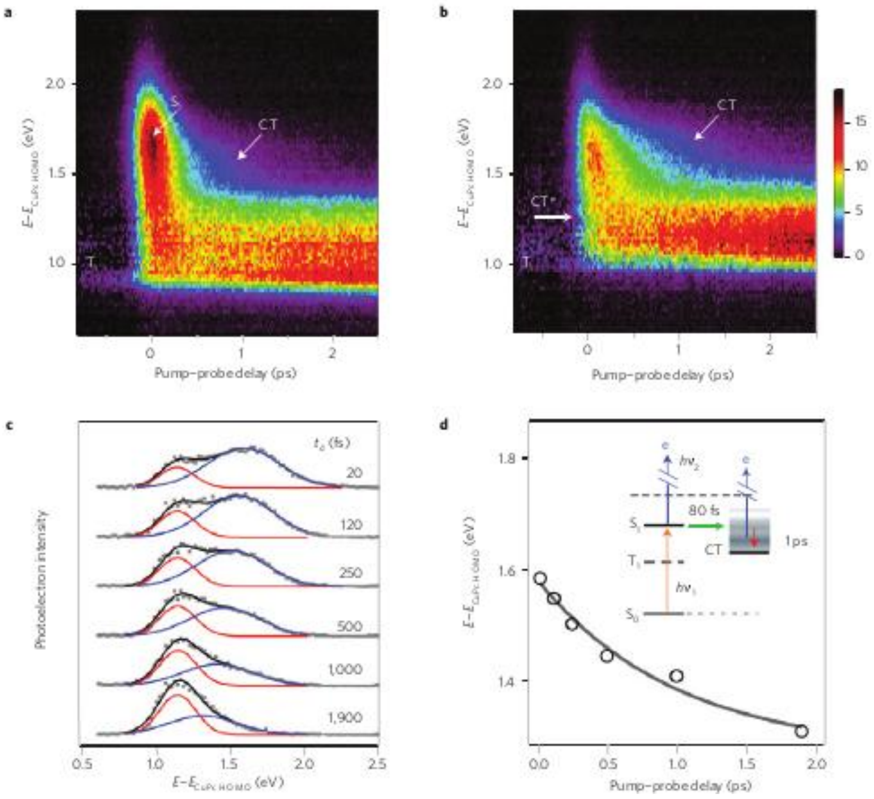

Figure 1.2.30 TR-2PPE spectra of D/A interfaces showing hot CT excitons. a, Pseudo-colour plot of TR-2PPE spectra of monolayer CuPc on C60 .b, Pseudo-colour plot of TR-2PPE spectra of monolayer C60 on CuPc. The electron energy in the intermediate state is referenced to the highest occupied molecular orbital of CuPc, as determined in ultraviolet photoemission (see Supplementary Fig. S1). Note the different energetic cutoff in signal between a and b due to the difference in workfunction. c, 2PPE spectra (dots, vertical cuts of b) at the indicated pump–probe delay times (±20 fs). The red and blue curves are components in double-Gaussian fits (black) to the data. d, The position of the CT state (circles) as a function of pump–probe delay. Figure is reproduced from ref. 46 with permission. Copyright 2013. Nature materials.

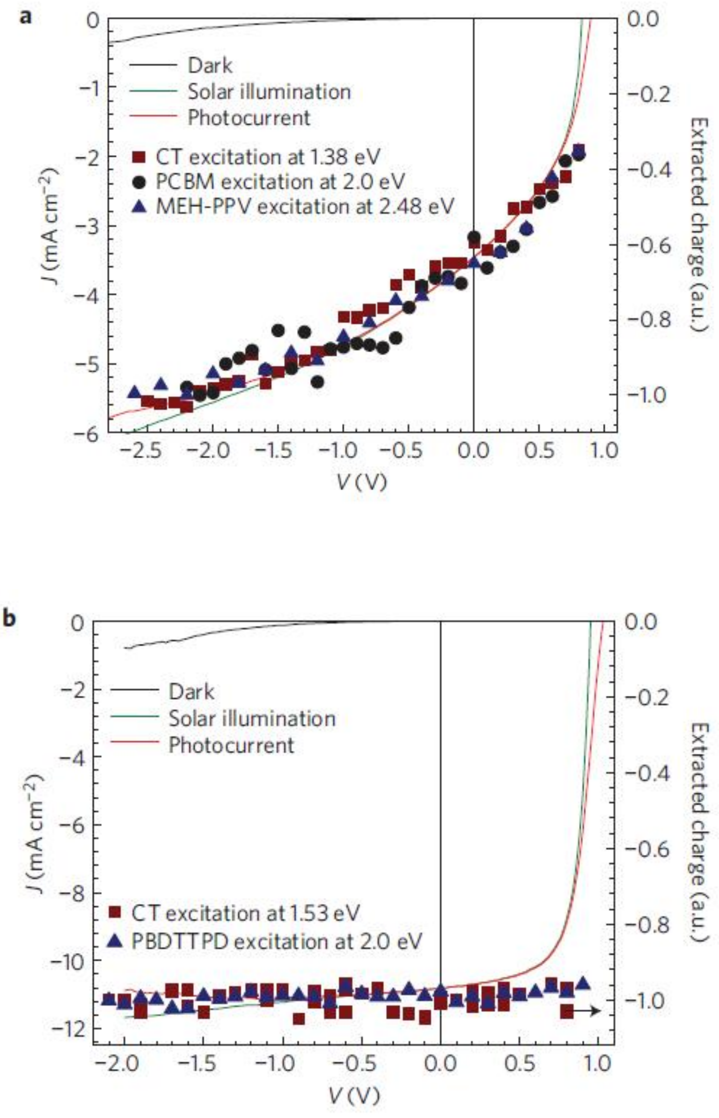

Figure 1.2.31 Current density and relative number of photogenerated charge carriers as a function of applied voltage. **a**,**b**, *J–V* curves in the dark and under solar illumination for a solution-processed MEH-PPVVPC61BM device (**a**) and for a PBDTTPDVPC61BM device (**b**). The relative number of generated charge carriers, extracted in the TDCF experiment as a function of applied bias, is shown on the right axis, for dominant excitations of D_, A_ and those directly into the CT band (at 1.38 eV for MEH-PPVVPC61BM and 1.5 eV for PBDTTPDVPC$_{61}$BM). Figure is reproduced from ref. 47 with permission. Copyright 2014. Nature Materials.

Salleo et al. reported although the hot CT states will fall into lower lying CT state, but it does not necessarily hamper charge separation.[47] Their results suggested that even with lower lying CT state, the charge separation efficiency could still be high. The point here lies in whether such lower lying CT state is delocalized enough for further charge separation or not. In Figure 1.2.31, they measurement two systems which showed lower lying CT state. However one of them showed efficient charge separation, the other showed field dependent charge separation. The results were rationalized by the energetic location of cold CT state. Their results indicated it's important to have delocalized state for CT state which is the key factor for charge separation.

The CT state plays an important role in OSCs since it decides charge separation efficiency. How to make CT state more delocalized is a challenging and key process in OSCs for further enhancement of PCE.

1.3 Research objectives

From the former sections, I can see lots of factors affecting device performance simultaneously. Common strategies to improve efficiency of device like developing low band gap polymer or new buffer layer have already been well established, and device performance was indeed improved. However, there were certain limits for these strategies. From Figure 1.2.22, I can easily imagine the trade-off relationship between V_{OC} and J_{SC}, and the common strategies cannot solve this issue since they are basically playing with energy levels of materials. How to avoid such trade-off relationship, or in other words, how to increase one parameter without losing the other is the problem I need to face right now.

In this thesis, I delicate to solve the above trade-off relationship and improve device performance. In order to do that, I purposed two strategies, namely D/A interfacial modification and crystallization of materials. The key here to solve trade-off relationship lies in controlling photo-physical process happening at D/A interface. Since E_{CT}, charge separation and recombination have critical influence on V_{OC} and J_{SC} of device, purposely using D/A interfacial modification and crystallization of materials as tools to control these process might give us a chance to avoid trade-off relationship and ultimately improve device performance.

In following chapters, I will first give an example how to introduce D/A interfacial modifications in bilayer device, and correlate interfacial property with device performance. In the next step, I propose the concept of "ideal interface" which helps to avoid trade-off relationship and improve device performance. In the last chapter, crystallization of fullerene was utilized as a new strategy to improve performance of both bilayer and BHJ device.

References

1. C. W. Tang, Applied Physics Letters **48** (2), 183 (1986).
2. M. Knupfer, Applied Physics a-Materials Science & Processing **77**, 623 (2003).
3. L. E. Lüer, H. J. Oelkrug, D. Cerullo, G. Lanzani, G. Huisman, B. H. de Leeuw, D., Organic Electronics **5**, 83 (2004).
4. J. E. S. Kroeze, T. J. Vermeulen, M. J. W. Warman, J. M., Journal of Physical Chemistry B **107**, 7696 (2003).
5. S. E. Webber, Chemical reviews **90**, 1469 (1990).
6. L. Onsager, Physical Review **54**, 554 (1938).
7. T. M. C. a. J. R. Durrant, Chemical Reviews **110**, 6736 (Chem. Rev. 2010, 110).
8. M. J. Tachiya, Chemical Physics **89**, 6929 (1988).
9. P. M. A. Borsenberger, A. I., Journal of Applied Physics **50**, 909 (1979).
10. K. M. N. Hong, J., Journal of Chemical Physics **69**, 5026 (1978).
11. J. B. Singh, H., Phys. Status Solidi b **63**, 425 (1974).
12. V. D. K. Mihailetchi, L. J. A. Hummelen, J. C. Blom, P. W. M., Physical Review Letters **93**, 216601 (2004).
13. C. L. Braun, Journal of Chemical Physics **80**, 4157 (1984).
14. J. G. G. Yu, J. C. Hummelen, F. Wudi, A. J. Heeger, Science **270**, 1789 (1995).
15. H.-L. Y. a. A. K.-Y. Jen, Energy Environ. Sci. **5**, 5994 (2012).
16. J. W. V. D. Mihailetchi, and P. W. M. Blom, Physical Review Letters **94**, 126602 (2005).
17. B. Q. a. J. Wang, Physical Chemistry Chemical Physics **15**, 8972 (2013).
18. B. P. Rand, D. P. Burk, S. R. Forrest, Physical Review B **75**, 115327 (2007).

19. D. M. M. C. Scharber, M. Koppe, P. Denk, C. Waldauf, A. J. Heeger andC. J. Brabec, Advanced Materials **18**, 789 (2006).

20. M. T. Rispens, A. Meetsma, R. Rittberger, C. J. Brabec, N. S. Sariciftci and J. C. Hummelen, Chemical Communications (17), 2116 (2003).

21. T. Offermans, S. C. J. Meskers and R. A. J. Janssen, Organic Electronics **8** (4), 325-335 (2007).

22. G. Li, V. Shrotriya, J. Huang, Y. Yao, T. Moriarty, K. Emery and Y. Yang, Nature Materials **4** (11), 864-868 (2005).

23. Y. Liang, Z. Xu, J. Xia, S.-T. Tsai, Y. Wu, G. Li, C. Ray and L. Yu, Advanced Materials **22** (20), E135-E138 (2010).

24. C. Z. Zhicai He, Shijian Su, Miao Xu, Hongbin Wu and Yong Cao, Nature Photonics **6**, 591 (2012).

25. F. C. Jamieson, E. B. Domingo, T. McCarthy-Ward, M. Heeney, N. Stingelin and J. R. Durrant, Chemical Science **3** (2), 485 (2012).

26. J.-S. Y. Jin-Mun Yun, Juhwan Kim, Hyung-Gu Jeong, Dong-Yu Kim, Yong-Jin Noh, Seok-Soon Kim, Bon-Cheol Ku and Seok-In Na, Advanced Materials **23**, 4923 (2011).

27. K. H. Kazuko Takanezawa, Qing-Shuo Wei, Keisuke Tajima, and and K. Hashimoto, J. Phys. Chem. C **111**, 7218 (2007).

28. G. T. S. Glenis, F. Garnier, Thin Solid Films **139**, 221 (1986).

29. N. S. Sariciftci, D. Braun, C. Zhang, V. I. Srdanov, A. J. Heeger, G. Stucky and F. Wudl, Applied Physics Letters **62** (6), 585 (1993).

30. M. Hiramoto, H. Fujiwara and M. Yokoyama, Applied Physics Letters **58** (10), 1062

(1991).

31. H. M. H. Inho Kim, Jian Li, Ghassan E. Jabbour, Applied Physics Letters **97**, 203301 (2010).

32. J. Y. Kim, K. Lee, N. E. Coates, D. Moses, T. Q. Nguyen, M. Dante and A. J. Heeger, Science **317** (5835), 222-225 (2007).

33. Z. a. Tan, L. Li, F. Wang, Q. Xu, S. Li, G. Sun, X. Tu, X. Hou, J. Hou and Y. Li, Advanced Energy Materials **4** (1), n/a-n/a (2014).

34. H. Zhou, Y. Zhang, J. Seifter, S. D. Collins, C. Luo, G. C. Bazan, T.-Q. Nguyen and A. J. Heeger, Advanced Materials **25** (11), 1646-1652 (2013).

35. S. Honda, T. Nogami, H. Ohkita, H. Benten and S. Ito, ACS Applied Materials & Interfaces **1** (4), 804-810 (2009).

36. S. Honda, H. Ohkita, H. Benten and S. Ito, Chemical Communications **46** (35), 6596 (2010).

37. S. Honda, H. Ohkita, H. Benten and S. Ito, Advanced Energy Materials **1** (4), 588-598 (2011).

38. S. Honda, S. Yokoya, H. Ohkita, H. Benten and S. Ito, The Journal of Physical Chemistry C **115** (22), 11306-11317 (2011).

39. C. Goh, S. R. Scully and M. D. McGehee, Journal of Applied Physics **101** (11), 114503 (2007).

40. Z. T. Liu, M. F. Lo, H. B. Wang, T. W. Ng, V. A. L. Roy, C. S. Lee and S. T. Lee, Applied Physics Letters **95** (9), 093307 (2009).

41. J. Y. Jiang Huang, Zhiqiang Guan, and Yadong Jiang, Applied Physics Letters **97**, 143301

(2010).

42. C.-F. Shih, K.-T. Hung, H.-J. Chen, C.-Y. Hsiao, K.-T. Huang and S.-H. Chen, Applied Physics Letters **98** (11), 113307 (2011).

43. B. Yang, Y. Yuan, P. Sharma, S. Poddar, R. Korlacki, S. Ducharme, A. Gruverman, R. Saraf and J. Huang, Advanced Materials **24** (11), 1455-1460 (2012).

44. A. R. Artem A. Bakulin, Vlad G. Pavelyev, Paul H. M. van Loosdrecht, Maxim S. Pshenichnikov, Dorota Niedzialek, Jérôme Cornil, David Beljonne, Richard H. Friend, Science **335**, 1340 (2012).

45. S. D. Dimitrov, A. A. Bakulin, C. B. Nielsen, B. C. Schroeder, J. Du, H. Bronstein, I. McCulloch, R. H. Friend and J. R. Durrant, Journal of the American Chemical Society **134** (44), 18189-18192 (2012).

46. A. P. W. Askat E. Jailaubekov, John R. Tritsch,Wai-Lun Chan, Na Sai, Raluca Gearba, and K. J. W. Loren G. Kaake, Kevin Leung, Peter J. Rossky and X-Y. Zhu, Nature Materials **12**, 66 (2013).

47. S. A. Koen Vandewal, Eric T. Hoke, Kenneth R. Graham, JohannesWidmer,, M. S. Jessica D. Douglas, William R. Mateker, Jason T. Bloking, George F. Burkhard,, J. M. J. F. Alan Sellinger, Aram Amassian, Moritz K. Riede, Michael D. McGehee, and D. N. a. A. Salleo, Nature Materials **13**, 63 (2014).

Chapter 2. Electric Field-Induced Dipole Switching at the Donor/Acceptor Interface in Organic Solar Cells

2.1 Introduction

D/A interface has played a very important role in device performance of OSCs. Open circuit voltage of the device is affected by many factors. Among them, energy levels at D/A interface is of vital importance. It is generally believed that the energy level difference between HOMO of D and LUMO of A (E_{DA}) defines the maximum V_{OC} attainable in OSCs. Usually, V_{OC} of OSCs could be changed by alternation of materials combination, therefore design of new material with suitable energy levels is favorable.

On the other hand, for the same combination of materials, the V_{OC} is usually stable under well optimized condition, since it is mainly determined by the energy levels of materials. Although sometimes factors like crystallization of the materials might change the band gap via different degree of intermolecular coupling after annealing, for the device under a given condition, V_{OC} should be constant. However, how to modify energy level of a given system and therefore V_{OC} remains challenging due to the difficulty in accessing to D/A interface in OSCs.

Well-defined bilayer structures could be suitable for the fundamental investigation of D/A interfaces in OSCs. However, the intermixing of D and A molecules at the interface must be avoided. The preparation of bilayer devices usually involves vacuum deposition or successive spin-coating of the organic materials. These methods often induce diffusion and intermixing of the D and A molecules at the interface.[1-3]

Recently, I have demonstrated that the insertion of aligned molecular dipole moments at the D/A interface of OSCs with a well-defined bilayer structure changed the energy level difference between the LUMO of acceptor and the HOMO of donor (E_{DA}), resulting in a large change in V_{OC} even for the same combination of the materials in the bulk films (Figure 2.1.1).[4] This clearly shows that the performance of OSCs could be strongly affected by the D/A interfacial properties. Furthermore, it is possible that these interfacial properties could be changed by external stimuli after the fabrication of the devices. This could clarify the relationship between the interfacial properties and the device performance, and also produce a new type of optoelectronic device that responds to various external stimuli.

In this chapter, I will present the manipulation of the molecular dipole moments in bilayer OSCs by electric fields. The structures of the materials in this work are shown in Figure 1.1.2. The same combination of materials as in our previous work was adopted: [6,6]-phenyl-C_{61}-butyric acid methyl ester (PCBM) as the acceptor; poly(3-hexylthiophene) (P3HT) as the donor; and surface-segregated monolayers (SSMs) of fluoroalkylated organic semiconductors, [6,6]-phenyl-C_{61}-butyric acid 1H,1H-perfluoro-1-nonyl ester (FC_8) or poly(4’-dodecyl-3-[1H,1H,2H,2H-perfluorooctyl]-2,2’-bithiophene)s (P3DDFT), as the dipole layer at the D/A interface. As previously reported, the aligned dipole moment of FC_8 reduced E_{DA} and thus V_{OC} of the OSC compared to the pristine P3HT/PCBM interface. When a negative bias was applied to the devices, the dipole moment of FC_8 became disordered or was reversed by to the electric field (Figure 2.1.2). This change in the dipole moment could induce a change in the energy alignment at the D/A interface, which should be reflected in the diode and OSC properties. More interestingly, these process could be totally reversible by using a positive bias, giving a new property of the device that V_{OC} could be controlled by electric field even after device fabrication.

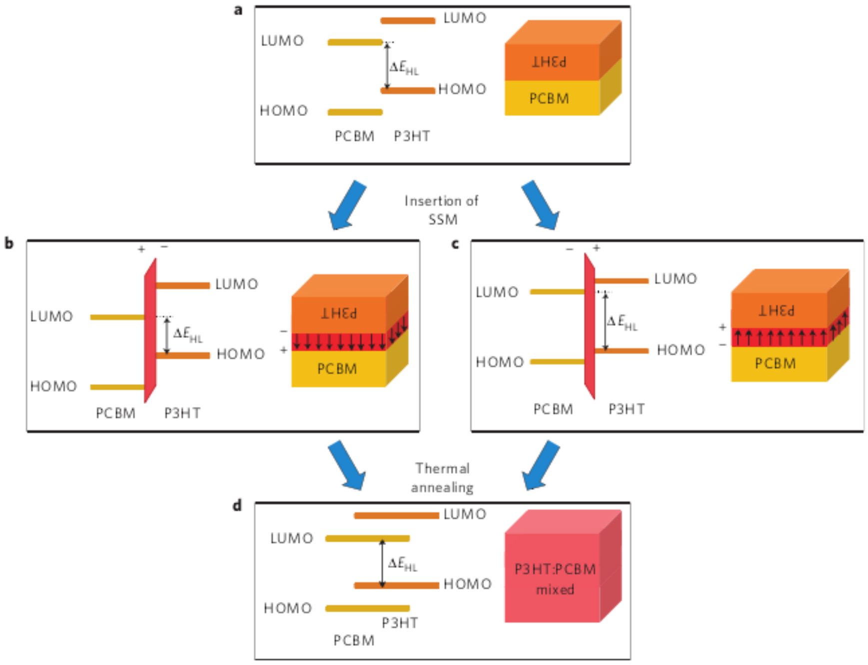

Figure 2.1.1 Schematic representation and energy diagrams of the P3HT/PCBM bilayer devices. a) Without interfacial dipole moments. b) With interfacial dipole moments of FC_8. c) With interfacial dipole moments of P3DDFT. d) After thermal annealing. Figure is reproduced from ref. 4 with permission. Copyright 2011. Nature materials.

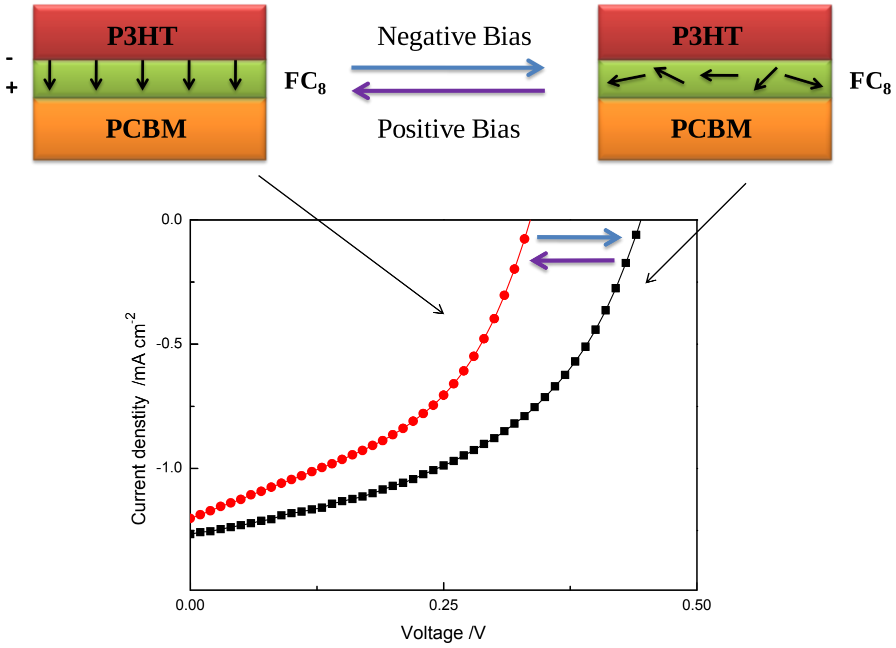

Figure 2.1.1 Schematic representations of the dipole moment reorientation induced by bias voltages in PCBM/FC$_8$//P3HT bilayer devices.

2.2 Experiments

Materials. [6,6]-phenyl-C$_{61}$-butyric acid methyl ester (PCBM) as the acceptor; poly(3-hexylthiophene) (P3HT) as the donor; and surface-segregated monolayers (SSMs) of fluoroalkylated organic semiconductors, [6,6]-phenyl-C$_{61}$-butyric acid 1H,1H-perfluoro-1-nonyl ester (FC$_8$) or poly(4'-dodecyl-3-[1H,1H,2H,2H-perfluorooctyl]-2,2'-bithiophene)s (P3DDFT), as the dipole layer at the D/A interface. Chemical structures of the above materials are shown in Figure 2.2.1 .

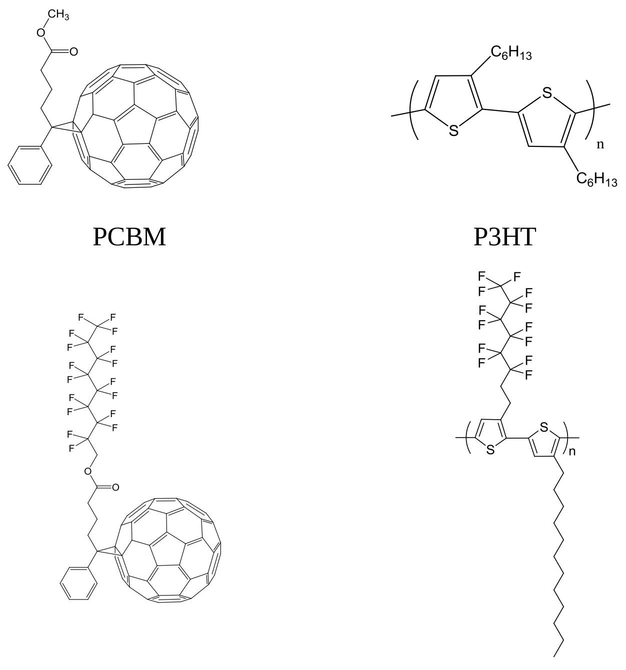

Figure 2.2.1 Chemical structures of PCBM, P3HT, FC_8, and P3DDFT.

Preparation of electron transporting layer TiO_2 films. ITO-coated glass substrates (sheet resistance $10\Omega^{-1}$, Geomatech) were cleaned by ultrasonication in detergent, water, acetone, 2-propanol and water again for 30 min, and were exposed to ultraviolet-ozone for 20 min. TiO_2 precursor solution (NDH-510C, Nippon Soda) diluted by ethanol was spin-coated on the ITO substrates at a spinning rate of 3,000 r.p.m. for 30 s followed by drying at 140 ℃ for 40 min and calcination at 500 ℃ for 30 min to form an electron-transporting layer. Then, the substrates were again cleaned by ultrasonication in acetone and 2-propanol.

Preparation of donor layer and acceptor layer. Chlorobenzene solution containing 10 mg/mL of PCBM was spin-coated onto the ITO/TiO_2 substrates at a spinning rate of 600 r.p.m. for 60 s. The substrates were thermally annealed at 150 ℃ for 5 min inside a N_2-filled glove box. The substrates with the structure glass/PSS (Aldrich)/P3HT were prepared by successive spin-coatings. PSS was a sacrificial layer and was prepared by spin-coating of aqueous solution containing 10 mg/mL of PSS at a spinning rate of 4,000 r.p.m. for 30 s on the glass substrates, which were precleaned and exposed to ultraviolet_ozone in the same way as were the ITO substrates. Chlorobenzene solution containing 10 mg/mL of P3HT was spin-coated on the glass/PSS substrates at a spinning rate of 1,000 r.p.m. for 60 s. ITO/TiO_2/PCBM/FC_8 film was fabricated from spin-coating chlorobenzene solution containing 10 mg/mL of PCBM and FC_8 (ratio 1:0.1). glass/PSS/P3HT/P3DDFT was fabricated from spin-coating chlorobenzene solution containing 10 mg/mL of P3HT and P3DDFT (ratio 1:0.1) at 120 ℃.

Device fabrication by contact film transfer (CFT). Contact film transfer method is previously reported by Wei et al.[5] The schematic image of CFT process is shown in Figure 2.2.2. Acceptor (PCBM) and SSM (FC_8) film was spin-coated on TiO_2 coated ITO. During spin-coating, FC_8 will flow to the surface due to its lower surface energy compared to PCBM, serving as dipole moment at the surface of film.(Figure 2.2.3) Donor (P3HT) film was spin-coated on PSS coated glass. Then the donor coated substrate was placed upside down onto acceptor coated substrate. One drop of water was placed on the edge of these two substrate. The water drop will selectively dissolve PSS layer because it's water soluble. After PSS layer was dissolved by water, donor film will be transferred onto the acceptor film . After evaporation of hole transporting layer V_2O_5 and electrode Al, the fabrication of bilayer OSCs were completed. Since in CFT method, no pressure or heat was involved, a clear laminated D/A interface could be expected. One more merit is that each layer could be modified purposely before film transfer, and these modification could remain at D/A interface after transfer, allowing us to investigate how D/A interfacial property affects device performance.

Device characterization. The bias was applied to the device as follows: the devices were placed on a hot plate at 55 ℃ in the dark, and the negative or positive bias voltage was applied for 50 min. After each bias was applied to the same device, the *J*-*V* characteristics of the OSCs were measured using a *J*-*V* measurement system (Model 2400, Keithley) either in the dark or under AM1.5 simulated solar light irradiation (PEC-L11, Peccell Technologies) at room temperature. This procedure was repeated with different bias voltages. A photomask was used to define an active area of 0.12 cm^2 for the devices. The light intensity was adjusted to 100 mW/cm^2 with a standard silicon solar cell (BS520, Bunkou Keiki, Japan).

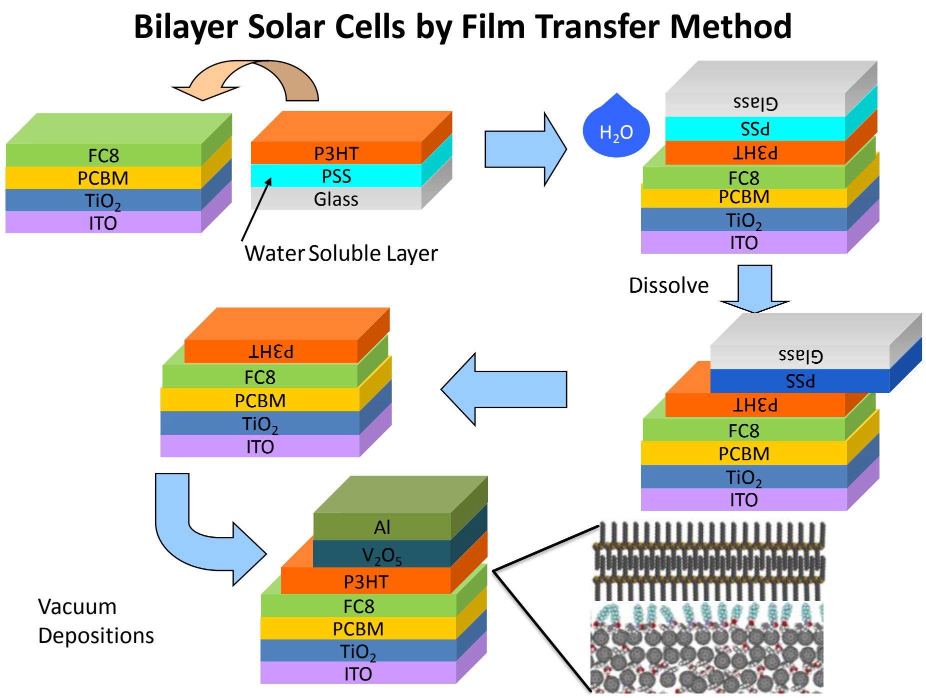

Figure 2.2.2 Schematic image of CFT method.

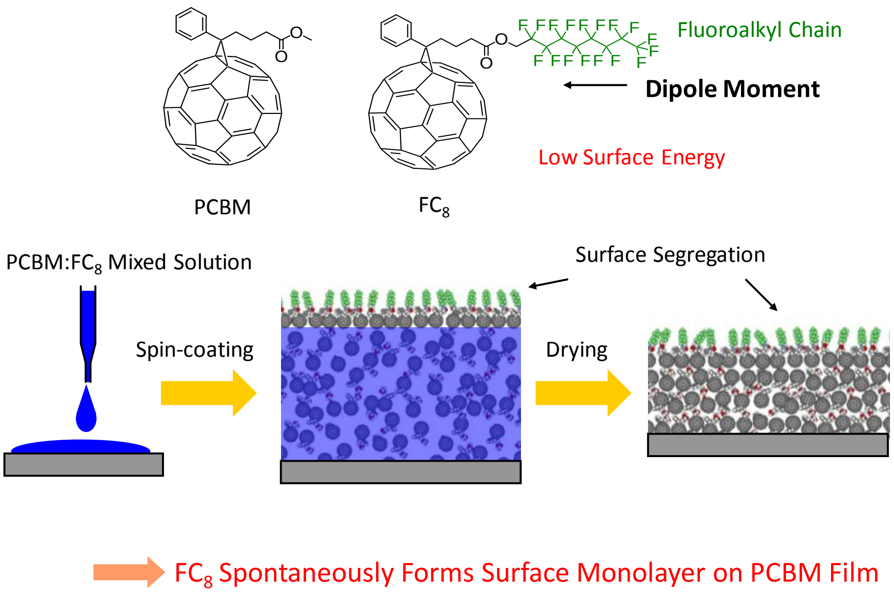

Figure 2.2.2 Modifying film surface with SSM.

2.3 Results and Discussions

Dipole switching by FC_8

In this research, dipole flipping at D/A interface was achieved by adding electric field. In order to enhance the response of molecules, the substrate was heated up to increase molecular dynamics. However, it is confirmed that interfacial mixing didn't happen under such conditions.

The *J*-*V* characteristics for the PCBM//P3HT and PCBM/FC_8//P3HT OSCs are shown in Figure 2.3.1. The PCBM//P3HT device had a V_{OC} of 0.49 V, J_{SC} of 1.46 mA cm^{-2}, and fill factor (FF) of 0.57. The PCBM/FC_8//P3HT device had a comparable J_{SC} of 1.40 mA cm^{-2}, and FF of 0.51, although the V_{OC} value of 0.34 V was lower. These results were consistent with our previous study.[4] The lower V_{OC} in the PCBM/FC_8//P3HT device can be attributed to the formation of dipole moment induced by the alignment of the fluoroalkyl chains of the FC_8 molecules during spin-coating the blended solution of PCBM and FC_8, and the relative energy levels were shifted between the P3HT and PCBM layer, resulting in a smaller E_{DA} (Figure 2.3.2).

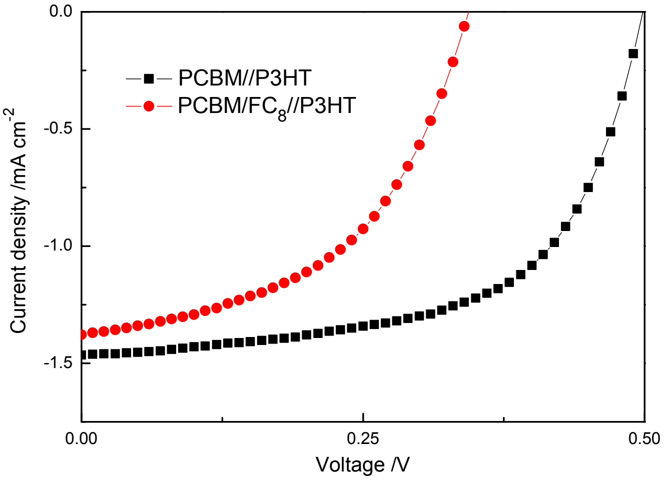

Figure 2.3.1. *J*-*V* characteristics of the PCBM//P3HT and PCBM/FC$_8$//P3HT devices under irradiation.

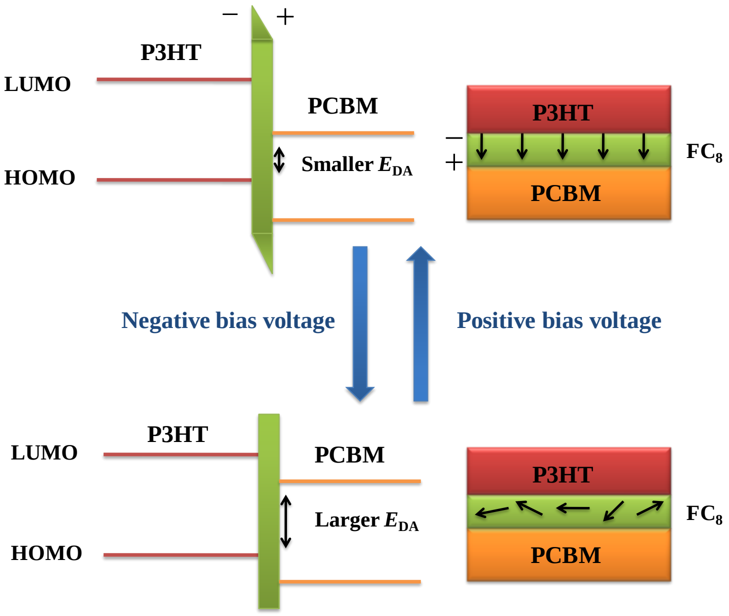

Figure 2.3.2 Schematic representations of the change in the energy diagrams and the dipole moment orientation induced by bias voltages in PCBM/FC$_8$//P3HT bilayer devices.

Figure 2.3.3 shows the dark *J*-*V* characteristics of the PCBM/FC$_8$//P3HT devices and the *J*-*V* characteristics under light irradiation after the application of a negative bias voltage of −5 to −8.5 V at 55 °C for 50 min. We confirmed that at temperatures below 60 ℃ with no applied bias there was no change in V_{OC} or J_{SC}, indicating that there was no intermixing of the materials at the interfaces (Figure 2.3.4). We also confirmed that the device temperature was always below 59 ℃ for all the bias application conditions (Figure 2.3.4). Therefore, I can exclude the possibility that the changes were caused by the mixing of the interfacial molecules; applying the bias at lower temperatures induced similar changes, although the response was slower (Figure 2.3.5). The dark *J*-*V* curves show that as the applied bias became more negative, the reverse saturation current density decreased and the turn-on voltage for the diode increased (indicated by the arrows in Figure 2.3.3a). Under irradiation, V_{OC} increased from 0.34 to 0.51 V as the negative bias voltage increased, whereas J_{SC} decreased from 1.40 to 1.15 mA cm^{-2}. When a larger negative bias voltage (−15 to −20 V) was applied to the device, V_{OC} of 0.63 V was observed (Figure 2.3.5). This value was higher than that of the PCBM//P3HT device (0.49 V), although it was smaller than the value I have previously reported with the opposite dipole moment (up to 0.95 V).[4] However, J_{SC} decreased sharply under higher negative biases and the devices broke down when the bias voltage was increased to −20 V.

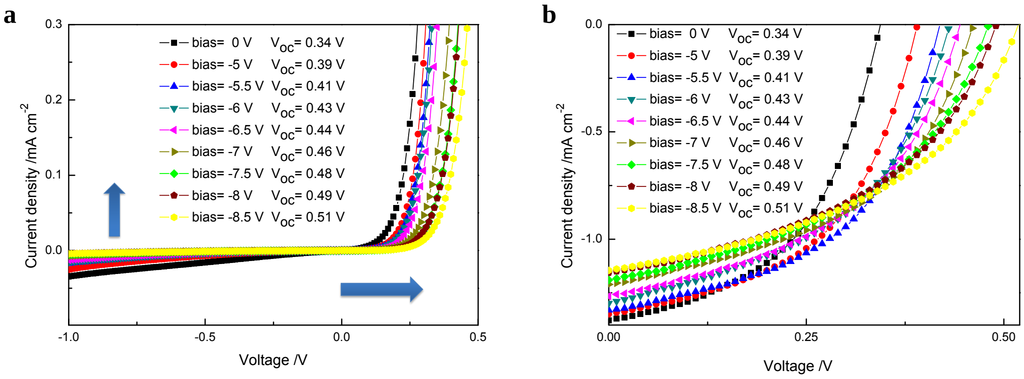

Figure 2.3.3. *J-V* characteristics of PCBM/FC_8//P3HT devices (a) in the dark, and (b) under irradiation after applying the designated negative bias voltages.

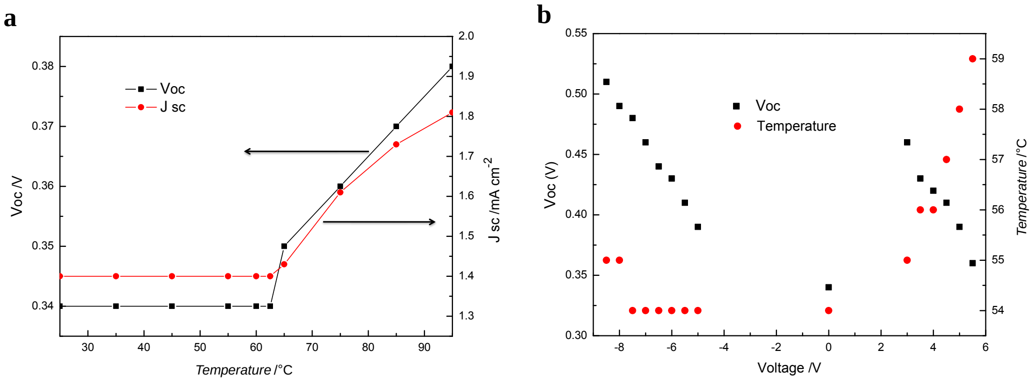

Figure 2.3.4. a) V_{OC} and J_{SC} versus temperature in PCBM/FC_8//P3HT devices. No change was observed up to 60 ℃, indicating that there was little intermixing of the materials at the interfaces below this temperature. b) Change in the surface temperatures of PCBM/FC_8//P3HT devices during the application of the bias voltage. Changes in V_{OC} after the bias voltage was applied are also shown. Temperatures did not exceed 60 ℃ for bias voltages in the range of −8.5 to +5.5 V.

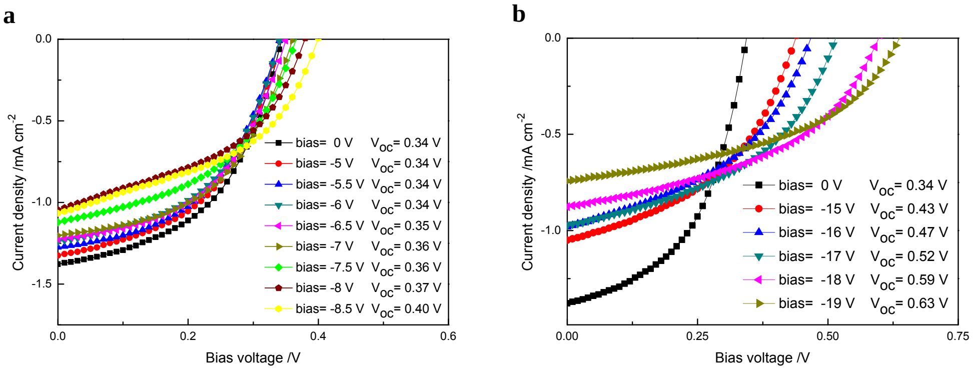

Figure 2.3.5. a) The *J*-*V* characteristics of PCBM/FC_8//P3HT devices under irradiation after applying the negative bias voltages (−5 to −8.5 V) at room temperature for 50 min. V_{OC} changed from 0.34 to 0.40 V, which was smaller than that at 55 ℃, which was from 0.34 to 0.51 V. b) The *J*-*V* characteristics of PCBM/FC_8//P3HT devices under irradiation after applying the negative bias voltages (−15 to −19 V) at 55 ℃ for 50 min. V_{OC} of 0.63 V was observed for high negative biases, although J_{SC} was dramatically reduced.

The performance of the PCBM//P3HT device after the bias voltages were applied was investigated as a control experiment. Figure 2.3.6 shows that the turn-on voltage of the diode in the positive voltage region (0 to +0.5 V) remained the same, and the reverse saturation current density remained largely unchanged after the negative bias voltages up to −8.5 V were applied. Under light irradiation, V_{OC} of the PCBM//P3HT devices did not change (0.49 to 0.52 V). J_{SC} decreased from 1.46 to 1.24 mA cm^{-2} after applying the bias voltages, which was similar to the decrease observed in the PCBM/FC_8//P3HT devices (1.40 to 1.15 mA cm^{-2}).

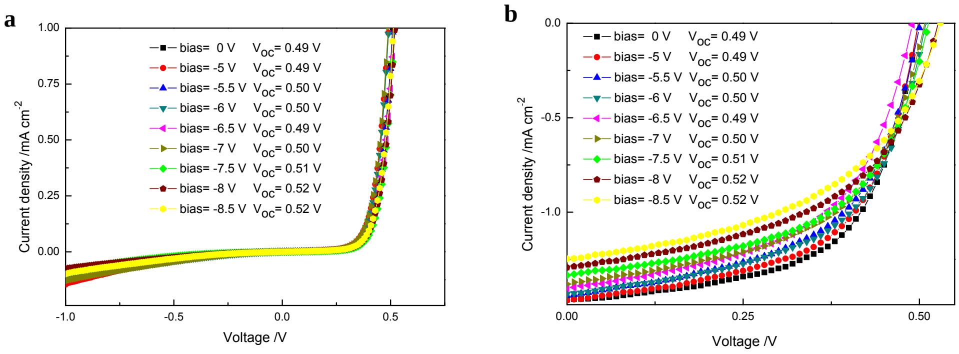

Figure 2.3.6. *J-V* characteristics of the PCBM//P3HT devices (a) in the dark, and (b) under irradiation after applying the negative bias voltages.

The changes in V_{OC} and diode behavior of PCBM/FC$_8$//P3HT device can be explained by the electric field causing changes in the orientation of the fluoroalkyl chains in FC$_8$. V_{OC} of the OSCs should represent the average properties of the D/A interface. V_{OC} of the PCBM/FC$_8$//P3HT device reached a similar value to that of the PCBM//P3HT device (0.51 V) after applying a negative bias (−8.5 V), which suggests that the fluoroalkyl chains lost their orientation. The E_{DA} shift disappeared because the direction of the dipole moment no longer pointed from the P3HT to PCBM layer, which was caused by the change in the alignment of the fluoroalkyl chains. When a larger negative bias of −19 V was applied, V_{OC} increased further to 0.63 V, indicating that the dipole moments of the fluoroalkyl chains began to be oriented in the opposite direction, from the PCBM to the P3HT layer.

The changes in the reverse saturation current and the turn-on voltage of the diodes could also be attributed to the change in E_{DA}. At thermal equilibrium, the reverse current should be proportional to the thermally generated charges at the D/A interface. Therefore, it should depend exponentially on E_{DA}, which represents the energy difference between the ground state and charge separated state, E_{CT}, assuming there is no charge injection from the electrodes. The dark *J*-*V* curves can be fitted with the standard Shockley equation by using one diode model in the range of −0.2 to +0.8 V.[6-7] The change in the turn-on voltage in the diodes can be reproduced by changing the reverse saturation current density (J_0), whereas the other parameters, such as R_{p}, R_{s}, or n, remained similar (Figure 2.2.7 and Table 2.3.1). This also suggests the observed changes were caused by the change in the energy levels at the D/A interface.

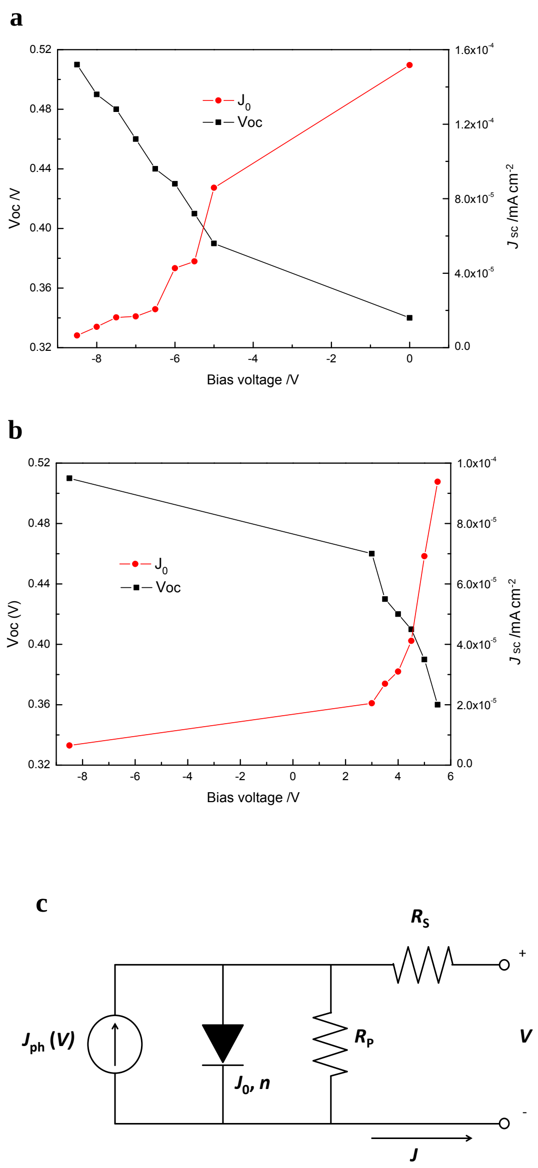

Figure 2.3.7 Plots of J_0 obtained by fitting the Shockley equation and V_{OC} measured after the bias voltage was applied to the PCBM/FC$_8$//P3HT device with a) negative, and b) positive biases. When the bias voltage became more negative, V_{OC} increased and J_0 decreased. The positive bias was then applied to the same device. When the bias voltage was positive, V_{OC} decreased and J_0 increased. c) Equivalent circuit model used for the *J*-*V* curve fitting.

Table 2.3.1. Summary of PCBM/FC8//P3HT device performance and the parameters extracted by analyzing the dark *J*-*V* characteristics using the Shockley equation ($J = \frac{1}{1+R_s/R_p}[J_0\{\exp(\frac{V-JR_sA}{nkT/e})-1\}+\frac{V}{R_pA}]-J_{ph}$). The optimum ideality factor *n* was 1.75 for all fittings.

Bias voltage	V_{OC} /V	Bias /V	J_0 /mA cm^{-2}	R_S /kΩ	R_P /kΩ
Negative bias	0.34	0	1.517×10^{-4}	1.5×10^{-1}	1.0×10^{4}
	0.39	−5	8.586×10^{-5}	1.8×10^{-1}	2.1×10^{4}
	0.41	−5.5	4.634×10^{-5}	1.7×10^{-1}	4.9×10^{4}
	0.43	−6	4.256×10^{-5}	4.6×10^{-1}	7.0×10^{4}
	0.44	−6.5	2.064×10^{-5}	1.7×10^{-1}	1.3×10^{5}
	0.46	−7	1.677×10^{-5}	2.0×10^{-1}	1.8×10^{5}
	0.48	−7.5	1.625×10^{-5}	2.3×10^{-1}	1.3×10^{5}
	0.49	−8	1.122×10^{-5}	2.7×10^{-1}	1.0×10^{5}
	0.51	−8.5	6.529×10^{-6}	2.8×10^{-1}	7.8×10^{4}
Positive bias	0.46	+3	2.047×10^{-5}	4.7×10^{-1}	2.0×10^{5}
	0.43	+3.5	2.694×10^{-5}	4.5×10^{-1}	9.7×10^{4}
	0.42	+4	3.115×10^{-5}	6.0×10^{-1}	8.1×10^{4}
	0.41	+4.5	4.117×10^{-5}	5.6×10^{-1}	9.3×10^{4}
	0.39	+5	6.917×10^{-5}	6.7×10^{-1}	7.3×10^{4}
	0.36	+5.5	9.382×10^{-5}	6.9×10^{-1}	5.9×10^{4}

J_{SC} decreased under the negative bias voltage. Because a similar decrease was observed in the PCBM//P3HT device control group, this may not be related only to the dipole change at the D/A interface, but also to the deteriorations of the electrodes or the charge transfer path in the active layer. We conducted the same experiments in vacuum, but the decrease of J_{SC} was still observed, which excluded the possibility that the degradation was due to the exposure to the air.

The PCBM/FC$_8$//P3HT device performance after applying the positive bias voltages was measured to determine whether the change of in V_{OC} is reversible. After V_{OC} of the PCBM/FC$_8$//P3HT device was increased from 0.34 to 0.51 V by applying a negative bias (−8.5 V), the positive bias voltages from +3 to +5.5 V were applied to the same device. The dark *J-V* characteristics shown in Figure 2.3.8 were the reverse of those caused by the negative bias: the reverse saturation current density was increased in the negative voltage region and the turn-on voltage was decreased (indicated by the arrows in Figure 2.2.7a). Under the light irradiation, V_{OC} gradually decreased when the positive bias voltages were applied and a V_{OC} of 0.36 V was obtained after a bias of +5.5 V was applied. This V_{OC} value was close to that of the original device before the biases were applied (0.34 V). A slight increase in J_{SC} from 1.06 to 1.13 mA cm^{-2} was observed when a positive bias of +5.5 V was applied. The current flow was larger for positive biases, because of the diode behavior of the bilayer OSCs; therefore the temperature approached 60 ℃ as the bias voltage increased in the positive direction. We suspect that the PCBM/P3HT interface began to mix at this stage, which resulted in a small increase in J_{SC}.

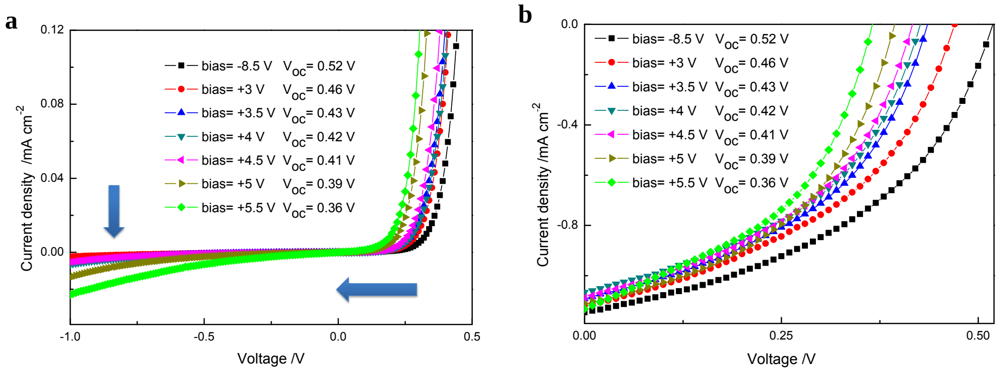

Figure 2.3.8. *J*-*V* characteristics of the PCBM/FC$_8$//P3HT devices (a) in the dark, and (b) under irradiation after the positive bias voltages were applied.

A negative (−7.5 V) and then a positive (+6 V) bias voltage were applied to the device for 50 min at 55 ℃ repeatedly, in order to demonstrate the reversible control of V_{OC} in the PCBM/FC$_8$//P3HT device Figure 2.3.9 shows V_{OC} of the PCBM/FC$_8$//P3HT device (black filled squares) switched reversibly between 0.32 and 0.44 V. In contrast, V_{OC} of the PCBM//P3HT device (red filled squares) remained nearly unchanged around 0.5 V. These results show that the change in V_{OC} was caused by the FC$_8$ layer at the D/A interface and was reversibly controlled by the bias directions.

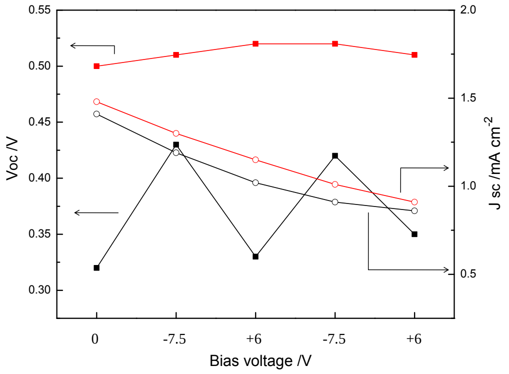

Figure 2.3.9 Changes in V_{OC} (filled squares) and J_{SC} (open circles) in the PCBM/FC$_8$//P3HT (black) and PCBM//P3HT devices (red) when alternating bias voltages of −7.5 and +6 V were applied at 55 ℃ for 50 min.

Dipole switching by P3DDFT

Similar changes of V_{OC} and the diode behaviors were also observed for PCBM//P3DDFT/P3HT devices: V_{OC} started from higher value of 0.88V as previously reported, because the original dipole direction in PCBM//P3DDFT/P3HT devices is opposite to that in PCBM/FC$_8$//P3HT devices.[4] After applying the designated positive bias voltages from +4 to +7 V at 55 ℃ for 20 min in the dark, the reverse saturation current density increased and the turn-on voltage for the diode decreased (indicated by the arrows in Figure 2.3.10a) as the applied bias became more positive. Under irradiation, V_{OC} decreased from 0.88 to 0.59 V and the decrease of J_{SC} was observed from 0.74 to 0.57 mA cm^{-2}. After these treatments, the designated negative bias voltages from −6 to −9 V were applied on the same device at 55 ℃ for 20 min in the dark. The reverse saturation current density decreased and the turn-on voltage for the diode increased (indicated by the arrows in Figure 2.2.10a) as the applied bias became more negative. Under irradiation, the V_{OC} increased from 0.59 to

0.84 V that is close to the original value, but further decrease of J_{SC} was observed from 0.57 to 0.42 mA cm^{-2}. In addition, similar switching experiments were conducted on PCBM//P3DDFT/P3HT devices with the alternating bias voltages of +7 and −10 V (Figure 2.3.11). Similar to PCBM/FC$_8$//P3HT device, V_{OC} switched reversibly between 0.66 and 0.82 V. In contrast, V_{OC} of the PCBM//P3HT device remained nearly unchanged around 0.5 V with the same treatments. These results indicate that the order of the dipole moments of the semifluoroalkyl side chains in P3DDFT also changed at the D/A interfaces by applying bias voltages.

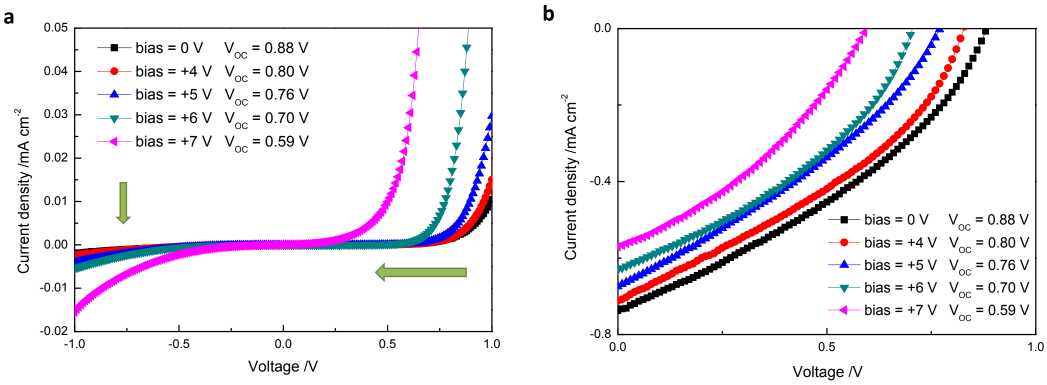

Figure 2.3.10 *J*-*V* characteristics of PCBM//P3DDFT/P3HT devices (a) in the dark, and (b) under irradiation after applying the designated positive bias voltages (from +4 to +7 V) at 55 ℃ for 20 min in the dark. The reverse saturation current density increased and the turn-on voltage for the diode decreased (indicated by the arrows in Figure 2.3.10a) as the applied bias became more positive (note that the original dipole direction of PCBM//P3DDFT/P3HT device is in the opposite direction compared to that of PCBM/FC$_8$//P3HT device). Under irradiation, the V_{OC} decreased from 0.88 V to 0.59 V; decrease of J_{SC} was also observed (from 0.74 to 0.57 mA cm^{-2}).

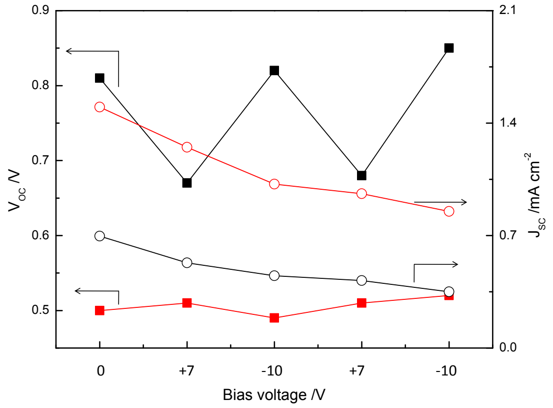

Figure 2.3.11. Changes in V_{OC} (filled squares) and J_{SC} (open circles) in the PCBM //P3DDFT/P3HT (black) and PCBM//P3HT devices (red) when alternating bias voltages of +7 and −10 V were applied at 55 ℃ for 20 min in the dark. The V_{OC} of PCBM //P3DDFT/P3HT device is (black filled squares) switched reversibly between 0.66 and 0.82 V. In contrast, V_{OC} of the PCBM//P3HT device (red filled squares) remained nearly unchanged around 0.5 V.

The change in the dipole moment was similar to the ferroelectric properties of fluoroalkyl compounds, such as poly(VDF-*co*-TrFE).[8] However, the change in the dipole moment was very slow in this study (50 min) compared with that of poly(VDF-*co*-TrFE). This could be because the dipole moment change in poly(VDF-*co*-TrFE) is caused by the twisting motion of the polymer main chain, whereas the changes in FC_8 and P3DDFT are caused by the movement of the entire fluoroalkyl chain. Therefore, the activation energy of the molecular reorientation should be much higher for FC_8 than poly(VDF-*co*-TrFE). At this stage, it is not clear whether the orientation was changed by just the fluoroalkyl chain or the entire molecules of FC_8 or P3DDFT. It is worth mentioning that after the changes of V_{OC} were induced, they were stable at least for three days. We speculate that the activation energies for the dipole moment change are relatively high because it is related to the change of the orientation of the molecules or the fluoroalkyl chains at the interfaces.

2.4 Conclusion

In conclusion, I have demonstrated that E_{DA} of donor and acceptor materials can be reversibly changed by D/A interfacial dipole reorientation, which changed the diode behaviors and V_{OC} of device. This methodology could be used in BHJ structures if well-defined large molecular interfaces and distinctly separated charge-transport paths could be formed in the films. The results obtained in this research may provide an experimental approach for investigating the correlation between OSC performance (V_{OC}) and D/A interfacial energy levels, and also produce a new type of optoelectronic device that responds to various external stimuli. Moreover, it demonstrate the availability of the methodology I used to construct clear donor/acceptor interface and introduce interfacial modification, correlating interfacial property with device performance. This method could be used as a prototype to investigate how interfacial property affect device performance in OSCs.

The text and the figures in this section contained the pre-peer reviewed version of the following article: Zhong Y.F.; Ma J.S.; Hashimoto K.; Tajima K.; Electric Field-Induced Dipole Switching at the Donor/Acceptor Interface in Organic Solar Cells, *Adv. Mater.* **2013**, 25, 1071-1075, which has been published in final form at [http://onlinelibrary.wiley.com/doi/10.1002/adma.201203605/abstract].

Reference

1. B. Yang, Y. Yuan, P. Sharma, S. Poddar, R. Korlacki, S. Ducharme, A. Gruverman, R. Saraf and J. Huang, Advanced Materials **24** (11), 1455-1460 (2012).
2. Z. T. Liu, M. F. Lo, H. B. Wang, T. W. Ng, V. A. L. Roy, C. S. Lee and S. T. Lee, Applied Physics Letters **95** (9), 093307 (2009).
3. C.-F. Shih, K.-T. Hung, H.-J. Chen, C.-Y. Hsiao, K.-T. Huang and S.-H. Chen, Applied Physics Letters **98** (11), 113307 (2011).
4. A. Tada, Y. Geng, Q. Wei, K. Hashimoto and K. Tajima, Nature Materials **10** (6), 450 (2011).
5. Q. Wei, K. Tajima and K. Hashimoto, ACS Applied Material Interfaces **1** (9), 1865 (2009).
6. J. William J. Potscavage, Asha Sharma, and Bernard Kippelen, Accounts for Chemical. Research **42** (11), 1758, (2009).
7. B. Rand, D. Burk and S. Forrest, Physical Review B **75** (11) (2007).
8. R. C. G. Naber, K. Asadi, P. W. M. Blom, D. M. de Leeuw and B. de Boer, Advanced Mater **22** (9), 933, (2010).

Chapter 3. Enhancement of V_{OC} without Loss of J_{SC} in Organic Solar Cells by Modification of Donor/Acceptor Interfaces

3.1 Introduction

Organic solar cells (OSCs) are promising candidates for generating cheap, clean electricity. However, their moderate power conversion efficiency (PCE) of up to 10% has limited their practical use.[1] Extensive research has been conducted to design low band gap polymers with suitable energy levels.[2-4] The short circuit current (J_{SC}) and the open circuit voltage (V_{OC}) of OSCs have been maximized by optimizing the energy level alignment and light absorption of the donor and acceptor materials. The band gap of the polymers should be related to the light absorption and thus to the maximum J_{SC} that can be achieved by the cells. The V_{OC} depends on the energy difference between the highest occupied molecular orbital (HOMO) of the donor and the lowest unoccupied molecular orbital (LUMO) of the acceptor (E_{DA}).[5, 6] Recently, this has been refined in accordance with the state picture by replacing E_{DA} with the energy of the charge transfer (CT) state, E_{CT}, which contains information on the structures at the donor/acceptor (D/A) interfaces and the relaxation of the charged molecular structures.[7, 8] The energy difference between the LUMOs of the donor and the acceptor serves as the main driving force for CT, and a LUMO offset is necessary to keep this process efficient. This can also be described using the state picture, by replacing the LUMO offsets with the energy difference between the photoexcited donor state (D*/A) and the CT state (D^+/A^-) (S_1-E_{CT}). Therefore, when the energy levels of the materials are manipulated, the compromise between E_{DA} and the LUMO offset leads to the trade-off between V_{OC} and J_{SC} in OSCs, which ultimately limits device performance.[9, 10]

In our previous work (chapter 2), I have developed experimental methods for fabricating bilayer OSCs with well-defined D/A interfaces. Introducing interfacial dipole moments at the D/A interface allows the relative energy levels of the materials to be tuned.[11, 12] The increase in E_{DA} resulting from the interfacial dipole moment improved V_{OC} from 0.5 to 0.9 V even for the same combination of materials. However, J_{SC} decreased, which may have been caused by the decreased LUMO offset. As a result, the increase in V_{OC} caused by the dipole moment did not increase the power conversion efficiency (PCE), which may indicate the limitations of energy level optimization.

The energy levels of the materials are one of several factors that determine the V_{OC}. E_{CT} is a more important parameter than E_{DA} and V_{OC} is the pseudo chemical potential difference between the electrodes in the steady state under photoirradiation. Therefore, when charge recombination competes with charge generation, the relative kinetics of these processes can change the charge density in the steady state and thus the chemical potentials. Consequently, the structure of the D/A interfaces, such as the distance and the molecular orientation of the donor and the acceptor, should substantially affect the V_{OC} even with the same E_{DA}. Thompson et al. investigated this aspect based on the electronic coupling at D/A interface by using a bilayer OSC and very recently the same system was revisited to correlate V_{OC} with E_{CT}.[13, 14] Although there have been several studies of the interfacial modification of OSCs with LiF, MoO_3, or a semiconducting polymer electrolyte,[15-17] no quantitative analysis of the effect of the interlayer on device performance has been published. The main challenge is to modify the interfaces to suppress charge recombination and simultaneously maintain efficient charge generation so as to increase the efficiency of device.

In this work, I purpose the concept of "ideal interface" in organic solar cells which has efficient charge separation, suppressed recombination and higher lying CT state (higher E_{CT}). As indicated in Figure 3.1.1, normal interface has charge separation and recombination happening at the same time. By taking D/A apart, the coupling between D and A became weakened, both charge separation and recombination were suppressed. Moreover, E_{CT} become larger due to weakened Coulomb interaction. The charge separation could be recovered while remaining suppressed charge recombination by introducing small amount of charge separation center. By using ideal interface, higher efficiency of device could be expected. Experimentally, the effect of D/A distance on device performance is investigated. A thin insulating transparent spacer layer was placed between the donor and acceptor layers in bilayer OSCs to change the D/A distance. Changes in V_{OC}, J_{SC}, and thermally generated current induced by the insulating layers in the dark were analyzed with an equivalent circuit model to reveal the physical processes at the interface. The changes may be related to E_{CT} and the electronic coupling between the excited and CT states, and between the CT and the ground state. The effect of doping the insulating layer with dye was also investigated to demonstrate that introducing efficient CT centers at the interfaces could recover the photocurrent and improve PCE.

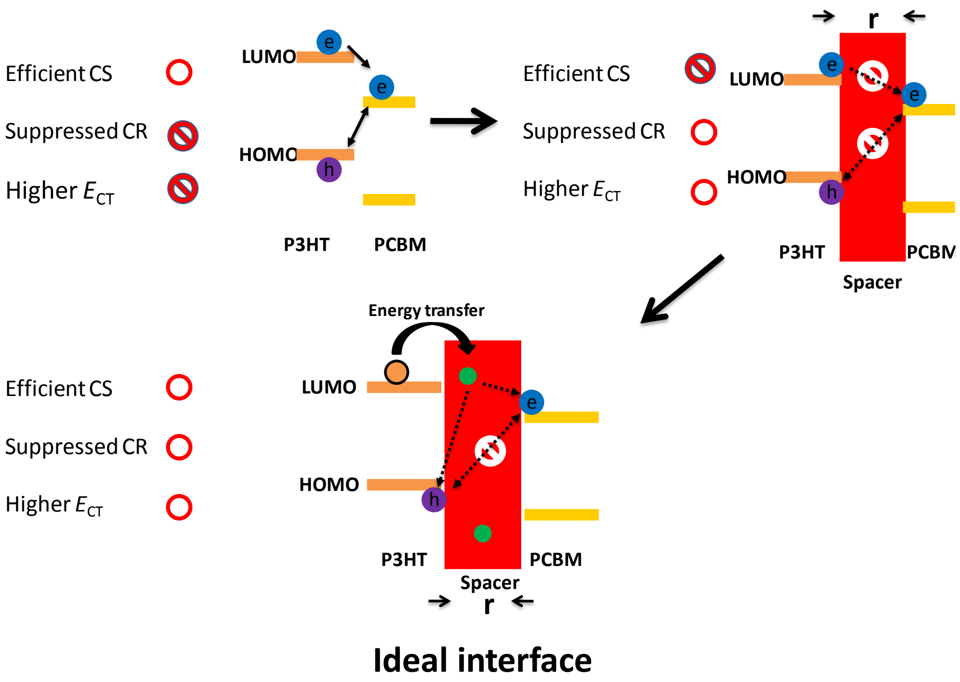

Figure 3.1.1 Schematic image of a) interface without modification, b) interface with enlarged D/A distance, c) interface with dye doping at D/A interface (ideal interface).

3.2 Experiments

Materials. The structures of the materials and their energy diagrams are shown in Figure 3.2.1. We chose [6,6]-phenyl-C_{61}-butyric acid methyl ester (PCBM) as the acceptor, poly(3-hexylthiophene) (P3HT) as the donor, and a fluorinated polymer

(CYTOP, Asahi Glass Co., Ltd.) as the insulating spacer. Because CYTOP is soluble in fluorinated solvents that are completely orthogonal to solvents suitable for the PCBM film, a thin CYTOP layer was spin-coated on the ITO/TiO_2/PCBM film without damaging the PCBM layer. We designed a silicon phthalocyanine dye molecule with axial semifluoroalkyl chains (F-SiPc), based on the SiPc dye synthesized by Ohkita et al.[18-20] SiPc has an intermediate HOMO-LUMO structure (Figure 1e) that enables the energy transfer from P3HT to SiPc. Ohkita et al. showed that the dye in the bulk heterojuction (BHJ) of P3HT:PCBM enhanced the photocurrent because of the absorption of SiPc and the energy transfer to the D/A interface. The fluoroalkyl chains make F-SiPc soluble in a fluorinated solvent, thus it is possible to dope the insulating layers with the dye at the PCMB/P3HT interface. Four devices, PCBM//P3HT, PCBM/CYTOP//P3HT, PCBM/CYTOP:F-SiPc//P3HT, and PCBM/F-SiPc//P3HT, were prepared, where // denotes an interface formed by the contact film transfer (CFT) method.[21, 22]

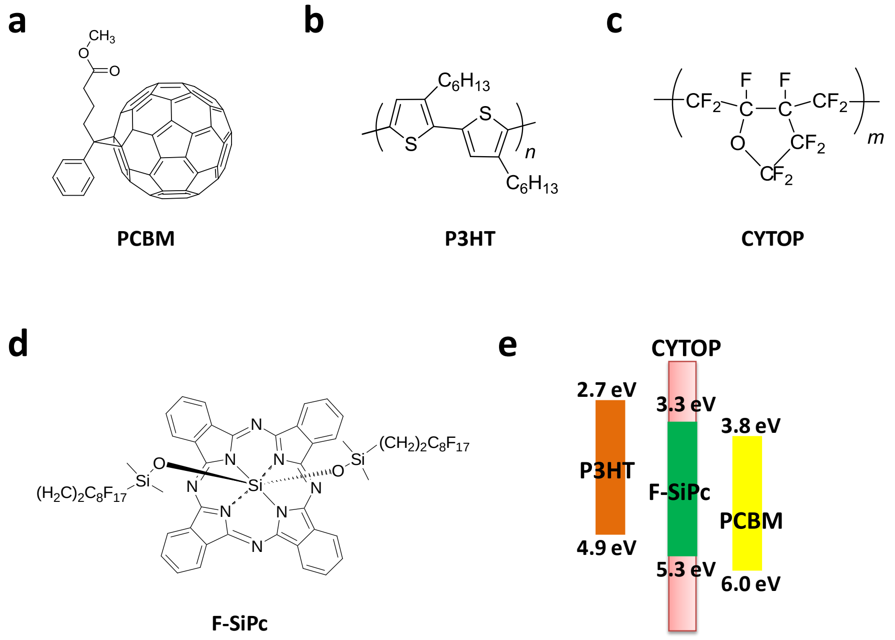

Figure 3.2.1 Chemical structures of the materials. a) PCBM, b) P3HT, c) CYTOP, and d) F-SiPc. e) Schematic energy diagram of the bilayer OSCs.

Device fabrication. The inverted bilayer device with a structure of ITO/TiO_2/PCBM (Frontier Carbon Corp., Japan)/CYTOP or CYTOP:F-SiPc/P3HT (Rieke Metals, USA)/V_2O_5/Al was fabricated as follows. ITO-coated glass substrates (sheet resistance: 10 Ω/□, Geomatech, Japan) were cleaned by successive ultrasonication in detergent, water, acetone, 2-propanol, and water for 30 min, and then were exposed to UV-ozone for 20 min. The ITO substrates were spin coated with an ethanol solution of the TiO_2 precursor (NDH-510C, Nippon Soda, Japan) at 3000 rpm for 30 s, dried at 140 ℃ for 40 min, and calcined at 500 ℃ for 30 min to form the electron-transporting layer (TiO_2 thickness: 25 nm). The substrates were cleaned by ultrasonication in acetone and 2-propanol. The ITO/TiO_2 substrate was spin coated with a 10 g L^{-1} chlorobenzene solution of PCBM at 600 rpm for 60 s. The substrates were thermally annealed at 150 ℃ for 5 min in a N_2-filled glove box. The ITO/TiO_2/PCBM substrates were spin coated with a CT-SOLV 180 (Asahi Glass Co., Ltd., Japan) solution of the spacer (CYTOP; CTL-809M, Asahi Glass Co., Ltd., Japan) at 3000 rpm for 60 s. The concentration of CYTOP was from 0.02 to 0.18% (v/v). The substrates were thermally annealed at 185 ℃ for 5 min on a hot plate in a N_2-filled glove box, in order to remove the CT-SOLV 180. The dye-doped CYTOP layer was prepared in the same manner. The F-SiPc dye was dissolved in the CYTOP solution at concentrations from 0.40 to 1.00 mg mL^{-1}. The CYTOP and F-SiPc solutions were heated at higher temperature (80 ℃ for 0.40 mg mL^{-1}, 100 ℃ for 0.75 mg mL^{-1}, and 120 ℃ for 1.00 mg mL^{-1}) to completely dissolve the F-SiPc. The dye-doped CYTOP solutions were spin coated onto the PCBM layer at 3000 rpm for 60 s. The substrates were also annealed at 185 ℃ for 5 min on a hot plate in a N_2-filled glove box to remove the solvent. Substrates with a structure of glass/poly(*p*-styrene sulfonate) (PSS; Aldrich)/P3HT were prepared by successive spin coating. The glass substrates for the sacrificial PSS layer were pre-cleaned and exposed to UV-ozone using the same method as for the ITO substrates, and then spin coated with a 10 g L^{-1} aqueous solution of PSS at 4000 rpm for 30 s. The glass/PSS substrates were spin coated with a 10 g L^{-1} chlorobenzene solution of P3HT at 1000 rpm for 60 s. The glass/PSS/P3HT substrate was gently placed upside down on the ITO/TiO_2/PCBM substrate (ITO/TiO_2/PCBM/CYTOP or ITO/TiO_2/PCBM/CYTOP:SiPc), and one drop of water was placed on the edge of two substrates. The water selectively penetrated and dissolved the PSS layer, resulting in the transfer of the P3HT layer onto the PCBM layer (PCBM/CYTOP or PCBM/CYTOP:SiPc). A V_2O_5 hole transport layer (4 nm) and Al electrodes (50 nm) were deposited by thermal evaporation under high vacuum (~10^{-4} Pa) in a vacuum evaporation system (H-2807, E-100 load lock, ALS Technology, Japan).

Device characterization. The *J-V* characteristics of the OSC devices were measured using a *J-V* measurement system (2400, Keithley. U.S) under AM1.5 simulated solar light irradiation (PEC-L11, Peccell Technologies, Inc., Japan). The active area of the devices was defined by a photomask as 0.12 cm^2. The light intensity was adjusted to 100 mW cm^{-2} by a standard silicon solar cell (BS520, Bunkou Keiki, Japan). The EQE of the devices was measured with a Hypermonolight System (SM-250 F, Bunkou-Keiki). The temperature dependence of the dark *J-V* characteristics was measured under high vacuum (<10^{-4} Pa) using a *J-V* measurement system (6430, Keithley). The temperature was controlled using a temperature controller (MJ-250, Measure Jig). XPS and UPS were performed on an AXIS Ultra DLD spectrometer (Kratos Analytical Ltd.). XPS spectra were obtained by using Al Kα radiation. UPS spectra were obtained with a He (I) excitation of 21.2 eV and a pass energy of 5 eV. UV-vis spectra were recorded on a JASCO V-650 spectrophotometer (Shimadzu, Japan).

3.3 Results and Discussions

Enhancement of V_{OC} without loss of J_{SC}

Figure 3.3.1 shows the structures of the devices. Figure 3.3.2 shows the results for the bilayer devices evaluated under AM1.5 simulated solar light (100 mW cm^{-2}). The PCBM//P3HT device had a V_{OC} of 0.49 V, a J_{SC} of 1.50 mA cm^{-2}, and a fill factor (FF) of 0.54, resulting in a PCE of 0.397%. These parameters were consistent with our previous results.[11] When a 0.95-nm-thick CYTOP layer was present in the PCBM/CYTOP//P3HT device, the V_{OC} increased to 0.60 V although the J_{SC} decreased to 0.81 mA cm^{-2}, which reduced the PCE to 0.309%. When I inserted the 0.95-nm-thick dye-doped CYTOP layer into the PCBM/CYTOP:F-SiPc//P3HT device, the V_{OC} increased to 0.60 V, which was similar to that of the PCBM/CYTOP//P3HT device. However, a J_{SC} of 1.40 mA cm^{-2} was obtained, which was comparable to that of the PCBM//P3HT device. This resulted in a PCE of 0.531% for the PCBM/CYTOP:F-SiPc//P3HT device, which was higher than that of the devices without the interfacial modification. A PCBM/F-SiPc//P3HT device was fabricated as a control, where only F-SiPc was spin-coated on the PCBM layer. The J_{SC} increased to 1.86 mA cm^{-2}, although the V_{OC} remained at 0.51 V, which is consistent with the results reported by Ohkita et al. for bulk heterojunction OSCs doped with SiPc. Our results clearly demonstrate that modifying the interface between the donor and the acceptor with a thin insulating layer doped with dye can achieve a high V_{OC} without reducing J_{SC}.

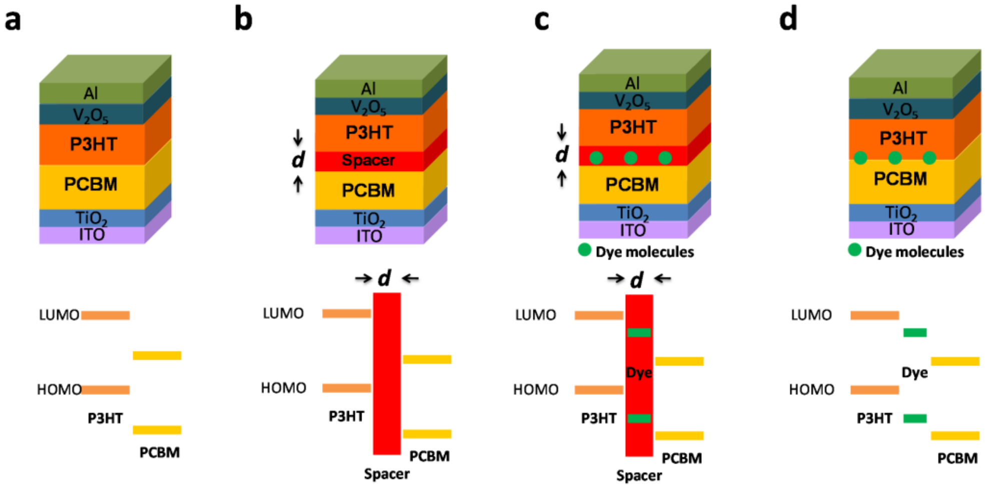

Figure 3.3.1 Schematic representation of bilayer OSCs. a) Without the spacer layer (PCBM//P3HT), b) with the spacer layer (PCBM/CYTOP//P3HT), c) with the spacer layer doped with the fluoroalkylated dye (PCBM/CYTOP:F-SiPc//P3HT), and d) with the fluoroalkylated dye (PCBM/ F-SiPc//P3HT).

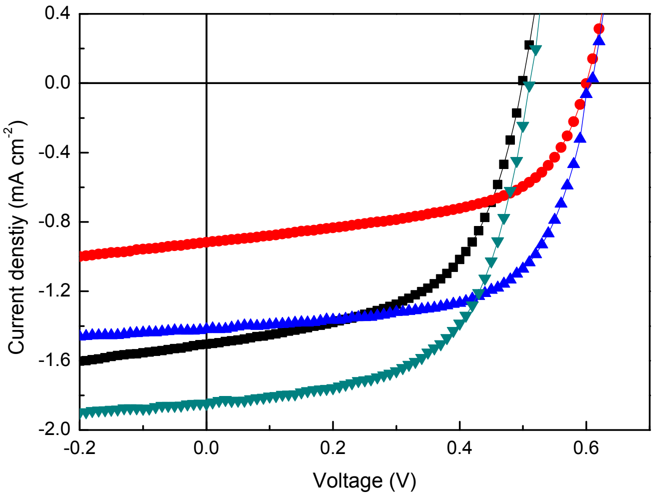

Figure 3.3.2. *J-V* curves of the four OSCs. PCBM//P3HT (■), PCBM/CYTOP//P3HT (●), PCBM/CYTOP:F-SiPc//P3HT (▲), and PCBM/F-SiPc//P3HT (▼).

Effect of the insulating layer thickness

The thickness of the CYTOP layer was changed to examine its effect on the OSC performance. Angle-dependent X-ray photoelectron spectroscopy (ADXPS) was used to determine the thickness of the CYTOP layers, which was varied in the range of 0.69-2.78 nm by changing the concentration of the solution. The data obtained by ADXPS can be well fitted with a simple bilayer mode to calculate the thickness of CYTOP, suggesting there is little intermixing of CYTOP and PCBM (see Figure 3.3.3). Furthermore, the contact film transfer method involves no heat, pressure or organic solvent, and the previous study showed that the surface structures are well preserved in the interface;[21, 22] therefore, this technique is well suited to correlate the interfacial structure and the device properties. The surface roughness of the PCBM/CYTOP film was also analyzed by AFM measurements (see Figure 3.3.4). The arithmetic mean roughness (R_a) was in the range of 0.31-0.78 nm, indicating that the presence of the CYTOP layer did not change the surface and interfacial roughness (R_a of the pristine PCBM film was 0.43 nm).

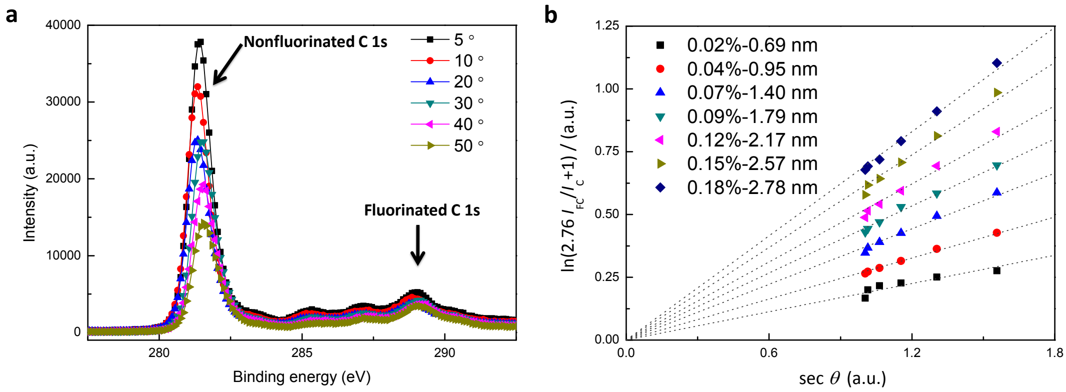

Figure 3.3.3 XPS measurement. a) ADXPS measurements for the ITO/PCBM/CYTOP film prepared from a 0.04% CYTOP solution. b) Plots of ln(2.76 I_{FC}/I_C+1) as a function of secθ at different concentrations of CYTOP. Linear fittings and the calculated thickness are also presented.

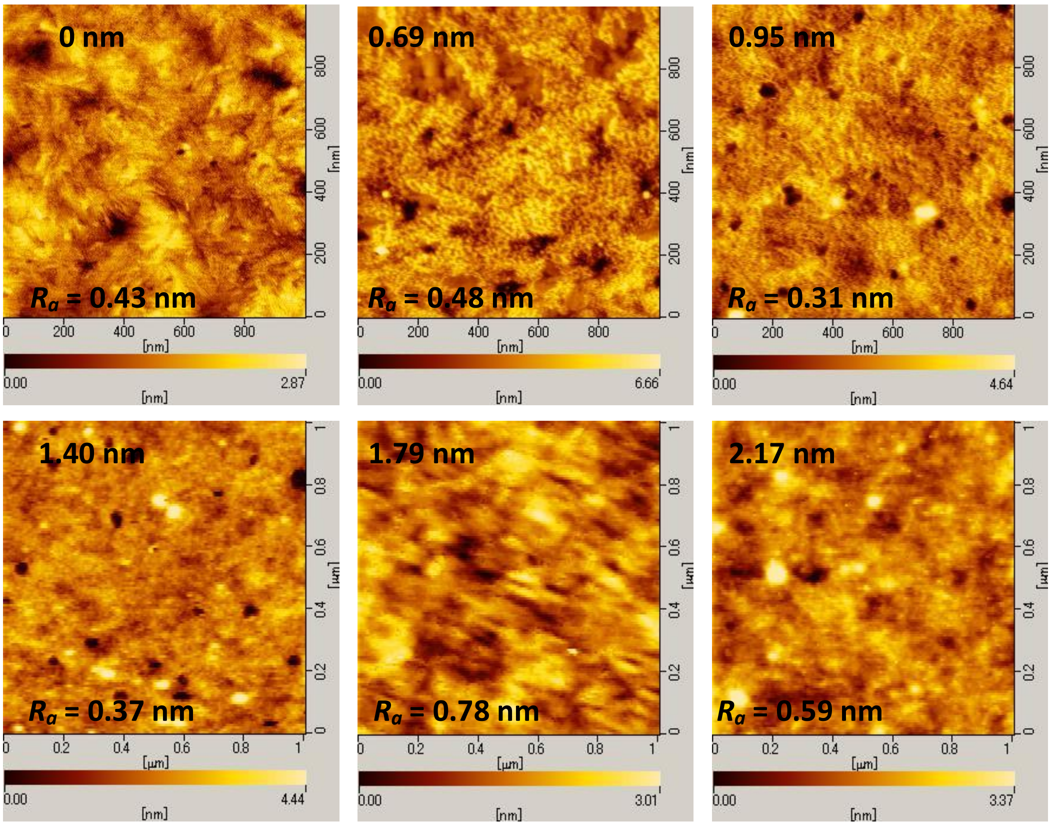

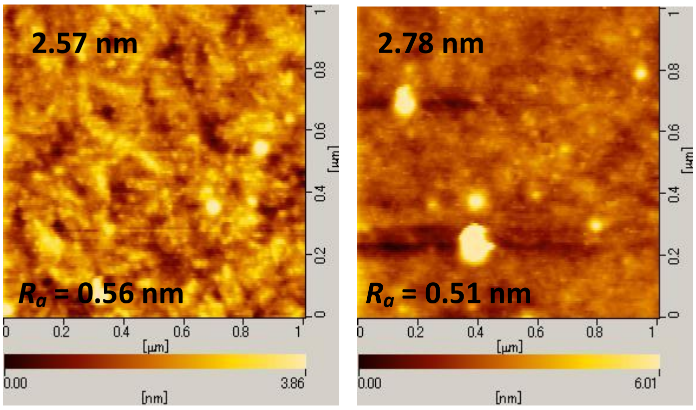

Figure 3.3.4 AFM images of PCBM/CYTOP films with different CYTOP layer thicknesses. The arithmetic mean roughness (R_{a}) is also shown.

To exclude the possibility that an interfacial dipole moment affected the OSC performance, I measured the ionization energy (IE) for PCBM and PCBM/CYTOP films by UV photoelectron spectroscopy (UPS). The PCBM/CYTOP films exhibited ionization energy (IE) of 5.63-5.72 eV that was similar to that of PCBM film (5.65 eV) and there was no clear relationship between the IE and the thickness (see Figure 3.3.5, Table 3.3.1). This result suggests the absence of an aligned dipole moment in the CYTOP layers. Because the CYTOP layer is introduced at the organic/organic interface in the bilayer device and the magnitude of the energy level shifts at the organic interface will be reduced from those in vacuum due to the dielectric constant of the materials (about 3-4), the effect of this energy level shift on the V_{OC} should be reduced by 1/3 to 1/4. In contrast, in fluoroalkyl self-segregated monolayers, IE shifts of up to +1.8 eV have been observed, depending on the density of the fluoroalkyl chains.[11, 23] This difference may be because CYTOP is an amorphous polymer and has no functional group with a lower surface energy that could segregate to the surface.

Even if there were a preferred molecular orientation on the surface, the molecular dipole moments from the main-chain fluorinated structure would be small.

Table 3.3.1 Ionization energies calculated from UPS measurements.

CYTOP Thickness (nm)	*Dye concentration* (mg mL^{-1})	*Ionization energy* (eV)
0	-	5.65
0.69	-	5.71
0.95	-	5.67
0.95	0.40	5.72
0.95	0.75	5.70
0.95	1.00	5.61
1.40	-	5.66
1.79	-	5.62
2.17	-	5.72
2.57	-	5.68
2.78	-	5.72

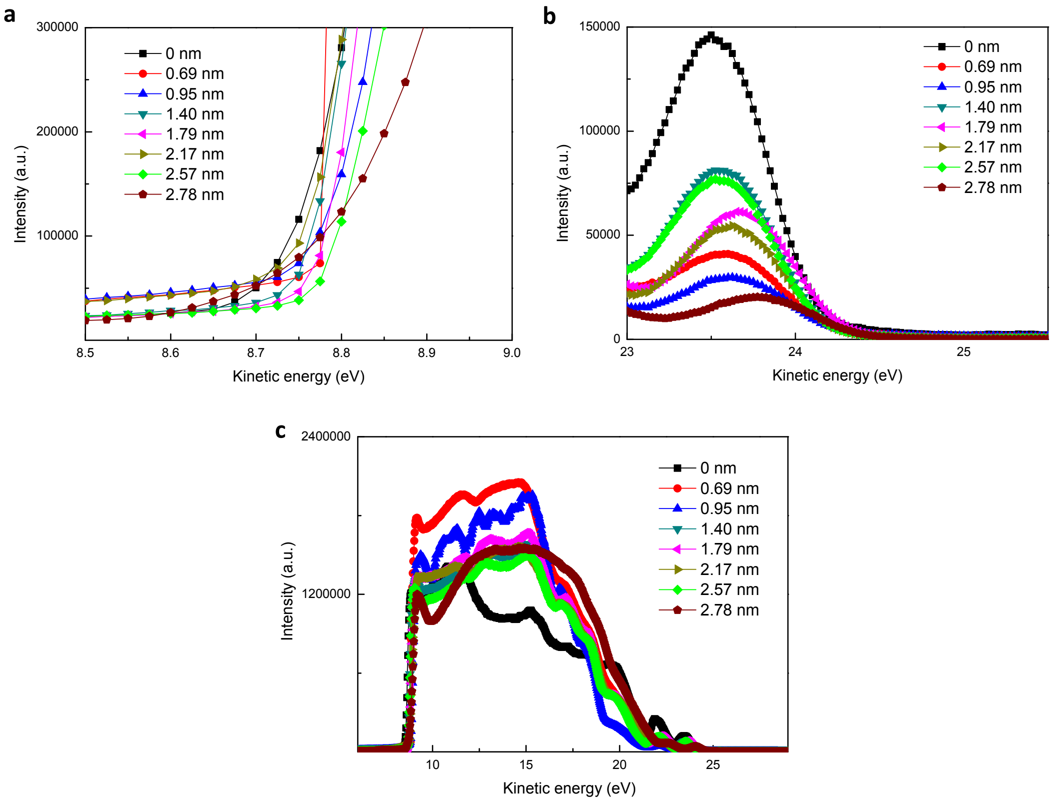

Figure 3.3.5 UPS measurement. a) Cutoff and b) Fermi-edge regions, and c) the whole range of the UPS spectra of the ITO/PCBM/CYTOP films with different CYTOP layer thicknesses.

The CYTOP layer is transparent in the visible region and thin enough (< 3 nm) to disregard the interference effect. The transmittance absorption spectra of the PCBM/CYTOP//P3HT films did not change when the CYTOP layers of various thicknesses were inserted (see Figure 3.3.6), which excludes the possibility of a change in the light absorption. Furthermore, the bilayer devices of PCBM/CYTOP or CYTOP/P3HT exhibited no photovoltaic behavior, indicating that the charge separation occurs exclusively at the PCBM/P3HT interface.

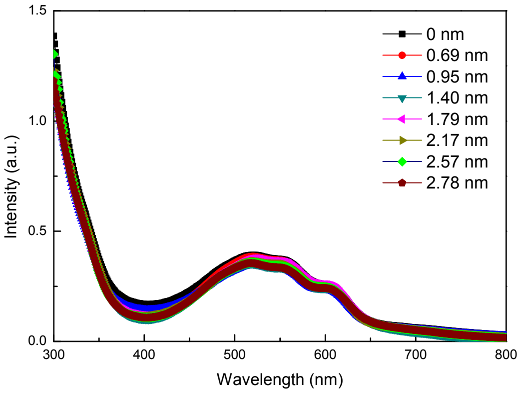

Figure 3.3.6. Absorption spectra of the TiO_2/PCBM/CYTOP//P3HT films.

The photovoltaic performance of PCBM/CYTOP//P3HT devices with CYTOP layers of various thicknesses are summarized in Figure 3.3.7. The V_{OC} increased from 0.49 V for the device with no CYTOP layer to 0.60 V for the 0.95-nm-thick layer, it remained constant until the thickness reached 2.17 nm, and then began to decrease. In contrast, J_{SC} monotonically decreased as the thickness of the spacer layer increased. The external quantum efficiency (EQE) spectra exhibited a monotonic decrease in the efficiency of the PCBM (300-400 nm) and P3HT (400-650 nm) response as the spacer thickness increased (see Figure 3.3.7c). This change corresponded well with the change in J_{SC}. The FF increased initially and decreased for CYTOP layers thicker than 1 nm. In summary, although the V_{OC} was increased by the insertion of the CYTOP layer, the substantial decrease in J_{SC} decreased the efficiency of the devices.

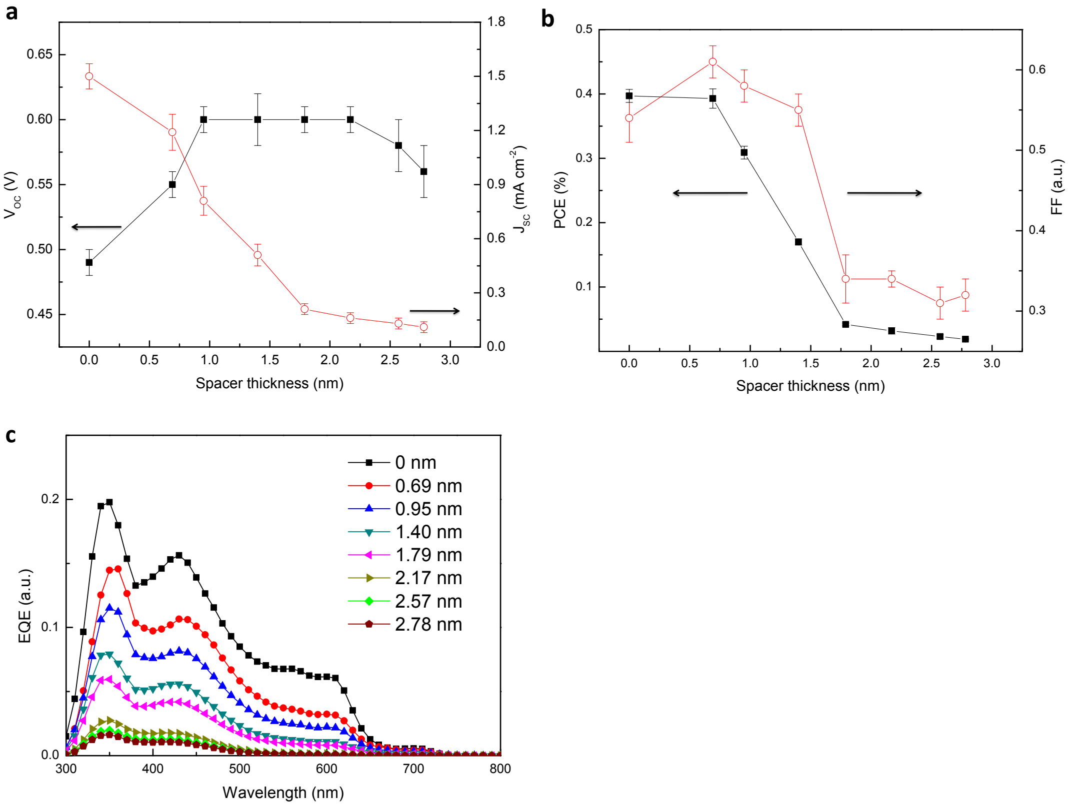

Figure 3.3.7 Dependence of the PCBM/CYTOP//P3HT device parameters on the thickness of the CYTOP layer. a) V_{OC} and J_{SC} and b) FF and PCE, c) EQE spectra of the PCBM/CYTOP//P3HT devices with different CYTOP layer thicknesses.

The dark *J–V* characteristics show that as the spacer became thicker, the reverse saturation current density decreased, and the turn-on voltage for the diode increased (see Figure 3.3.8). To analyze the change in the V_{OC} quantitatively, an equivalent circuit model was used to fit the dark *J-V* curves, according to a previously reported method.[6, 24] V_{OC} can be expressed by the Shockley equation, assuming the ideal case (see Supplementary Information for details)

$$V_{OC} \approx \frac{nkT}{e} \ln\left(\frac{J_{ph}(V_{OC})}{J_0}\right) \qquad (1)$$

where n is the ideality factor, k is the Boltzmann constant, T is the temperature, e is the elementary charge, $J_{\mathrm{ph}}(V_{\mathrm{OC}})$ is the photogeneration rate of the charge density under open circuit conditions, and J_0 is the reverse saturation current density. J_0 displays an empirical dependence on the temperature

$$J_0 = J_{00} \exp\left(-\frac{\phi}{kT}\right) \tag{2}$$

where J_{00} is the pre-exponential factor, and ϕ is the energetic term for the thermal excitation generation of the charge carrier under dark conditions. The combination of the two equations produces the following expression,

$$V_{\mathrm{OC}} \approx \frac{n\phi}{e} - \frac{nkT}{e} \ln\left(\frac{J_{00}}{J_{\mathrm{ph}}\left(V_{\mathrm{OC}}\right)}\right) \tag{3}$$

Vandewal et al. described the relationship between V_{OC} and E_{CT} obtained by spectroscopic methods and showed experimentally that V_{OC} converges to E_{CT}/e at 0 K.[25] When this relationship was compared with equation (3) for T, the expression $n\phi = E_{\mathrm{CT}}$ was obtained. This relationship is plausible if under the assumption that J_0 is proportional to the number of the charges thermally generated from the D/A interface in the steady state under negative bias. n can be interpreted as the average number of charges, which is between 2 (no charge trapping) and 1 (one of the charges trapped at the interface).[26] J_{00} may represent the density of the charge generation sites and the probability of charge generation, which would be directly related to the distance between the donor and acceptor.[27]

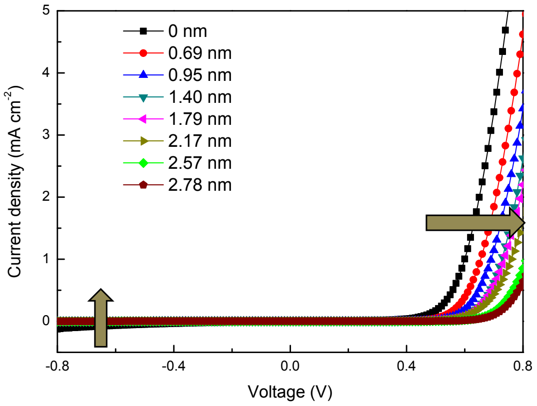

Figure 3.3.8 Dark *J–V* characteristics of PCBM/CYTOP//P3HT devices for different CYTOP layer thicknesses. The thickness of the spacer increased, the reverse saturation current density decreased, and the turn-on voltage for the diode increased, as indicated by the arrows.

Temperature-dependent measurements of the *J-V* curve were obtained and the dependence of the parameters J_{00}, J_{ph} (V_{OC}), $-nkT\ln(J_{00}/J_{ph}(V_{OC})$, and $n\phi$ extracted from the fitting of the thickness of the CYTOP layers are shown in Figure 3.3.9. Both J_{00} and J_{ph} monotonically decreased as the thickness of the spacer layer increased. The insulating spacer layer affected several processes at the D/A interface; the enlarged D/A distance may weaken the electron coupling between the excited (D^*/A or D/A^*) and CT states (D^+/A^-). It could also weaken the coupling between the CT and ground states; therefore, both the charge recombination and the charge separation were suppressed by the spacer layer at the D/A interface, resulting in the decrease of J_{00} and J_{ph}. The dependence on the thickness was larger for J_{ph} than in J_{00}, leading to the increase of $-nkT\ln(J_{00}/J_{ph}(V_{OC})$ (Figure 3.3.9c). However, $n\phi$ initially increased with the spacer thickness and then remained constant for thicknesses greater than 1 nm (Figure 3.3.9d). Because $n\phi = E_{CT}$ and n was not affected by the thickness of the

CYTOP layer in the curve fitting (n ~ 1.60), E_{CT} was increased by adding the spacer layer. E_{CT} can be expressed approximately by

$$E_{CT} = E_{DA} - \frac{e^2}{4\pi\varepsilon_0\varepsilon_r d} \tag{4}$$

where ε_0 is the vacuum dielectric constant, ε_r is the relative dielectric constant, and d is the D/A distance. The increase in E_{CT} was attributed to the increase in d, although the lower dielectric constant of CYTOP (2.0-2.1) could also reduce E_{CT}. E_{CT} converged to 1.1 eV, which is comparable to E_{DA} calculated from the HOMO of P3HT and the LUMO of PCBM measured by CV (1.0-1.1 eV).[28-30]

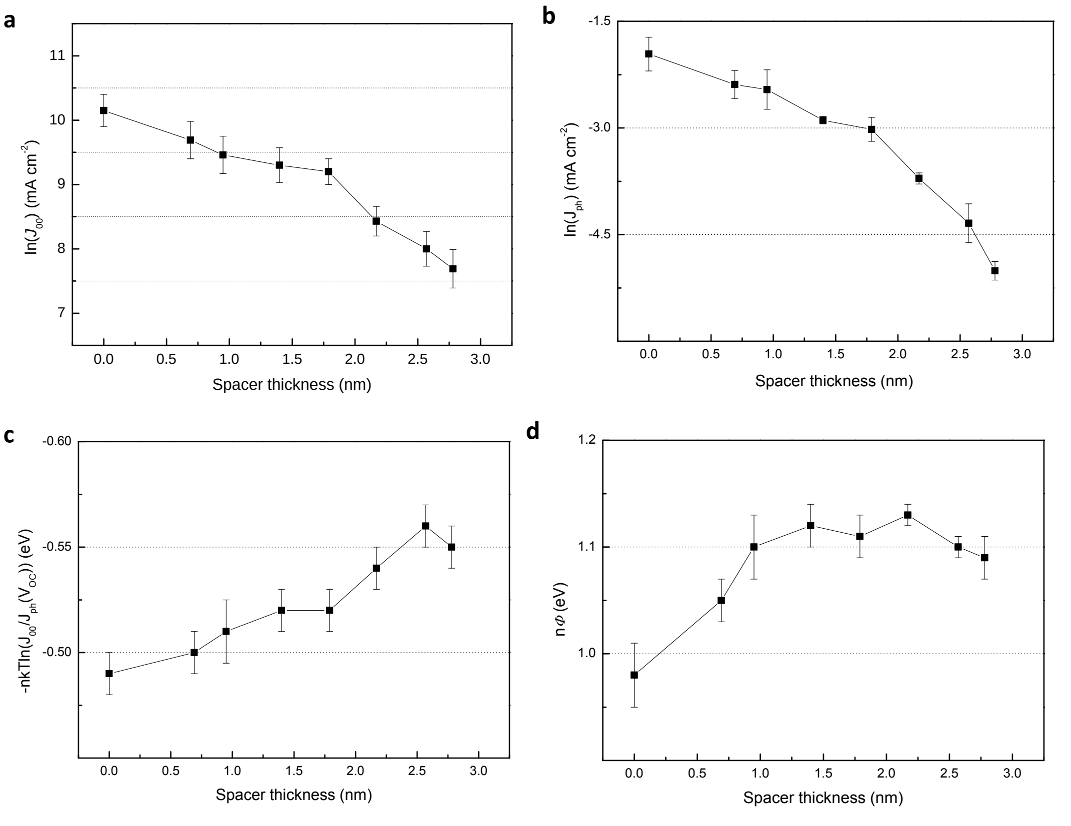

Figure 3.3.9 Parameters obtained from variable temperature dark *J-V* curve measurements on PCBM/CYTOP//P3HT devices. The dependence of a) J_{00}, b) J_{ph} (V_{OC}), c) $-nkT\ln(J_{00}/J_{\mathrm{ph}}(V_{\mathrm{OC}})$, and d) $n\phi$ on the thickness of the CYTOP layers.

These results show that two factors affect V_{OC}. The first is the larger dependence of J_{ph} on the spacer thickness compared with J_{00}, leading to an increase in the loss term, $-nkT\ln(J_{00}/J_{ph}(V_{OC})$. The second is the increase in E_{CT} caused by the reduced Coulomb interaction of the charges in the CT state. These two factors compete with each other, resulting in the V_{OC} dependence on the spacer thickness, indicated by the peak observed in Figure 3.3.8a.

Effects of dye doping concentration

The thickness of the CYTOP layer was fixed at 0.95 nm, and it was doped with different concentrations of F-SiPc dye. To dissolve the dye completely, the CYTOP solution was heated. The surface roughness of the films was not substantially altered by the addition of the dye and the aggregation of the dye was not observed (R_a = 0.39–0.47 nm, see Figure 3.3.10). The absorption spectra of ITO/TiO_2/PCBM/CYTOP:F-SiPc//P3HT films show that the absorption at 680 nm increased with the doping concentration (Figure 3.3.11a). The UPS spectra showed that the IE of the ITO/TiO_2/PCBM/CYTOP:F-SiPc films did not change with the doping concentration (see Figure 3.3.12, Table 3.3.1), indicating the effect of the molecular dipole moments was negligible.

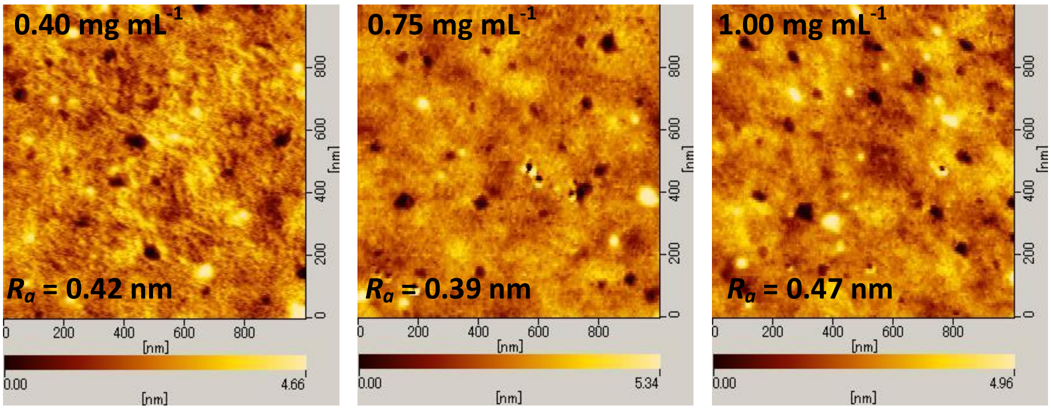

Figure 3.3.10. AFM images of PCBM/CYTOP:F-SiPc. The thickness of the CYTOP layer was 0.95 nm.

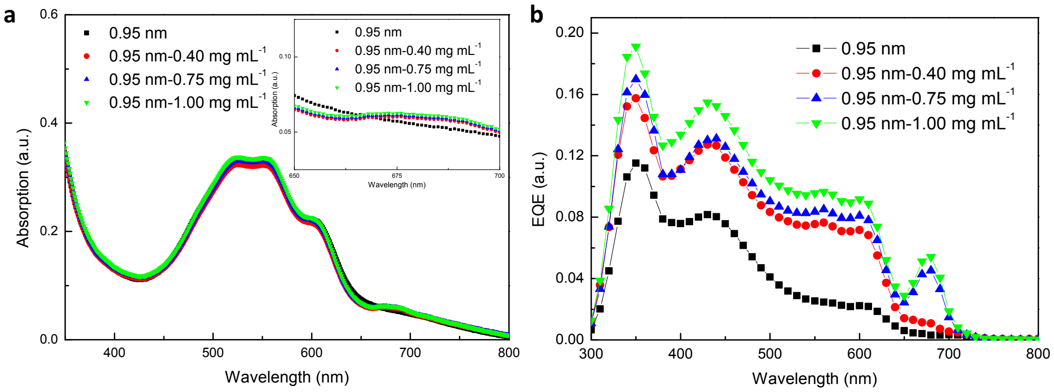

Figure 3.3.11 Absorption and EQE spectra for PCBM/CYTOP:F-SiPc//P3HT devices. a) Absorption spectra of TiO_2/PCBM/CYTOP:F-SiPc//P3HT films (inset: a magnified view of the range 650-700 nm) and b) EQE spectra of PCBM/CYTOP:F-SiPc//P3HT devices different dye concentrations.

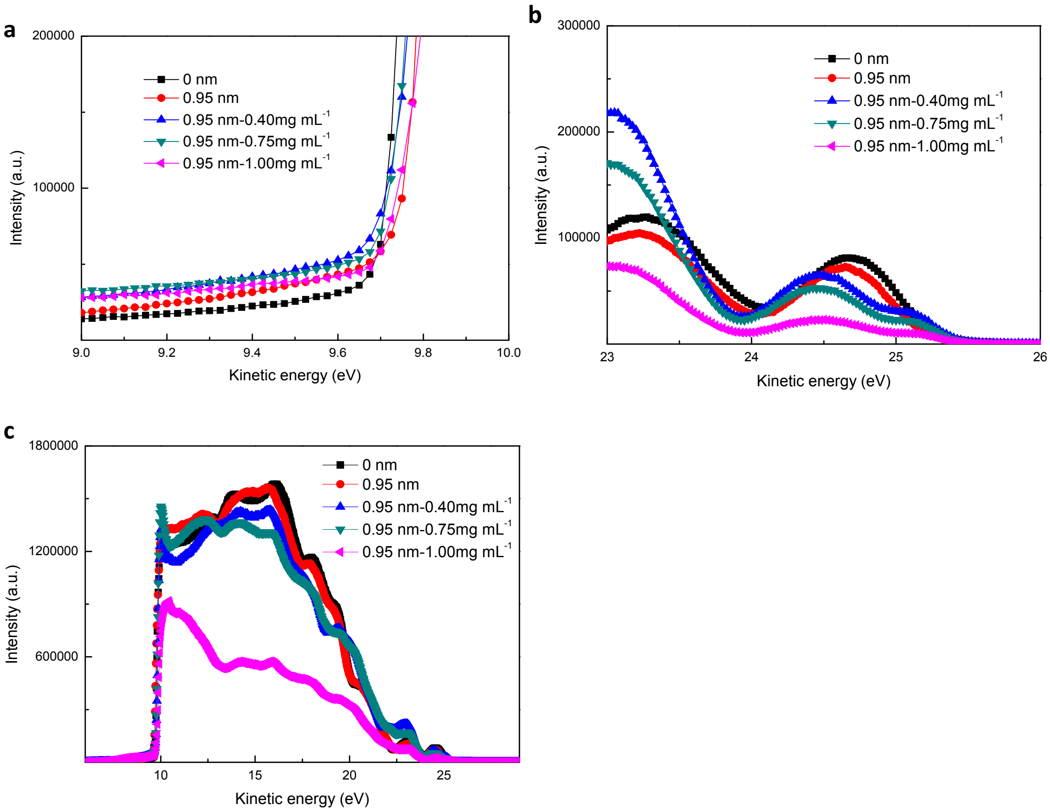

Figure 3.3.12 UPS measurement. a) Cutoff and b) Fermi-edge regions, and c) the whole range of the UPS spectra of ITO/PCBM/CYTOP:F-SiPc films with different F-SiPc concentrations in the CYTOP solution.

The device performance with different dye concentrations under AM1.5 irradiation are summarized in Figure 3.3.13. When the CYTOP layer was doped with a low concentration of F-SiPc (0.40 mg mL^{-1}), the J_{SC} of the device recovered from 0.81 to 1.40 mA cm^{-2}, whereas the V_{OC} remained at 0.60 V. As the amount of dye increased to 1.00 mg mL^{-1}, the V_{OC} decreased from 0.60 to 0.54 V, and J_{SC} increased from 1.40 to 2.20 mA cm^{-2}.

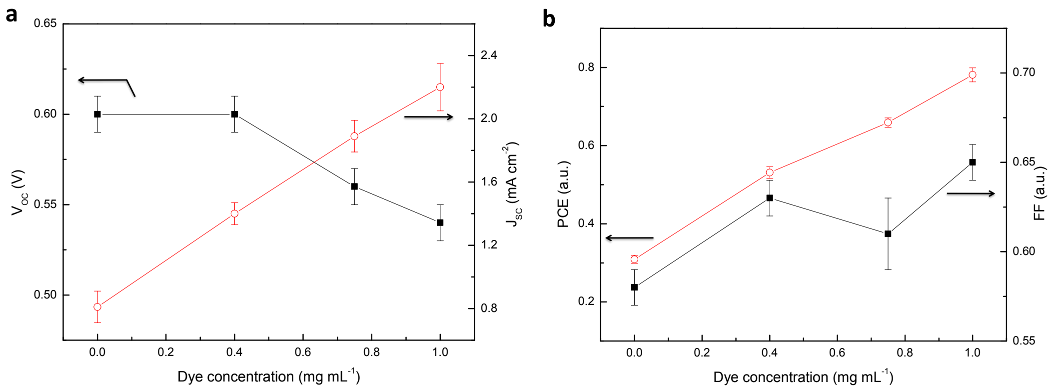

Figure 3.3.13 Dependence of device parameters of PCBM/CYTOP:F-SiPc//P3HT devices on the thickness of the CYTOP layer. Dependence of a) V_{OC} and J_{SC}, and b) FF and PCE.

The EQE plots in Figure 3.3.11 show that the increase in J_{SC} for a dye concentration of 0.40 mg mL^{-1} can be attributed to the increase in the photoresponse of P3HT and PCBM, and the response from the dye at 680 nm was negligible. This result indicates that the dye served as an energy acceptor from P3HT and as an efficient charge separation center at the interface. Photoluminescence of P3HT film was quenched by the presence of CYTOP:F-SiPc layer beneath, supporting the presence of the energy transfer process (see Figure 3.3.14). The average distance between the dye molecules in the 2D CYTOP layer at this concentration was calculated from the absorbance and absorption coefficient of SiPc. The distance was estimated as 6.1-12.2 nm, depending on the adapted absorption coefficient of SiPc.[31, 32] The distance is in the same range as the exciton diffusion length in P3HT, suggesting that excitons can be collected through the energy transfer process, even though the density is not high enough for light absorption. When the dye concentration reached 0.75 mg mL^{-1}, the EQE plot indicated the dye absorption at around 680 nm also began contributing to the photocurrent. Therefore, at high concentrations the dye acted as an energy acceptor and a light absorber.

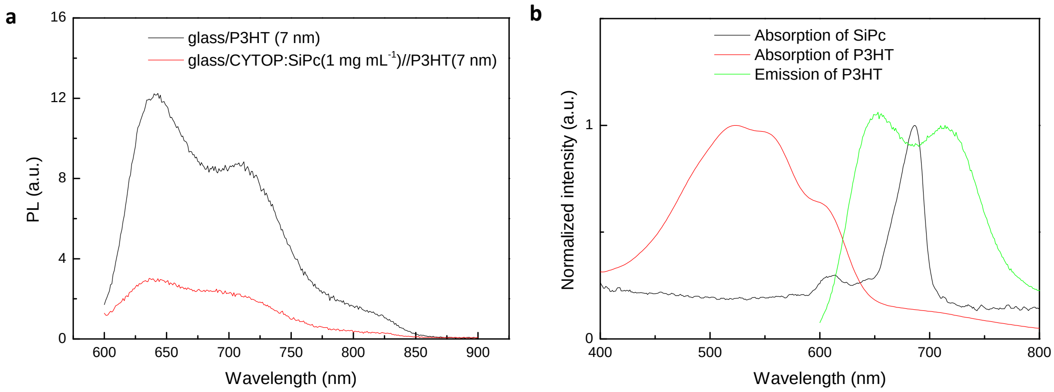

Figure 3.3.14 Photoluminescence (PL) spectra for a) glass/P3HT(7 nm) and glass/CYTOP:F-SiPc(1 mg mL^{-1})//P3HT(7 nm), excited at 550 nm and b) absorption spectra of P3HT and F-SiPc and PL of P3HT.

The effect of the dye concentration was analyzed based on the equivalent circuit for the PCBM/CYTOP:F-SiPc//P3HT devices. The parameters were extracted and plotted as the function of the dye concentration (Figure 3.3.15). When the dye concentration was low (0.40 mg mL^{-1}), both J_{00} and J_{ph} increased, although the increase in J_{00} was not as large as that of J_{ph}. As a result, the V_{OC} loss term, $-nkT\ln(J_{00}/J_{\mathrm{ph}}(V_{\mathrm{OC}}))$, decreased slightly. At low concentrations, the dyes in the CYTOP layer may not function as charge recombination sites, whereas they may work more efficiently as energy acceptors, because of the exciton diffusion and the long range interaction of Förster-type energy transfer. In contrast, the $n\phi$ term did not change upon the doping, indicating the D/A distance was independent of the dye concentration. However, at higher dye concentrations, J_{00} increased more rapidly than J_{ph} as the concentration increased, resulting in the increase of the loss term, $-nkT\ln(J_{00}/J_{ph}(V_{OC}))$. In this regime, the dye molecules could function as recombination sites. A slight decrease in the $n\phi$ term was also observed. This could be caused by the contribution of new CT states related to the P3HT/dye or dye/PCBM interfaces. Both the factors contributed to the decrease in V_{OC} from 0.60 to 0.54 V when the dye concentration was 1.0 mg mL^{-1}. Therefore, it may be important to optimize the low dye concentrations to achieve a high V_{OC}, because the dye can also act as a recombination site.

In the devices with only the F-SiPc dye layer (PCBM/F-SiPc//P3HT), J_{SC} monotonically increased as the concentration of F-SiPc increased due to the energy transfer and photocurrent from the F-SiPc absorption, although V_{OC} did not change substantially (see Figure 3.3.16). This indicates that the presence of the CYTOP layer is crucial for increasing V_{OC}. The equivalent circuit and temperature dependent measurements revealed that $\ln(J_{00})$ and $n\phi$ did not change for the PCBM/F-SiPc//P3HT devices as the dye concentration increased (see Figure 3.3.17). This suggests that the dye at the interface did not affect E_{CT} and changed only the $\ln(J_{ph}(V_{OC}))$ term. This could produce the very small change in V_{OC} through the $-nkT\ln(J_{00}/J_{ph}(V_{OC}))$ term.

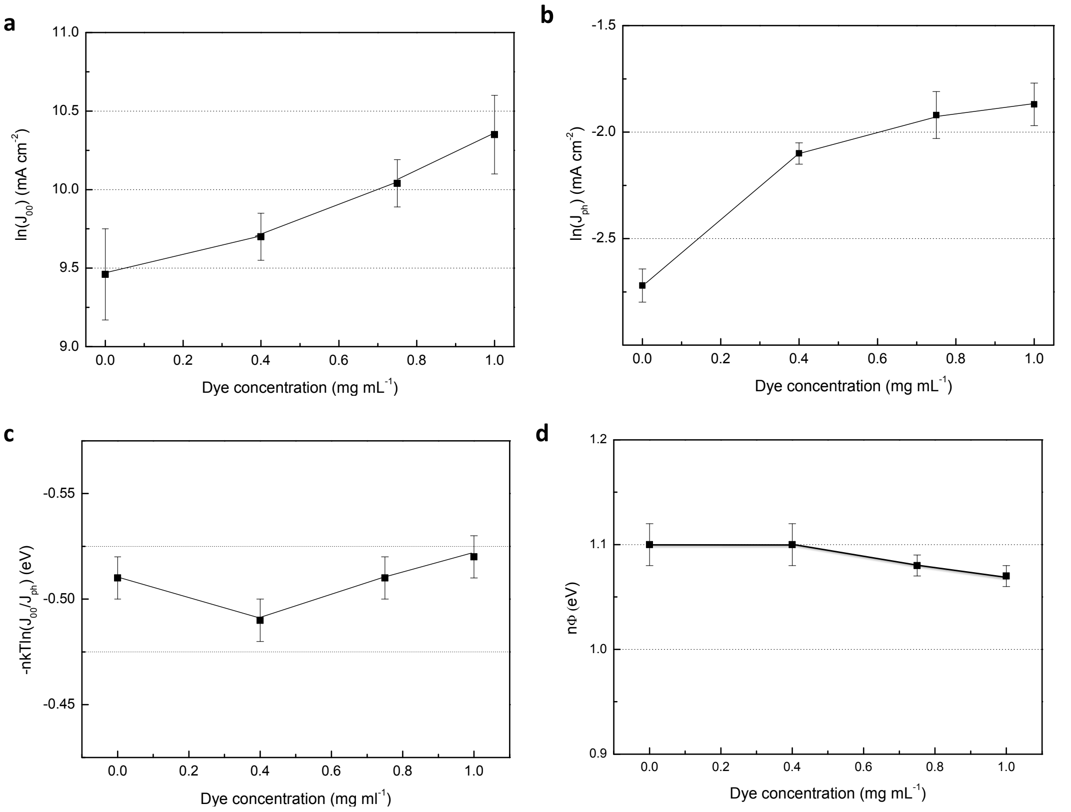

Figure 3.3.15 Parameters obtained from the variable temperature dark *J*-*V* curve measurements for the PCBM/CYTOP (0.95 nm):F-SiPc//P3HT devices. The dependence of a) $\ln(J_{00})$, b) $\ln(J_{ph}(V_{OC}))$, c) $-nkT\ln(J_{00}/J_{ph}(V_{OC}))$, and d) $n\phi$ on the concentration of F-SiPc in the CYTOP solution for the PCBM/CYTOP:F-SiPc//P3HT devices.

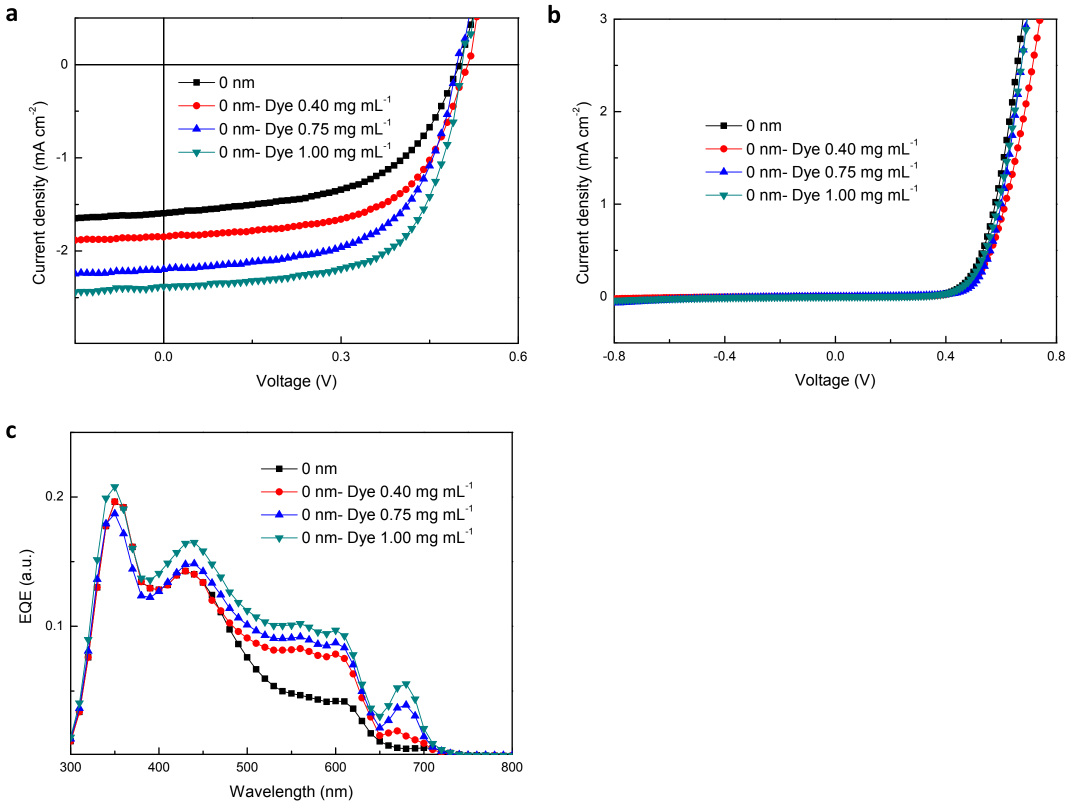

Figure 3.3.16 *J–V* characteristics and EQE measurement for PCBM/F-SiPc//P3HT. *J–V* characteristics (a) under AM1.5 irradiation and (b) under dark conditions. (c) EQE spectra of PCBM/F-SiPc//P3HT devices with different dye concentrations in the solution.

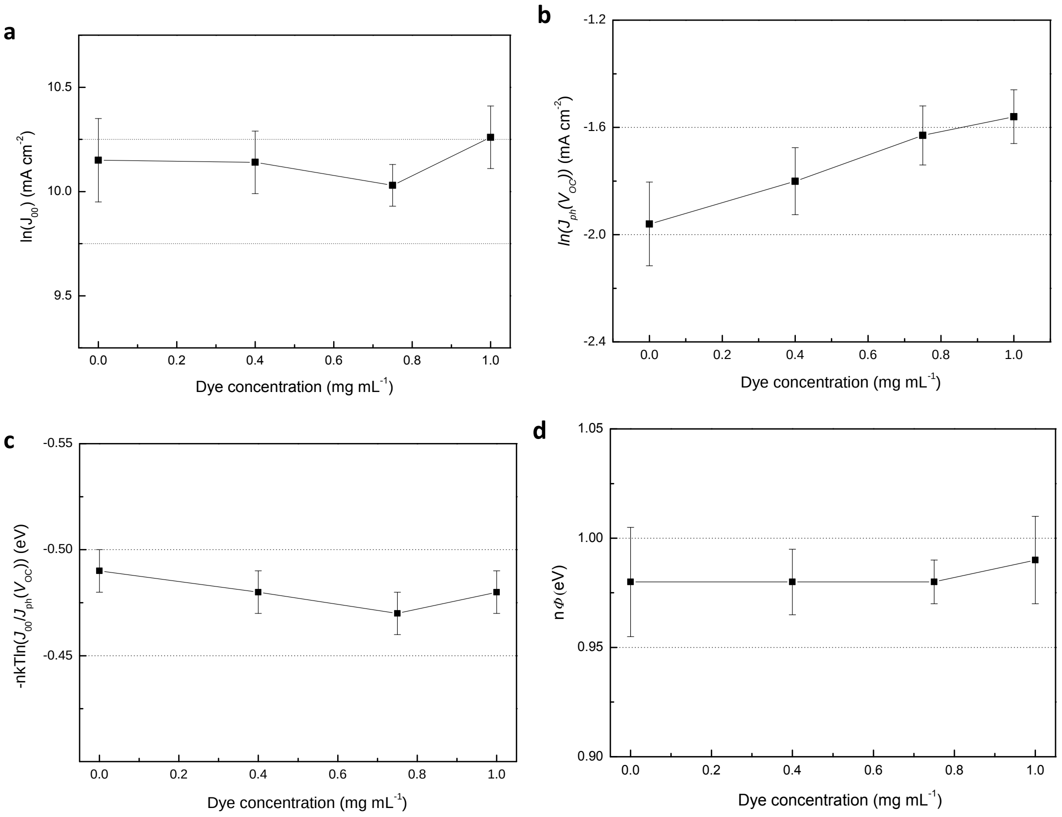

Figure 3.3.18 Parameters obtained from equivalent circuit analysis. Dependence of (a) $\ln(J_{00})$, (b) $\ln(J_{\mathrm{ph}}(V_{\mathrm{OC}}))$, (c) $-nkT\ln(J_{00}/J_{\mathrm{ph}}(V_{\mathrm{OC}}))$, and (d) $n\phi$ on the concentration of F-SiPc in solution for PCBM/F-SiPc//P3HT devices. The values were extracted from the variable-temperature dark *J*-*V* curve measurements.

3.4 Conclusion

In this chapter, the concept of ideal interface is proposed. It is demonstrated that placing a spacer layer between the donor and acceptor in bilayer OSCs can increase E_{CT} and suppress charge recombination, resulting in a higher V_{OC}. Although previous studies have focused on suppressing the charge recombination with spacers[16, 17], I found that the increase in E_{CT} was a more important factor for the V_{OC}. Doping the spacer layer with a dye increased the J_{SC} by the energy transfer and avoiding a reduction in V_{OC}. Ultimately, by using such ideal interface, the efficiency of device increased by 30%. But more importantly, the trade-off relationship was avoided in which I increased V_{OC} without losing J_{SC}. Our results offer a new route toward enhancing the efficiency of OSCs, which may also be applicable to BHJ structures if the well-defined donor and acceptor nanostructure interfaces can be modified in a similar way.

This is the pre-peer reviewed version of the following article: Zhong Y.F.; Tada A.; Izawa S.; Hashimoto K.; Tajima K.; Enhancement of V_{OC} without Loss of J_{SC} in Organic Solar Cells by Modification of Donor/Acceptor Interfaces, *Adv. Energy Mater.* **2013**, *4*, 1301332, which has been published in final form at [http://onlinelibrary.wiley.com/doi/10.1002/aenm.201301332/abstract]

Reference

1. J. You, L. Dou, K. Yoshimura, T. Kato, K. Ohya, T. Moriarty, K. Emery, C.-C. Chen, J. Gao, G. Li and Y. Yang, Nature Communication **4**, 1446, (2013).
2. E. J. Zhou, J. Z. Cong, K. Tajima, C. H. Yang and K. Hashimoto, Journal of Physical Chemistry C **116**, 2608, (2012).
3. E. J. Zhou, J. Z. Cong, K. Hashimoto and K. Tajima, Energy Environmental Science **5**, 9756, (2012).
4. E. J. Zhou, J. Z. Cong, K. Hashimoto and K. Tajima, Macromolecules **46**, 763, (2013).
5. M. C. Scharber, D. Mühlbacher, M. Koppe, P. Denk, C. Waldauf, A. J. Heeger and C. J. Brabec, Advanced Materials **18**, 789, (2006).
6. B. Rand, D. Burk and S. Forrest, Physical Review B **75**, 115327, (2007).
7. K. Vandewal, K. Tvingstedt, A. Gadisa, O. Inganas and J. V. Manca, Nature Materials **8**, 904, (2009).
8. D. Veldman, S. C. J. Meskers and R. A. J. Janssen, Advanced Function Materials **19**, 1939, (2009).
9. E. T. Hoke, K. Vandewal, J. A. Bartelt, W. R. Mateker, J. D. Douglas, R. Noriega, K. R. Graham, J. M. J. Frechet, A. Salleo and M. D. McGehee, Advanced Energy Materials **3**, 220, (2013).
10. D. Di Nuzzo, G.-J. A. H. Wetzelaer, R. K. M. Bouwer, V. S. Gevaerts, S. C. J. Meskers, J. C. Hummelen, P. W. M. Blom and R. A. J. Janssen, Advanced Energy Materials **3**, 85, (2013).
11. A. Tada, Y. F. Geng, Q. S. Wei, K. Hashimoto and K. Tajima, Nature Materials **10**, 450,

(2011).

12. Y. Zhong, J. Ma, K. Hashimoto and K. Tajima, Advanced Materials **25**, 1071, (2013).

13. K. R. Graham, P. Erwin, D. Nordlund, K. Vandewal, R. Li, G. O. Ngongang Ndjawa, E. T. Hoke, A. Salleo, M. E. Thompson, M. D. McGehee, and A. Amassian, Advanced Materials DOI: 10.1002/adma201301319, (2013).

14. M. D. Perez, C. Borek, S. R. Forrest, and M. E. Thompson, Journal of American Chemical Society **131**, 9281, (2009).

15. Z. T. Liu, M. F. Lo, H. B. Wang, T. W. Ng, V. A. L. Roy, C. S. Lee and S. T. Lee, Applied Physcs Letters **95**, 3222975, (2009).

16. I. H. Campbell and B. K. Crone, Applied Physcs Letters **101**, 4734505, (2012).

17. A. Kumar, G. Pace, A. A. Bakulin, J. F. Fang, P. K. H. Ho, W. T. S. Huck, R. H. Friend and N. C. Greenham, Energy Environmental Science **6**, 1589, (2013).

18. S. Honda, T. Nogami, H. Ohkita, H. Benten and S. Ito, ACS Applied Material Interfaces **1**, 804, (2009).

19. S. Honda, H. Ohkita, H. Benten and S. Ito, Chemical Communication **46**, 6596, (2010).

20. S. Honda, H. Ohkita, H. Benten and S. Ito, Advanced Energy Materials **1**, 588, (2011).

21. Q. Wei, S. Miyanishi, K. Tajima and K. Hashimoto, ACS Applied Material Interfaces **1**, 2660, (2009).

22. Q. Wei, K. Tajima and K. Hashimoto, ACS Applied Material Interfaces **1**, 1865, (2009).

23. Y. Geng, Q. Wei, K. Hashimoto and K. Tajima, Chemical Materials **23**, 4257, (2011).

24. W. J. Potscavage, A. Sharma and B. Kippelen, Accounts for Chemical Research **42**, 1758, (2009).

25. K. Vandewal, K. Tvingstedt, A. Gadisa, O. Inganas and J. V. Manca, Physical Review B **81**, 125204, (2010).

26. G. Richardson, C. Please, J. Foster and J. Kirkpatrick, SIAM Journal of Applied Mathematics **72**, 1792, (2012).

27. S. Yamamoto, A. Orimo, H. Ohkita, H. Benten and S. Ito, Advanced Energy Materials **2**, 229, (2012) .

28. H. L. Yip and A. K. Y. Jen, Energy Environmental Science **5**, 5994, (2012).

29. Y. J. He, H. Y. Chen, J. H. Hou and Y. F. Li, Journal of American Chemical Society **132**, 1377, (2010).

30. E. J. Zhou, J. Z. Cong, Q. S. Wei, K. Tajima, C. H. Yang and K. Hashimoto, Angewandte Chemie International Edition, **50**, 2799, (2011).

31. B. L. Wheeler, G. Nagasubramanian, A. J. Bard, L. A. Schechtman, D. R. Dininny and M. E. Kenney, Journal of American Chemical Society **106**, 7404, (1984).

32. S. Honda, S. Yokoya, H. Ohkita, H. Benten and S. Ito, Journal of Physical Chemistry C **115**, 11306 (2011) .

Chapter 4. Crystallization-induced Energy Level Change of [6,6]-Phenyl-C_{61}-butyric Acid Methyl Ester (PCBM) Film and Its Effect on Performance of Organic Solar Cells

4.1 Introduction

In high-performance organic solar cells (OSCs), [6,6]-phenyl-C_{61}-butyric acid methyl ester (PCBM) is often used as the electron acceptor in combination with semiconducting polymers and oligomers as donors. The crystallization of materials in OSCs could largely affect device performance by changing mixing morphologies and improve the efficiencies of charge separation, recombination, and collection in organic thin films.[1, 2] The crystallization of donor polymers has generally been considered as the key factor for improving OSC performance owing to improved charge separation or transport.[1, 3] Recently, however, the aggregation of PCBM in the films has also been regarded as an important phenomenon for achieving high performance in OSCs. The effect has been discussed in terms of charge delocalization in crystalline domains and the energy level cascade due to the difference in aggregation state.[4, 5]

It is widely accepted that the ionization potential (IP) of the donor and the electron affinity (EA) of the acceptor are key factors to determine the upper limit of open-circuit voltage (V_{OC}) and the efficiency of charge separation. The electronic structures of PCBM films have been investigated by several groups.[6, 7] Yet, how the crystallization of PCBM affects the energy levels has not been clarified, although they have primary importance for photovoltaic processes. Verploegen et al. reported the cold crystallization of PCBM films by thermal annealing at a temperature below the melting point and monitored the effect of blending PCBM with polymers on the crystallization of each component.[8] However, no study on the change in the electronic structure has been reported.

The energy levels of organic films are affected by many factors such as electronic polarization energy, intermolecular interaction, molecular orientation, surface dipole moment, and doping level.[10-12] It is generally difficult to distinguish between the effects of these factors as they simultaneously affect both IP and EA in different ways. Namely, the polarization energy affects the stabilization of charge carriers by the electronic polarization of the surrounding molecules. The magnitude of polarization energy is about 1 eV, which works to decrease IP and increase EA compared to those of singe molecule in vacuum. The enhancement of the intermolecular interaction widens the bandwidth of the energy level, resulting in the narrowing of the band gap, which is the difference between IP and EA. The other factors such as molecular orientation, surface dipole, and doping primarily affect both IP and EA at the same magnitude; they do not change the band gap.

Thus far, the above-mentioned effects on the energy level have been discussed only for the valence and core levels, determined using ultraviolet photoemission spectroscopy (UPS) and X-ray photoemission spectroscopy (XPS). No reliable information about unoccupied states or EA has been available owing to the lack of suitable experimental techniques. Inverse photoemission spectroscopy can be regarded as an inverse process of photoemission and an ideal method of examining unoccupied states. However, the obtained data is not precise enough to discuss changes on the order of 0.1 eV because of the low energy resolution[9] and damage to organic samples[10] due to electron bombardment. If EA can be determined as precisely as IP, it is possible to determine the factors that affect the energy level.

Recently, I have developed a new experimental method, low-energy inverse photoemission spectroscopy (LEIPS)[11,12]. Electrons with kinetic energy below the damage threshold of organic materials are introduced into the sample film and photons emitted owing to radiative transition to unoccupied states are detected. Since the electron energy is lower than the damage threshold[13], damage to organic samples is negligible. The energy of emitted photons falls in the range between 2 and 5 eV (i.e., the near-ultraviolet or visible range). These photons can be analyzed using band-pass filters with a high resolution and a high transmittance followed by the use of a highly sensitive photomultiplier. Thus far, this new technique has been applied to small-molecule organic semiconductors[14-16] and polymers[17] to determine EA at a precision higher than 0.1 eV.

In this research, I focus on the change in the energy level of PCBM films induced by thermal annealing. We find that spin-cast PCBM films thermally annealed above 150 ℃ crystallize and that their thickness decreases, in association with the change of the energy levels. By determining both IP and EA precisely, I can clearly distinguish the effects of polarization energy and intermolecular interaction from those of other factors.

Furthermore, in order to apply such change of interfacial energy level in BHJ device, the crystallization behavior of pristine PCBM film and PTB7:PCBM blended film (BHJ film) were investigated. A novel "epitaxy growth" method was used to introduce the crystallization into BHJ film and correspondingly increased V_{OC} of BHJ device.

4.2 Experiment

Sample Preparation. PCBM films are prepared by spin-coating, typically from $CHCl_3$ solution (10 mg/mL) at 1200 rpm for 60 second, resulting in the film thickness of ca. 73 nm. Thinner films (ca. 4 nm) were prepared by spin-coating from chlorobenzene solution (3 mg/mL) at 3000 rpm for 60 second and used for 2D GIXRD, UPS, XPS, LEIPS and LEET measurements. The substrates are ITO/glass for 2D GIXRD, UPS, XPS, LEIPS and LEET measurements, SiO_2 (500 nm)/Si for XRR and TiO_2/ITO/glass for GIXRD. Thermal annealing was conducted on a hot plate in a N_2 filled glove box at the designated temperatures for 5 min.

Measurements. UPS and XPS were performed on a PHI5000 VersaProbe II (ULVAC-PHI Inc.). UPS spectra were obtained with a He (I) excitation of 21.2 eV and a pass energy of 5 eV. Bias voltage of −5 V was applied to the samples in order to detect the cut-off region of secondary electrons. XPS spectra were obtained by using Al Kα radiation with the take-off angle of 90 °. XRR and GIXRD measurements were carried out on X-ray diffractometer (SmartLab, Rigaku, Japan) using monochromatized CuKα radiation (λ = 0.154 nm) generated at 45 kV and 200 mA. GIXRD was measured with the in-plane geometry at an incident angle of 0.21 °. 2D-GIXRD patterns were measured at an incident angle of 0.12 ° using synchrotron radiation at the beamline BL19B2 of SPring-8 with the approval of the Japan Synchrotron Radiation Research Institute.

Details about the low-energy inverse photoemission spectroscopy (LEIPS) setup are described elsewhere.[29] The sample specimen was introduced into the vacuum chamber evacuated below 1 x 10^{-7} Pa and incident to an electron beam. In order to avoid the sample damage, the kinetic energy of incident electrons was restricted to less than 4 eV and the electron current densities ranged between 10^{-6} and 10^{-5} A cm^{-2}. Under these experimental conditions, the same IPES spectra were obtained after several scans confirming the sample damage was negligible. The emitted photons were collected and focused into a photon detector consisting of an optical bandpass filter and a photomultiplier tube. The center wavelengths of the bandpass filters were 254 nm, 280 nm and 285 nm. The overall energy resolution was estimated to be 0.3 eV. The low energy electron transmission (LEET) spectroscopy was carried out on the same apparatus and sample films as the LEIPS. The electron current $I(E_k)$ was measured as a function of electron kinetic energy E_k and the LEET spectrum was obtained as the first derivative $dI(E_k)/dE_k$. The peak corresponds to the vacuum level of the sample.

4.3 Results and Discussions

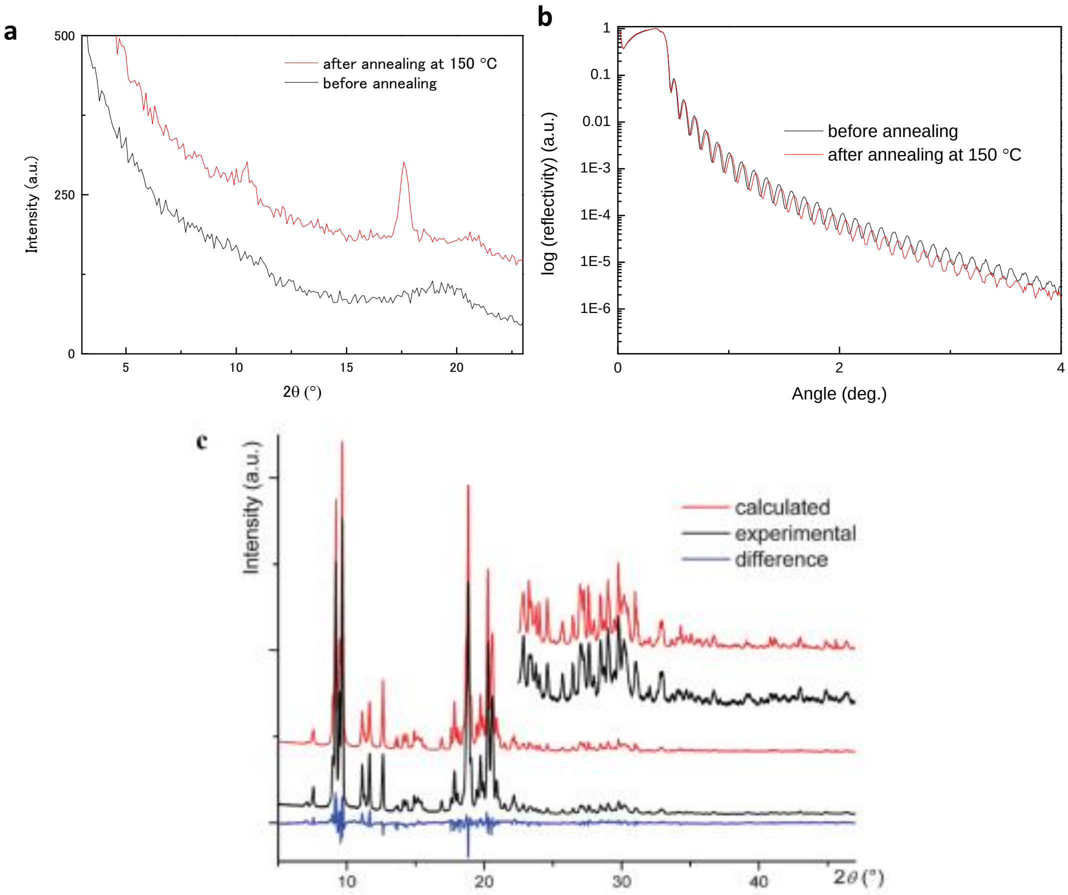

Figure 4.3.1.a) In-plane GIXRD and b) XRR patterns of PCBM/TiO_2/ITO sample before and after the annealing at 150 ℃ for 5 min. c) Experimental, calculated (also expanded 7) and difference powder diffraction profiles (Cu-Ka radiation) for the n-PCBM crystal structure. Figure is reproduced from ref. 18 with permission. Copyright 2014, RSC. Acknowledgements for reproduction of RSC material in RSC publications.

Figure 4.3.1a shows the in-plane grazing incidence X-ray diffraction (GIXRD) patterns of the PCBM films on the TiO_2/ITO substrate before and after annealing. The film before annealing showed a broad peak at 2θ of 19.7 ° (d = 0.472 nm calculated from the top of the peak), indicating a disordered structure of PCBM in the film. After annealing the film at 150 ℃ for 5 min, the broad peak at approximately 19.7 ° became smaller, a sharp peak at 17.6 ° (*d* = 0.539 nm) emerged, and relatively broad peaks appeared at 10.2 ° and 20.7 °. This change suggests the crystallization of PCBM films upon thermal annealing. The annealing temperature was changed from 50 ℃ to 150 ℃, and it was confirmed that the crystallization started occurring above 140 ℃ (see Figure 4.3.2a). This crystallization behavior is consistent with the previous report by Verploegen et al.[8] The 2D GIXRD patterns of the films were also measured by using synchrotron radiation. Although only a broad ring was observed in the film before the annealing, clear diffractions are observed as spots after the annealing (see Figure 4.3.2). This result indicates not only that the film is crystalline after the thermal annealing but also that the domain is preferentially oriented in the film. Although there are several reports on the structural analysis of single-crystal PCBM, I could not identify the structure of the film using known phases.[18, 19] Considering distance between PCBM molecules (~1 nm, center to center of C_{60} cage, 110), peak appear around 10 ° is reasonable (d spacing ~0.902 nm). On the other hand, d spacing (*d* = 0.539 nm) of sharp peak around 17.6 ° is typically smaller than the above value. By comparing with reported powder X-ray, there is similar peak appeared in the same region (Figure 4.3.1c), suggesting this peak should come from crystalline PCBM. In addition, by calculating d spacing from 2DXRD data (Figure 4.3.2b), d= 1.046/0.697/0.502/0.546 nm were obtained, in which similar d value (0.546 nm) could be found compared to that from GIXRD (0.539 nm), further proving emerged peak around 17.6 ° coming from crystalline PCBM. However, there is no report signing such peak to any crystal structure of PCBM, identifying origin of this peak is currently difficult, further detailed study of the crystal structure in PCBM films is needed.

The changes in the film thickness and the density before and after the annealing were examined using X-ray reflectivity (XRR) for the PCBM/SiO_2/Si samples. As shown in Figure 1b, both samples showed clear fringes due to the interference of X-rays corresponding to the thickness of the PCBM layers. Before the annealing, the fitting of the data with the bilayer model gave a thickness of 75.24 ± 0.26 nm and a density of 1.644 ±0.021 g cm^{-3}. After the annealing, the fringes shifted to a lower angle and the reflectivity decreased. The fitting of the XRR data gave a thickness of 73.33 ± 0.35 nm and a density of 1.686 ±0.011 g cm^{-3}. These changes indicate a decrease in PCBM film thickness and an increase in the density upon the crystallization. The thickness is found to be reduced by 2.54 ±0.60% and the density to be increased by 2.58 ±1.5%. The change of the density agrees well with that of the thickness, suggesting that the film shrinks along the direction perpendicular to the substrate. Note that XPS measurements of the films confirm the absence of solvent ($CHCl_3$ or chlorobenzene) residue in the films (see Figure 4.3.2), indicating that the film consists of pure PCBM and is not a co-crystal with the solvent, as in previous report on single-crystal PCBM.[20] This result suggests the increase in film density upon crystallization.

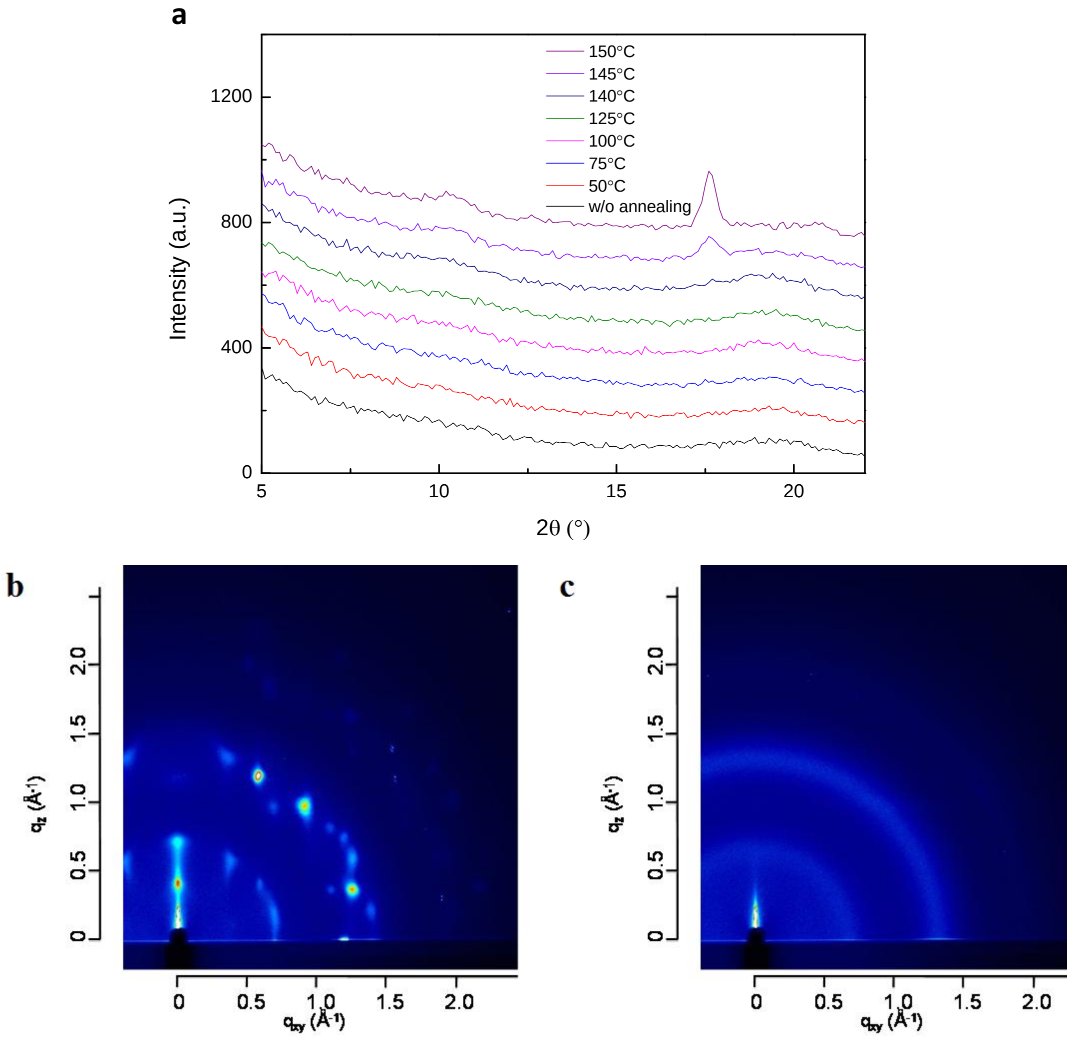

Figure 4.3.2 a) In-plane GIXRD patterns for PCBM/TiO$_2$/ITO at the different annealing temperatures. The crystallization starts happening at 140 ℃ and the peak around 17.6° gradually increase at higher annealing temperature up to 150 ℃. 2D GIXRD patterns of PCBM/ITO film b) after and c) before the annealing at 150 ℃ for 5 min. Only a broad ring was observed in the film before the annealing, while clear diffractions are observed as spots after the annealing.

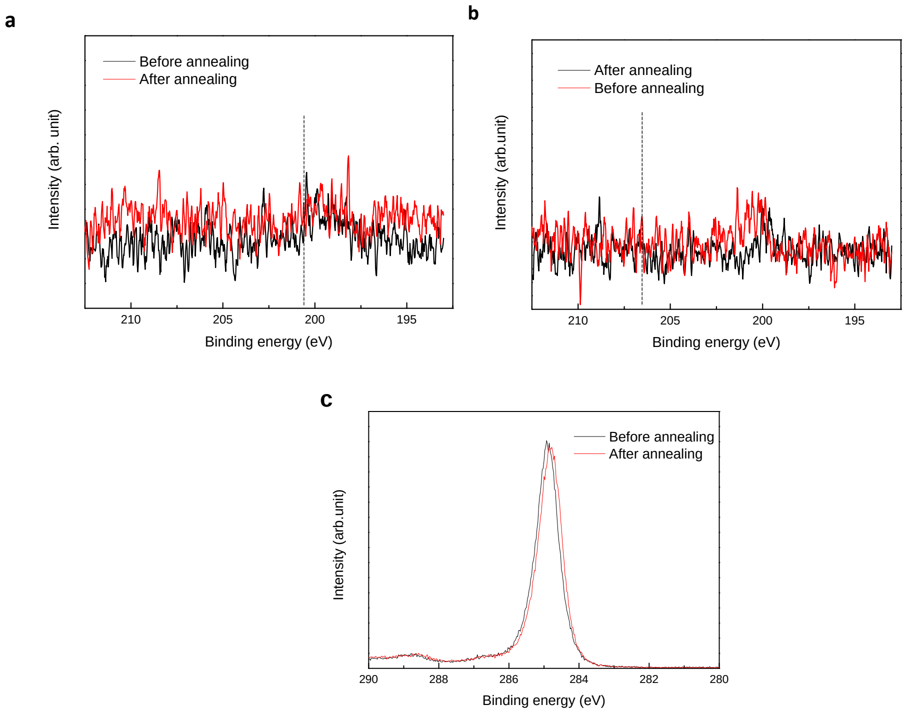

Figure 4.3.3 XPS measurements of PCBM/ITO in the regions of a) Cl2p for PCBM spin-coated from chlorobenzene [binding energy of Cl in C_6H_5Cl (200.5 eV) is indicated by a dashed line], b) Cl2p for PCBM spin-coated from $CHCl_3$ [binding energy of Cl in $CHCl_3$ (206.8 eV) is indicated by a dashed line] and c) C1s peaks before and after annealing. No Cl2p peak was observed, indicating the absence of solvent residue in the PCBM film. The shift of the C1s peak was clearly observed after annealing. Peak maxima were obtained by Gaussian fitting for five different points from the same sample, which gives 284.97±0.04 eV and 284.79±0.04 eV for the PCBM film before and after annealing, respectively.

Ultraviolet photoelectron spectroscopy (UPS) was performed on the samples to monitor the change in the valence energy and vacuum level (VL) of the PCBM films induced by the annealing at 150 °C. As shown in Figure 4.3.4, a small difference in the cutoff energy of secondary electrons was found after the annealing (4.29 and 4.31 eV before and after the annealing, respectively). This indicates little change in VL relative to the Fermi level (E_F) after the annealing. In Figure 2a, the onset of the spectrum in the highest occupied molecular orbital (HOMO) edge region shifted from 1.71 to 1.50 eV after the annealing, indicating that the peak consisting of the HOMO of PCBM shifted upward by 0.21 eV relative to E_F. The maximum of the peak also shifted from 2.32 to 2.07 eV indicating a shift by +0.25 eV. IP was determined as the onset energy of the HOMO peak with respect to the VLs. The IPs were 5.95 and 5.74 eV before and after the annealing, respectively. For the peak width, the full width at half-maximum (FWHM) of the HOMO peak was broadened by only 0.03 eV after annealing which was judged from the peak fitted with a Gaussian function. This result suggests a subtle enhancement of the intermolecular coupling of PCBM after the annealing, that is, due to the crystallization.

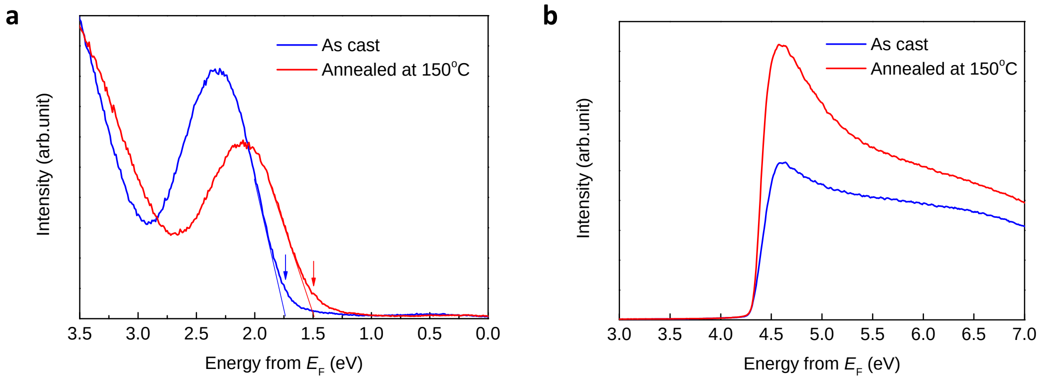

Figure 4.3.4 UPS profiles of PCBM films before and after the annealing at 150 ℃ for 5 min in the a) HOMO edge and b) cutoff regions. The energies are with reference to the Fermi levels. Arrows indicate the onset energies.

XPS was conducted on the films to investigate the energy level change in the core level. The core levels are highly localized and not affected by the change of the bandwidth due to the intermolecular interaction. The C1s energies before and the after the annealing were 284.97±0.04 eV and 284.79±0.04 eV, respectively, resulting in the upward shift of the core level by 0.18 eV with respect to E_F (see Figure 4.3.3). The decrease of the binding energy is in a good agreement with that of IP within the experimental uncertainties.

To investigate the change in the EA of PCBM, LEIPS measurements were performed on the films.[11] Figure 3a shows that the onset of the LUMO peak shifts by about 0.1 eV before and after the annealing. Low-energy electron transmission (LEET) measurements of the same films showed that the VLs are 4.80 and 4.76 eV above E_F, respectively (Figure 4.3.5b). The difference in VL between before and after the annealing was −0.04 eV. The magnitude of the VL shifts is in good agreement with those determined by the cutoff energy of secondary electrons in the UPS measurement, as shown before. This confirms that UPS and LEIPS showed consistent results despite the fact that they were performed using different apparatuses. The absolute VLs determined by secondary electrons of UPS and the peak of LEET differ by a few tenths of eV. Although VL with respect to E_F may sensitively change, for example, with exposure to air, the HOMO and LUMO levels are expected to remain unchanged with respect to VL [21, 22].

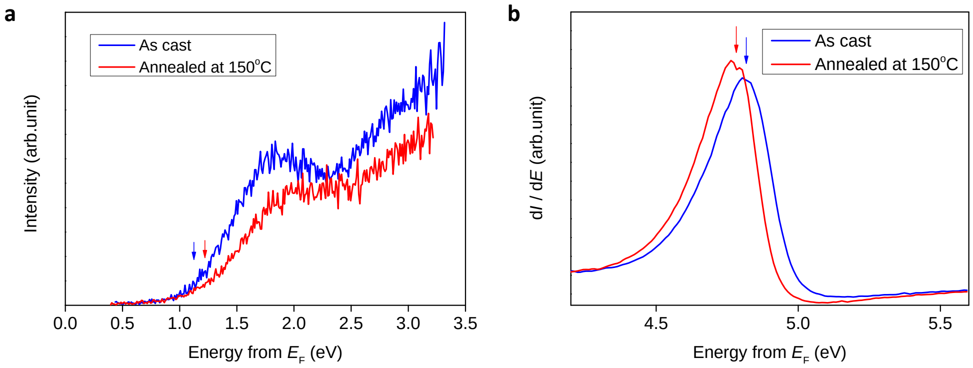

Figure 4.3.5 a) LEIPS and b) LEET measurements of PCBM film before and after the annealing at 150 ℃ for 5 min.

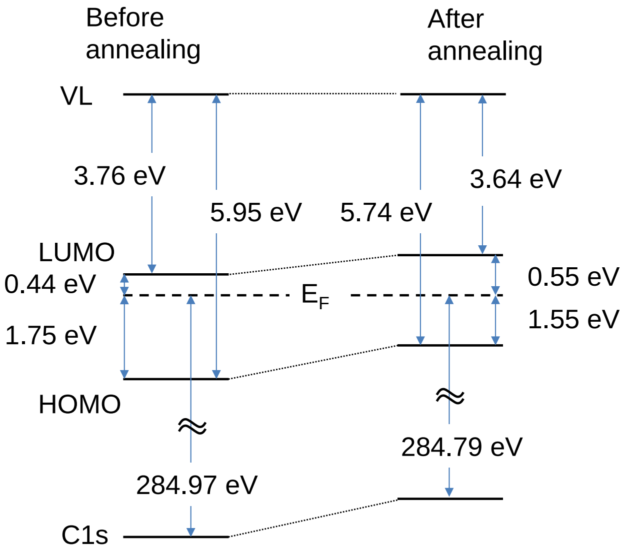

Figure 4.3.6. Schematic energy diagram of PCBM films before and after the crystallization. *y*-axis is relative to the Fermi level but not in scale.

The polarization energy is the stabilization energy for an ionized species (P_+ and P_- for a cation and an anion, respectively) due to the electronic polarization of the surrounding molecules [23]. An increase in the density of the surrounding media around an ionized molecule should lead to an increase in the polarization energy. In the present study, the XRR result shows that the crystallization increases the density of the film; therefore, I expect a larger polarization energy after the annealing. Here, I estimate the difference in P_+ and P_- due to the increase in the density of thin films using a simple model.[24] The electrostatic interaction between an ionized molecule and the surrounding molecules is approximated by that between the point charge and the induced dipole. In this case, P is given by

$$P = 8.25(e)^2 \alpha N^{\frac{4}{3}},$$

where e is the charge of an electron, α is the average molecular polarizability, and N is the number density of molecules. According to this equation, the decrease in the film volume by 3% could induce a 4% increase in P. For PCBM, the reported P_+ and P_- are 1.21 eV and 1.20 eV, respectively. [6, 25] The result shows that the increase in the film density gives rise to a 0.05 eV increase in the polarization energy for both P+ and P^-, resulting in a reduction in the band gap by 0.1 eV. Therefore, the P change caused by the densification of the film could quantitatively explain the band gap narrowing.

Another possible cause of band gap narrowing is the enhancement of intermolecular interaction. This should be associated with the broadening of the HOMO and LUMO peaks. However, the observed HOMO peak is broadened only by 0.03 eV (FWHM), which is much smaller than the change in the band gap (0.09 eV). These results suggest that the contribution of changes in intermolecular interaction is negligible. This conclusion is further supported by the following experimental findings. First, there is virtually no change in the optical gap observed in the photoabsorption spectra of the films (see Figure 4.3.6). Second, the change in the C1s peak position (0.18 eV) occurs close to that of the HOMO peak (0.21 eV) suggesting that the effect is predominantly electrostatic rather than the broadening is induced by intermolecular interaction.

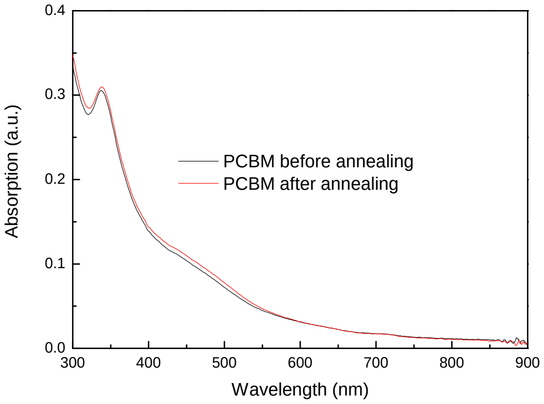

Figure 4.3.6 Transmittance absorption spectrum for PCBM film before and after the annealing on quartz substrate.

In addition to the band gap narrowing, the energy levels shifted upward relative to both VL and E_F after the annealing, as shown in Figure 4. Although the reasons for the observed changes are not clear at this moment, I speculated that both molecular orientation and doping level could contribute to the changes. Since the crystallized film shows preferential orientation in the films as shown by the 2D GIXRD patterns, it is possible that the film surface has a particular molecular orientation after the annealing, resulting in the formation of a molecular dipole layer.[26] On the other hand, a small amount of impurities in PCBM could serve as unintentional dopants and be removed, associated with the crystallization by the thermal annealing in N_2. Possible dopants could be oxygen or oxygenated compounds. Bao et al. observed a decrease in the work function of PCBM films by 0.15 eV with exposure to O_2 gas, which was attributed to n-doping.[27] The magnitude of the upward shift of 0.1-0.2 eV in IP and EA observed in the present work is comparable to the reported shift due to oxygen exposure. In our case, the small amount of oxygen included in the PCBM film during the exposure to air might be released upon the annealing. If such de-doping of an n-type dopant is assumed, E_F should shift downward and both HOMO and LUMO bands should shift upward relative to the VL. [28-30] The change in E_F after the crystallization could compensate for the shifts in the VL, resulting in no apparent change in the VL. According to this picture, the estimated VL shift induced by the crystallization is −0.15 eV.

Device performance

To directly correlate between the change of EA in PCBM films by the thermal annealing and the behavior as the electron acceptor in OSCs, I fabricated bilayer OSCs devices by using contact film transfer (CFT) method. This method allowed constructing well-defined bilayer structure by using the same polymer films, so the changes in the transport and the absorption properties in the donor phase could be excluded and the changes of the properties in PCBM films could be directly correlated to the device performances. Poly[[4,8-bis[(2-ethylhexyl)oxy]benzo[1,2-b:4,5-b’]dithiophene-2,6-diyl][3-fluoro-2-[(2-ethylhexyl)carbonyl]-thieno[3,4-b]thiophenediyl]] (PTB7) was used as the donor material. The chemical structures of PTB7 and PCBM, and current density-voltage (*J*-*V*) curves of devices without or with PCBM layer annealed at 150 ℃ are shown in Figure 4.3.7a and Figure 4.3.7b. The energy diagram was listed in Figure 4.3.7c, the IP of PTB7 was measured by UPS and EA was taken by optical band gap. The open circuit voltage (V_{OC}) of the device was 0.71 V and 0.84 V for device without and with annealing PCBM layer at 150 ℃ before transferring PTB7 film. Since V_{OC} is closely related to the difference of HOMO of the donor and LUMO of acceptor (E_{DA}), the change of V_{OC} (0.13 V) is in good agreement of that of E_{DA} (0.12 eV). The detailed analysis of device performance was provided in Figure 4.3.8. On the other hand, there is a notable decrease in J_{SC}, as shown in the *J*-*V* curves in Figure 4.3.7a. Although crystallization is usually believed to increase the device performance, the situation of PCBM observed here is in completely different manner. Possible reason could be smaller LUMO offset (decrease from 0.45 to 0.33 eV) which is the driving force for charge separation. Further investigation is needed to reveal the origin of J_{SC} change here.

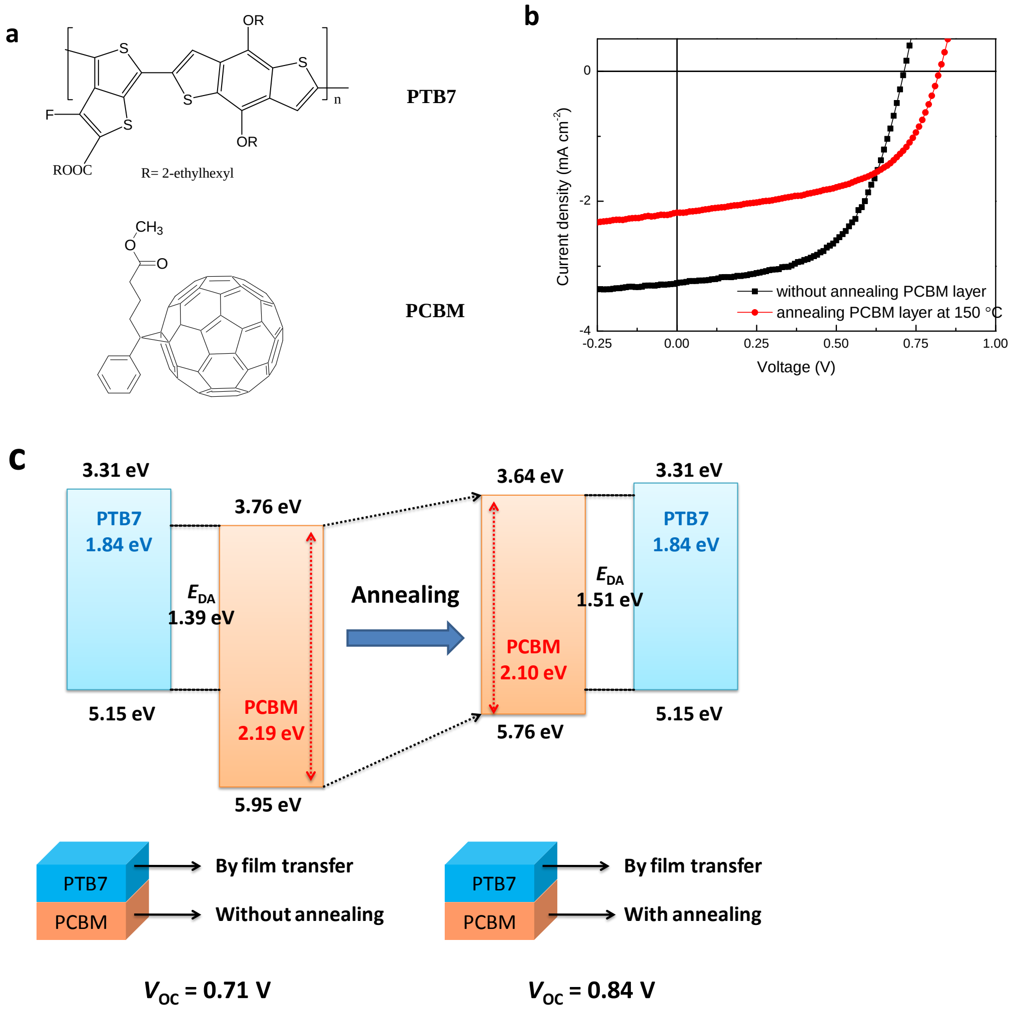

Figure 4.3.7. a) Chemical structures of PTB7 and PCBM, b)*J*-*V* curves for the devices without or with PCBM layer annealed at 150 ℃. c) Energy diagrams for bilayer devices of PCBM//PTB7 without or with PCBM layer annealed at 150 ℃ before transfer of PTB7 layer.

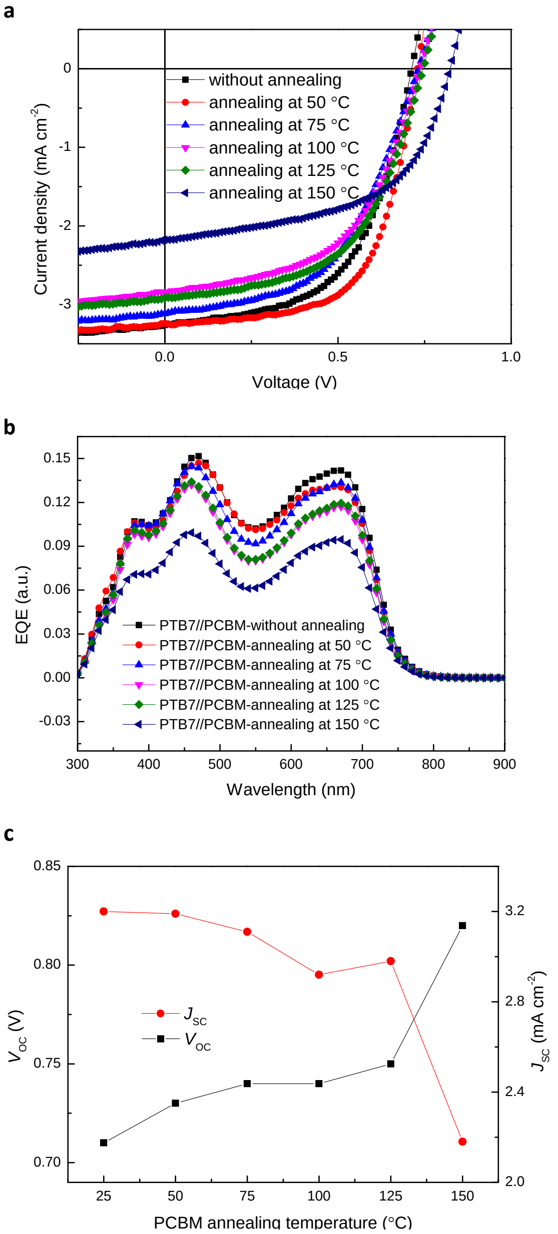

Figure 4.3.8 Detailed device performance change after annealing PCBM layer under different temperature. a) *J-V* curves, b) EQE spectrum, and c) change of V_{OC} and J_{SC}.

By using the above bilayer devices, I clearly see that V_{OC} of device can be increased due to the change of energy level induced by crystallization of PCBM. In order to further utilize such change of interfacial energy levels in BHJ OSCs. The crystallization behavior of pristine PCBM film and PTB7:PCBM blended (BHJ film) were studied. As shown in Figure 4.3.9, use of ITO or TiO_2 as substrate does not affect the crystallization of PCBM which is confirmed by the sharp peak around 17.5 °. This result suggested the crystallization of PCBM might not be affected by the substrate (ITO of TiO_2). (Note that the peak around 26 °came from TiO_2)

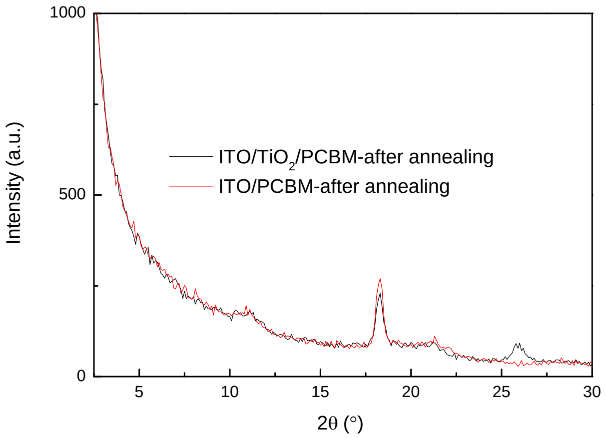

Figure 4.3.9 XRD pattern for ITO/TiO_2/PCBM film and ITO/PCBM film after annealing.

However, the crystallization of PCBM was stopped if another PTB7 film was transfer onto PCBM film, as indicated in Figure 4.3.10a, only a broad peak around 20 ° was observed after annealing, suggesting PCBM beneath PTB7 is still amorphous. This result suggested PCBM/air interface might play an important role in crystallization of PCBM film. In order to certify the above assumption, SSM was utilized. As shown in Figure 4.3.10b, FC_8 molecule was blended with PCBM, and flow to the top of film, forming SSM. After annealing however, the crystallization was still prevented even with just a monolayer FC_8 at PCBM/air interface. This result indicated that crystallization of PCBM might be a top down process which started from PCBM/air interface.

As next step, donor polymer PTB7 was blended with PCBM to form BHJ film. After annealing, broad peak around 20 ° was still observed, suggesting crystallization of PCBM was prevented when blending with PTB7. This results indicated that in conventional BHJ OSCs, PCBM was amorphous or crystalline domain is very small due to the existence of donor polymer.

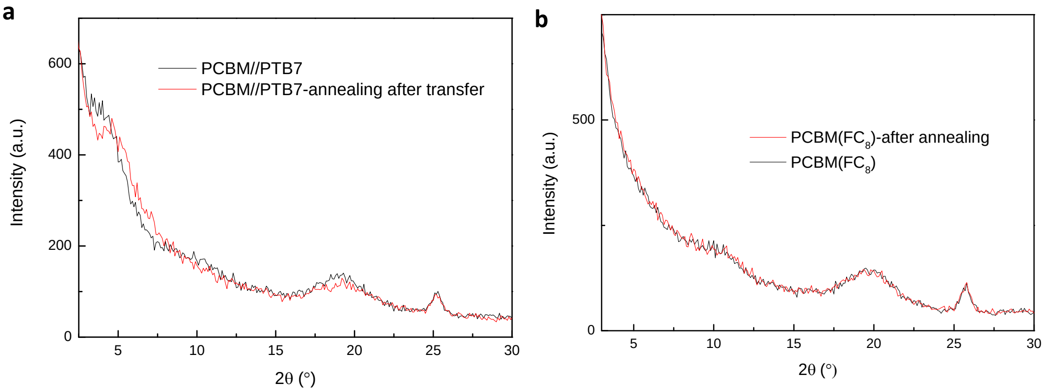

Figure 4.3.10 XRD pattern for a) PCBM//PTB7 before and after annealing (after transfer PTB7), b) PCBM(FC_8) film before and after annealing.

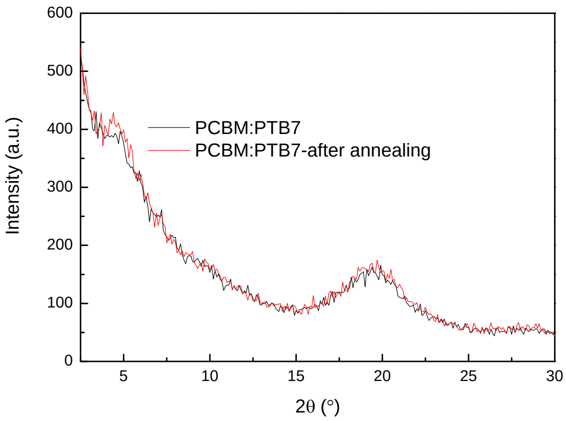

Figure 4.3.11 XRD pattern for PCBM:PTB7 (BHJ) film before and after annealing.

In order to introduce the crystalline PCBM into BHJ film, a novel "epitaxy growth" was purposed. As indicated Figure 4.3.12, a PCBM layer was annealed to be a crystalline PCBM layer. This layer works as seed layer. After that, a BHJ layer comprise of PCBM and PTB7 was transferred onto the seed layer. Then post annealing was carried out to introduce the crystallization bottom up. This is certified by the XRD measurement. The black line is the seed layer, after annealing seed layer PCBM stated to crystallize and have a sharp peak around 17.5 °. After transfer of BHJ film onto this crystallized seed layer (red), a broad peak appeared due to the amorphous PCBM in BHJ film on top. However, this broad peak vanished and sharp peak around 17.5 °increased after post annealing, suggesting the amorphous PCBM in BHJ film stated to crystallize. These results indicated the "expitaxy growth" introduced the crystallization of PCBM into BHJ film through a bottom up approach.

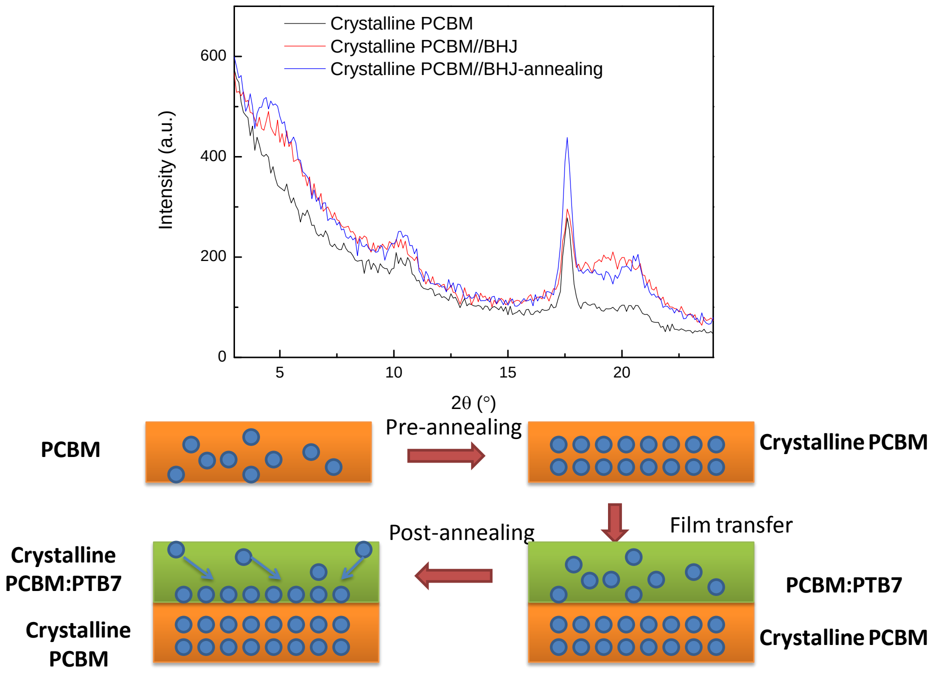

Figure 4.3.12 XRD pattern schematic images for "epitaxy growth" of crystalline PCBM.

By using the above strategy, a BHJ device was fabricated, utilizing crystallized PCBM. The structure was shown in Figure 4.3.13. A seed layer PCBM was added beneath BHJ layer PCBM:PTB7. The device performance was summarized in Table

4.3.1. The results showed that by directly annealing BHJ device without seed layer, the V_{OC} of device does not change. This is due to the prevention of PCBM crystallization in presence of PTB7. After insertion of seed layer PCBM beneath BHJ layer, V_{OC} of device still remained around 0.76 V after post-annealing, this is because the seed layer is not pre-annealed to introduce the crystallization into BHJ film. However, once the seed layer is crystallized, the post annealing can help to introduce the crystallization in the seed layer into BHJ layer. The V_{OC} of device increased to 0.83 V which is similar as in bilayer device case.

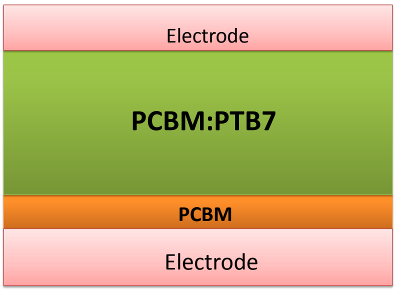

Figure 4.3.13 Device structure of BHJ cell utilizing "epitaxy growth".

Table 4.3.1 Device performance of BHJ cells.

Sample	Pre-anneal	Post-anneal	V_{OC} (V)	J_{SC} (mA/cm^2)	FF	PCE (%)
BHJ	/	/	0.74	6.34	0.22	1.03%
BHJ	/	150	0.77	10.73	0.37	3.05%
PCBM//BHJ	/	150	0.76	10.20	0.35	2.71%
PCBM//BHJ	150	150	0.83	4.25	0.33	1.16%

On the other hand, the current density of device decreased from 10.20 to 4.25 mA/cm^2 after crystallization of PCBM. This could be attributed to the same reason as

I explained in bilayer device. Furthermore, the un-optimized morphology could also reduce the current density. Further investigation or optimization of the device is needed to clarify the change of J_{SC}.

The above results of device performance suggested that the change of V_{OC} of device is due to the crystallization of PCBM in BHJ layer, causing the change of energy levels. These results suggested that crystallization of PCBM can be used as a tool to introduce the change of interfacial property like energy levels into BHJ device.

4.4 Conclusion

We observed a significant change in the energy level of PCBM films upon thermal annealing accompanied by the crystallization of the films. From a precise analysis of IP, EA and the core level, I conclude that the band gap narrowing is most likely attributed to the polarization energy due to the increase in film density. The effect of the enhancement of intermolecular interaction upon crystallization could be neglected. Other factors such as a change in molecular orientation and de-doping may also affect the rigid shift in the HOMO and LUMO levels; in other words, IP and EA change by the same magnitude.

For the calculation of the polarization energy, positive and negative charges are assumed to be point charges. Despite its simplicity, this model could explain the change in the band gap reasonably well, suggesting that charge carriers in PCBM films localized on a single PCBM molecule in the ground state. This picture is consistent with the low mobility of charge carriers in PCBM films.[16]

It is noteworthy that the change in the energy level should occur upon densification even without a change of intermolecular interactions. This fact seems to have been overlooked in the discussion of possible cascading energy diagrams in bulk heterojunction structures. The current finding obtained by LEIPS suggests that crystallized, high-density PCBM in OSCs could have significantly different energy levels from noncrystallized domains through polarization energy changes. This could potentially help to understand the factors that make PCBM the most successful electron acceptor in OSCs.

Moreover, bilayer OSCs was utilized to investigate how crystalline PCBM affects device performance. The results showed that due to higher lying LUMO of crystalline PCBM, V_{OC} of device using crystalline PCBM was 0.13 V higher than that of amorphous PCBM. This result agreed well with the change of energy levels. In order to utilized crystalline PCBM in BHJ device to have higher V_{OC}, "epitaxy growth" was purposed to introduce crystallization of PCBM into BHJ layer. The results were certified by XRD measurement and device performance. These results suggested crystallization of PCBM could be used as a tool to introduce change of interfacial property like energy levels into BHJ device to increase V_{OC} of device.

Reference

1. T. M. Clarke, A. M. Ballantyne, J. Nelson, D. D. C. Bradley and J. R. Durrant, *Adv. Func. Mater.* **18**, 4029-4035 (2008).
2. T. M. C. a. J. R. Durrant, *Chem. Rev.* **110**, 6736-6767 (2010).
3. G. Li, V. Shrotriya, J. Huang, Y. Yao, T. Moriarty, K. Emery and Y. Yang, *Nat. Mater.* **4**, 864-868 (2005).
4. F. C. Jamieson, E. B. Domingo, T. McCarthy-Ward, M. Heeney, N. Stingelin and J. R. Durrant, *Chem. Sci.* **3**, 485-492 (2012).
5. S. Gelinas, A. Rao, A. Kumar, S. L. Smith, A. W. Chin, J. Clark, T. S. van der Poll, G. C. Bazan and R. H. Friend, *Science* **343**, 512-516 (2014).
6. K. Akaike, K. Kanai, H. Yoshida, J. y. Tsutsumi, T. Nishi, N. Sato, Y. Ouchi and K. Seki, *J. Appl. Phys.* **104**, 023710 (2008).
7. Z.-L. Guan, J. B. Kim, H. Wang, C. Jaye, D. A. Fischer, Y.-L. Loo and A. Kahn, *Org. Electron.* **11**, 1779-1785 (2010).
8. E. Verploegen, R. Mondal, C. J. Bettinger, S. Sok, M. F. Toney and Z. Bao, *Adv. Func. Mater.* **20**, 3519-3529 (2010).
9. P. I. Djurovich, E. I. Mayo, S. R. Forrest and M. E. Thompson, *Org. Electron.* **10**, 515-520 (2009).

10. K. Tsutsumi, H. Yoshida and N. Sato, *Chem. Phys. Lett.* **361**, 367-373 (2002).
11. H. Yoshida, *Chem. Phys. Lett.* **539-540**, 180-185 (2012).
12. H. Yoshida, *Anal. Bioanal. Chem.* **406**, 2231-2237 (2014).
13. B. Boudaiffa, P. Cloutier, D. Hunting, M. A. Huels and L. Sanche, *Science* **287**, 1658-1660 (2000).
14. H. Yoshida, *Mater. Res. Soc. Symp. Proc.* **1493**, 295-301 (2012).
15. W. Han, H. Yoshida, N. Ueno and S. Kera, *Appl. Phys. Lett.* **103**, 123303 (2013).
16. Y. Ie, M. Karakawa, S. Jinnai, H. Yoshida, A. Saeki, S. Seki, S. Yamamoto, H. Ohkita and Y. Aso, *Chem. Commun.* **50**, 4123-4125 (2014).
17. S. Fabiano, H. Yoshida, Z. H. Chen, A. Facchetti and M. A. Loi, *ACS Appl. Mater. Interfaces* **5**, 4417-4422 (2013).
18. M. Casalegno, S. Zanardi, F. Frigerio, R. Po, C. Carbonera, G. Marra, T. Nicolini, G. Raos and S. V. Meille, *Chem. Commun.* **49**, 4525-4527 (2013).
19. G. Paternò, A. J. Warren, J. Spencer, G. Evans, V. G. Sakai, J. Blumberger and F. Cacialli, *J. Mater. Chem. C* **1**, 5619-5623 (2013).
20. M. T. Rispens, A. Meetsma, R. Rittberger, C. J. Brabec, N. S. Sariciftci and J. C. Hummelen, *Chem. Commun.* 2116-2118 (2003).
21. T. Sueyoshi, H. Kakuta, M. Ono, K. Sakamoto, S. Kera and N. Ueno, *Appl. Phys. Lett.* **96**, 093303 (2010).
22. F. Bussolotti., S. Kera K. Kudo, A. Kahn and N. Ueno, *Phys. Rev. Lett.* **110,** 267602 (2013).
23. F. Gutmann and L. E. Lyons, in *Organic Semiconductors* (John Wiley and Sons,

Inc., 1967).

24. N. Sato, K. Seki and H. Inokuchi, *J. Chem. Soc., Faraday Trans.* **2**, 1621-1633 (1981).

25. H. Yoshida, (submitted).

26. S. Duhm, G. Heimel, I. Salzmann, H. Glowatzki, R. L. Johnson, A. Vollmer, J. P. Rabe and N. Koch, *Nat. Mater.* **7**, 326-332 (2008).

27. Q. Bao, X. Liu, S. Braun and M. Fahlman, *Adv. Energy. Mater.* **4**, 1301272 (2013).

28. W. Gao and A. Kahn, *Appl. Phys. Lett.* **79**, 4040 (2001).

29. S. Guo, S. B. Kim, S. K. Mohapatra, Y. Qi, T. Sajoto, A. Kahn, S. R. Marder and S. Barlow, *Adv. Mater.* **24**, 699-703 (2012).

30. Y. Qi, S. K. Mohapatra, S. Bok Kim, S. Barlow, S. R. Marder and A. Kahn, *Appl. Phys. Lett.* **100**, 083305 (2012).

31. H. Yoshida, *Rev. Sci. Instrum.* **85**, 016101 (2014).

Chapter 5. Conclusion and Perspectives

An in-depth study of effect of interface and crystallization of materials on device performance of organic solar cells has been conducted and presented in this thesis. The goal is to control the photo-physical process in OSCs as to avoid trade-off relationship between V_{OC} and J_{SC}, and find a new route for optimizing device performance. Two strategy were purposed in this study:

Interfacial modification:

1. Control of V_{OC} of OSCs after fabrication of device via tuning D/A interfacial energy levels by switching the orientation of dipole moment.
2. Constructing ideal interface for OSCs via higher E_{CT}, suppressing charge recombination by enlarging D/A distance and introducing charge separation center in OSCs as to increase photocurrent generation.

Crystallization of PCBM:

Analyzing effect of crystallization of PCBM on its energy levels and device performance of OSCs.

The key factors in OSCs like interfacial energy levels, charge separation and recombination, CT state and crystallization of materials were analyzed in this thesis. By using the above two strategies, these factors could be controlled, and therefore improving device performance.

The study of insertion of dipole moment monolayer at D/A interface allowed us to clarify the relationship between device performance (V_{OC}) of OSC and D/A interfacial property (energy levels) (chapter 2), demonstrating the availability of the methodology I purposed about introducing D/A interfacial modification in bilayer OSCs. More importantly, the V_{OC} could be reversibly controlled via tuning the direction of dipole moment by electric field. This is the first report of manipulating V_{OC} of OSCs after fabrication of device. This not only showed the relationship between interfacial energy levels and V_{OC} , but also presented a new type of device which could response to external stimuli.

Back to the energy levels at D/A interface, I notice that increasing V_{OC} of OSCs by changing the energy levels is not enough. One can immediately see the trade-off relationship between maximizing E_{DA} and least requirement for LUMO offset for charge separation, these two factors contribute to V_{OC} and J_{SC} in OSCs, respectively. Therefore, I developed a new route to increasing PCE of OSCs by constructing ideal D/A interface (chapter 3, Figure 5.1.1c). Ideal interface comprise of efficient charge separation, suppressed charge recombination and high lying CT state (E_{CT}). Moreover, by using such ideal interface, the trade-off relationship should be avoided and ultimately improve the efficiency of device.

The above results suggested that same enhancement of device performance could be expected if these modification of interface could be introduced in BHJ device. That means even for efficient device with materials having optimized energy levels and interfacial buffer layer, the efficiency could still be pushed further by utilizing "ideal interface". This not only gives us a clue how I understand and also construct D/A interface, but also offer some guidelines for the materials design. For instance, design polymer with long and insulating side chain might block acceptor materials away from its backbone, achieving larger D/A distance as to increase E_{CT} and suppress recombination. Also, selectively introducing some segment on polymer backbone as charge separation center for efficient photocurrent generation while remains recombination suppressed. These points could be the future target of material design which could improve device performance further without confronting trade-off relationship.

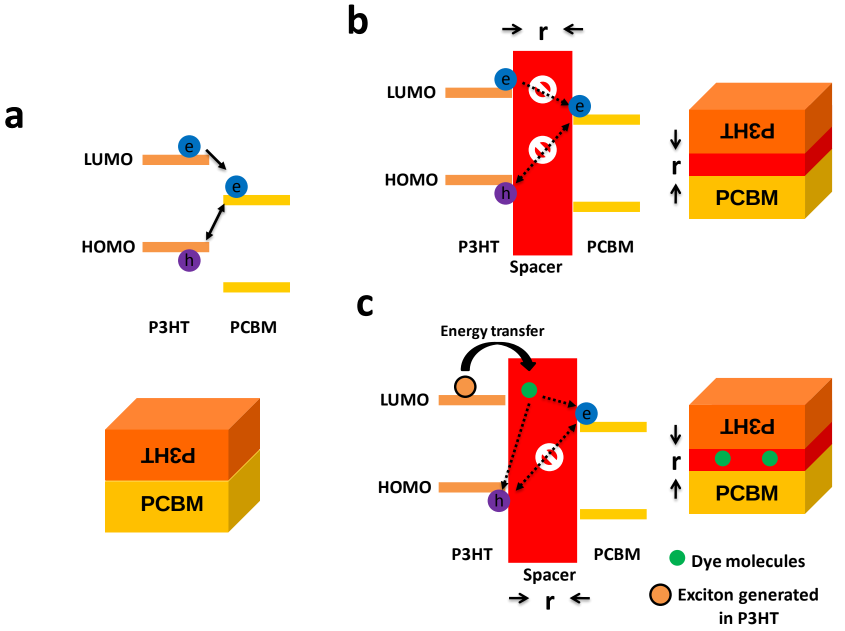

Figure 5.1.1 a) P3HT//PCBM interface at which charge separation and recombination happened. b) with spacer at P3HT//PCBM interface, CT state become delocalized due to enlarged charge transfer distance, and charge separation and recombination were also suppressed. c) introducing small amount of charge separation center to promote energy transfer for charge separation.

The second strategy I purposed to improve device performance is crystallization of materials. We conducted detailed analysis for crystallization of PCBM (chapter 4) since it is the most widely used acceptor materials in organic solar cells. Usually, crystallization of polymer is known to enhance the performance of OSCs, but I found that the crystallization of PCBM could also largely affect its electronic property (energy levels) and therefore OSC performance. This is the first report on the electronic property change induced by crystallization of PCBM, and the impact of polarization energy was highlighted. Furthermore, by using bilayer OSCs, the change of PCBM energy levels was successfully correlated to the change of device parameter

(V_{OC}). The detailed study of crystallization behavior of PCBM was also carried out and an novel "epitaxy growth" method was utilized to introduce crystallization of PCBM into BHJ device, leading to a enhancement in V_{OC}. This result could offer a new route to consider improving the efficiency of OSCs in terms of PCBM crystallization.

Since the study of crystalline PCBM so far mostly concentrated on its crystal structure, our research offered clear information about the electronic property of crystalline PCBM. Although there is discussion about crystalline PCBM having lower lying LUMO as to extract charges and help charge separation. Our results suggested that upward shift of energy levels (related to doping/de-doping) played an more important role in determining device performance although there is the shrinking of the band gap. However, crystalline PCBM in current study might be different from those in mixed phase (polymer:PCBM). Whether crystalline PCBM help charge separation is still not clear. Nevertheless, crystallization of PCBM could be considered as a new strategy to improve V_{OC} of device and could be the first step for screening on how crystallization of PCBM affects device performance. Further study for clarifying impact of crystallization of PCBM on photocurrent generation might help to increase device performance eventually.

In summary, two strategies, namely interfacial modification and crystallization of materials, were purposed in this study to improve the efficiency of device. The photo-physical processes at D/A interface was systematically analyzed, the results showed that device performance of OSCs could be largely affected by D/A interfacial property and crystallization of materials. It was demonstrated that by purposely modifying the interface in OSCs, a clearer picture of photo-physical process at interface could be revealed. Furthermore, by using crystallization as a useful tool, change of interfacial property like energy levels could be introduced even in BHJ device, enhancing parameters like V_{OC}. Through the above two strategies, I could understand more about the fundamental process in OSCs, a new route could be provided to push the efficiency of device and even pave the way for breaking its upper limit. The results obtained in this study could not only shed light on optimization of device structure, but also give guideline to the material design for more efficient OSCs.

Acknowledgements

I offer my sincere gratitude to all the people who had helped me during my Ph.D course.

I spend 3 years in Hashimoto lab supervised by Prof. Hashimoto. I would like to thank him for giving me a change to be a member of this amazing group. I also thank him for scientific training and teaching me the responsibility as a researcher. He taught me the way of thinking as a leader, and research should derive from the requirement from public society.

I also thank Dr. Tajima, our team leader, who had taught me lots of detailed knowledge of experiment. He is kind and supportive, I enjoy working with him very much. His broad band knowledge benefit my research and make me understand more and deeper about organic solar cell.

There are lots of lab members I want thank. Dr. Yang and Dr. Zhou help me a lot with the experiment when I just join the group, barely knowing anything. Dr. Zhao offered me good advises for future career. Dr. Liu (min) played football with me, and Dr. Liu (huan) taught me lots of things about research condition in China. Dr. Zhang and Dr. Zhao (minxiu) had shared lots of knowledge they know with me. Mr. Tada and Mr. Izawa also help me with experiments and lab maintaining. I also thank our secretary Nakajima-San, Shinoda-San and Mitsuzawa-San who were always supportive with the paper works. Mr. Ma also help me with synthesis of materials, and I had great time for two years working together.

Last but not least, I want give my special thanks to my family. My beloved wife He Qi and my lovely son Mulin, who is always by my side. They makes my life busy but fruitful. I also thank my parents being supportive with my Ph.D course.

It's impossible to recall all the people who helped me, I hope at least they would be glad to read my thesis.

Zhong Yufei

2014

List of Publications

1.**Yufei Zhong**, Kazuhito Hashimoto, and Keisuke Tajima. "Open Circuit Voltage Enhancement in Organic Solar Cells via Crystallization of PCBM", (***In preparation***)

2.**Yufei Zhong**, Seiichiro Izawa, Kazuhito Hashimoto, Keisuke Tajima, Tomoyuki Koganezawa and Hiroyuki Yoshida. "Crystallization-induced Energy Level Change of

[6,6]-Phenyl-C61-butyric Acid Methyl Ester (PCBM) Film", (***submitted***)

3.**Yufei Zhong**, Jusha Ma, Kazuhito Hashimoto, and Keisuke Tajima. "Electric Field-Induced Dipole Switching at the Donor/Acceptor Interface in Organic Solar Cells", ***Adv. Mater.*** 2013, 25, 1071–1075

4.**Yufei Zhong**, Akira Tada, Seiichiro Izawa, Kazuhito Hashimoto, and Keisuke Tajima. " Enhancement of V_{OC} without Loss of J_{SC} in Organic Solar Cells by Modification of Donor/Acceptor Interfaces", ***Adv. Energy Mater.*** 2014, 4, 1301332

5.**Yufei Zhong**, Akira Tada, Yanfang Geng, Qingshuo Wei, Kazuhito Hashimoto and Keisuke Tajima. "Donor/Acceptor Interface Modifications in Organic Solar Cells ", ***J. Photopolym. Sci. Technol.*** 2013, 26, 181-184.